

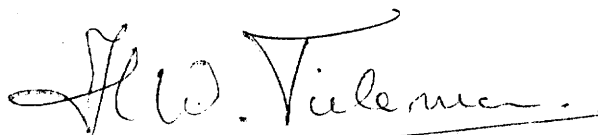
AN EXPERIMENTAL STUDY OF THE ATMOSPHERIC BOUNDARY LAYER  
MODIFIED BY A CHANGE IN SURFACE ROUGHNESS  
AND SURFACE TEMPERATURE /

by

Darrell B. Derrington, Jr.

Thesis submitted to the Graduate Faculty of the  
Virginia Polytechnic Institute and State University  
in partial fulfillment of the requirements for the degree of  
MASTER OF SCIENCE  
in  
Engineering Mechanics

APPROVED:

  
H. W. Tietelman, Chairman

  
F. J. Maher

  
R. A. Heller

May, 1977

Blacksburg, Virginia

LD  
5655  
V855  
1977  
D41  
C.2

## ACKNOWLEDGEMENTS

LM/MRS 6/7/77

The author wishes to express his thanks for the support supplied by NASA and its monitors. Without this help a project of this size would have surely remained a dream. Also, appreciation is expressed to Dr. H. W. Tieleman for his continuous constructive criticisms. I would also like to thank Professor F. J. Maher and Dr. R. A. Heller for their help in proofreading the text. Without these, this thesis would not have been possible.

The author also wishes to thank the many friends who provided moral support during his study. I need not mention their names, for they know who they are.

This thesis is dedicated to Mr. Oscar Derrington, Sr., the author's grandfather. He was an outstanding Christian and an inspiration to everyone who knew him.

## TABLE OF CONTENTS

<u>Chapter</u>	<u>Page</u>
ACKNOWLEDGEMENTS . . . . .	ii
LIST OF FIGURES . . . . .	v
LIST OF TABLES . . . . .	x
LIST OF SYMBOLS . . . . .	xi
I. INTRODUCTION . . . . .	1
II. THERMALLY STRATIFIED FLOW OF THE ATMOSPHERIC BOUNDARY LAYER . . . . .	3
2.1 Thermal Gradients . . . . .	3
2.2 The Governing Equations . . . . .	7
2.3 The Monin-Obukhov Similarity Hypothesis . . . . .	11
III. FLOW NEAR THE SEA-SHORE . . . . .	14
IV. EXPERIMENTAL PROCEDURE . . . . .	16
4.1 Instrumentation . . . . .	16
4.1.1 NASA Facility . . . . .	16
4.1.2 TSI Instrumentation . . . . .	17
4.1.3 Calibration Procedures . . . . .	18
4.2 DATA ACQUISITION AND DATA HANDLING . . . . .	19
4.3 DATA ANALYSIS . . . . .	20
4.3.1 Conversion from Voltages to Velocities . . . . .	20
4.3.2 Stationarity Test and Calculation of Mean Wind Angle . . . . .	21
4.3.3 Mean Sample Covariances . . . . .	24
4.3.4 Spectra . . . . .	26

<u>Chapter</u>	<u>Page</u>
4.3.5 Conversational Monitor System . . . . .	29
4.3.6 Calculation of Covariances and Variances from Cospectra and Spectra Respectively . . . . .	29
V. DISCUSSION OF RESULTS . . . . .	31
5.1 Mean Flow and Integral Statistics . . . . .	32
5.2 Spectra and Cospectra . . . . .	38
5.2.1 Spectra of Velocity . . . . .	41
5.2.2 Spectrum of Temperature . . . . .	51
5.2.3 Cospectra of Reynolds Stress and Heat Flux . . . . .	54
VI. CONCLUSIONS . . . . .	58
REFERENCES . . . . .	63
FIGURES . . . . .	65
TABLES . . . . .	127
VITA . . . . .	132

## LIST OF FIGURES

<u>Figure</u>	<u>Page</u>
1 . Potential temperature profiles for stable, neutral and unstable stratifications . . . . .	66
2 . Model for the temperature profiles for on-shore flow and the internal boundary layer (IBL) . . . . .	67
3 . 100 Hz low-pass filter . . . . .	68
4 . Tower location on Wallops Island and orientation of a general coordinate system . . . . .	69
5 . Vertical temperature distributions for run 7, 8 and 9 .	70
6 . Ratio of standard deviation of longitudinal velocity to local friction velocity as a function of $z/L$ . . . . .	71
7 . Ratio of standard deviation of lateral velocity to local friction velocity as a function of $z/L$ . . . . .	72
8 . Ratio of standard deviation of vertical velocity to local friction velocity as a function of $z/L$ . . . . .	73
9a. Logarithmic spectra of the vertical velocity normalized by the variance versus $f/f_m$ , moderately unstable, $-1.0 < z/L < 0$ . . . . .	74
9b. Logarithmic spectra of the vertical velocity normalized by the variance versus $f/f_m$ , moderately stable, $0 < z/L < +1.0$ . . . . .	75
9c. Logarithmic spectra of the vertical velocity normalized by the variance versus $f/f_m$ , very stable, $z/L > +1.0$ . .	76
10a. Logarithmic spectra of the longitudinal velocity normalized by the variance versus $f/f_0$ , moderately unstable, $-1.0 < z/L < 0$ . . . . .	77
10b. Logarithmic spectra of the longitudinal velocity normalized by the variance versus $f/f_0$ , moderately stable, $0 < z/L < +1.0$ . . . . .	78
10c. Logarithmic spectra of the longitudinal velocity normalized by the variance versus $f/f_0$ , very stable, $z/L > +1.0$ . . . . .	79

<u>Figure</u>	<u>Page</u>
11a. Logarithmic spectra of the lateral velocity normalized by the variance versus $f/f_0$ , moderately unstable, $-1.0 < z/L < 0$ . . . . .	80
11b. Logarithmic spectra of the lateral velocity normalized by the variance versus $f/f_0$ , moderately stable, $0 < z/L < +1.0$ . . . . .	81
11c. Logarithmic spectra of the lateral velocity normalized by the variance versus $f/f_0$ , very stable, $z/L > +1.0$ . . . . .	82
12a. Logarithmic spectra of the vertical velocity normalized by the variance versus $f/f_0$ , moderately unstable, $-1.0 < z/L < 0$ . . . . .	83
12b. Logarithmic spectra of the vertical velocity normalized by the variance versus $f/f_0$ , moderately stable, $0 < z/L < +1.0$ . . . . .	84
12c. Logarithmic spectra of the vertical velocity normalized by the variance versus $f/f_0$ , very stable, $z/L > +1.0$ . . . . .	85
13 . Variation of reduced peak-frequencies $f_m^u$ for longitudinal velocity spectra with $z/L$ . . . . .	86
14 . Variation of reduced peak-frequencies $f_m^v$ for lateral velocity spectra with $z/L$ . . . . .	87
15 . Variation of reduced peak-frequencies $f_m^w$ for vertical velocity spectra with $z/L$ . . . . .	88
16 . Estimates of the logarithmic spectra of the longi- tudinal velocity normalized by the local shear velocity at $f=10$ versus stability . . . . .	89
17 . Estimates of the logarithmic spectra of the lateral velocity normalized by the local shear velocity at $f=10$ versus stability . . . . .	90
18 . Estimates of the logarithmic spectra of the vertical velocity normalized by the local shear velocity at $f=10$ versus stability . . . . .	91
19a. Logarithmic spectra of the longitudinal velocity normalized with $(\kappa \epsilon z)^{2/3}$ versus the reduced frequency, moderately unstable, $-1.0 < z/L < 0$ . . . . .	92

<u>Figure</u>	<u>Page</u>
19b. Logarithmic spectra of the longitudinal velocity normalized with $(\kappa \epsilon z)^{2/3}$ versus the reduced frequency, moderately stable, $0 < z/L < +1.0$ . . . . .	93
19c. Logarithmic spectra of the longitudinal velocity normalized with $(\kappa \epsilon z)^{2/3}$ versus the reduced frequency, very stable, $z/L > 1.0$ . . . . .	94
20a. Logarithmic spectra of the lateral velocity normalized with $(\kappa \epsilon z)^{2/3}$ versus the reduced frequency, moderately unstable, $-1.0 < z/L < 0$ . . . . .	95
20b. Logarithmic spectra of the lateral velocity normalized with $(\kappa \epsilon z)^{2/3}$ versus the reduced frequency, moderately stable, $0 < z/L < +1.0$ . . . . .	96
20c. Logarithmic spectra of the lateral velocity normalized with $(\kappa \epsilon z)^{2/3}$ versus the reduced frequency, very stable, $z/L > 1.0$ . . . . .	97
21a. Logarithmic spectra of the vertical velocity normalized with $(\kappa \epsilon z)^{2/3}$ versus the reduced frequency, moderately unstable, $-1.0 < z/L < 0$ . . . . .	98
21b. Logarithmic spectra of the vertical velocity normalized with $(\kappa \epsilon z)^{2/3}$ versus the reduced frequency, moderately stable, $0 < z/L < +1.0$ . . . . .	99
21c. Logarithmic spectra of the vertical velocity normalized with $(\kappa \epsilon z)^{2/3}$ versus the reduced frequency, very stable, $z/L > 0$ . . . . .	100
22a. Logarithmic spectra of the longitudinal velocity normalized by the variance versus $f/\phi_u$ , moderately unstable, $-1.0 < z/L < 0$ . . . . .	101
22b. Logarithmic spectra of the longitudinal velocity normalized by the variance versus $f/\phi_u$ , moderately stable, $0 < z/L < +1.0$ . . . . .	102
22c. Logarithmic spectra of the longitudinal velocity normalized by the variance versus $f/\phi_u$ , very stable, $z/L > +1.0$ . . . . .	103
23a. Logarithmic spectra of the lateral velocity normalized by the variance versus $f/\phi_v$ , moderately unstable, $-1.0 < z/L < 0$ . . . . .	104



<u>Figure</u>	<u>Page</u>
23b. Logarithmic spectra of the lateral velocity normalized by the variance versus $f/\phi_V$ , moderately stable, $0 < z/L < +1.0$ . . . . .	105
23c. Logarithmic spectra of the lateral velocity normalized by the variance versus $f/\phi_V$ , very stable, $z/L > +1.0$ . . . . .	106
24a. Logarithmic spectra of the vertical velocity normalized by the variance versus $f/\phi_W$ , moderately unstable, $-1.0 < z/L < 0$ . . . . .	107
24b. Logarithmic spectra of the vertical velocity normalized by the variance versus $f/\phi_W$ , moderately stable, $0 < z/L < +1.0$ . . . . .	108
24c. Logarithmic spectra of the vertical velocity normalized by the variance versus $f/\phi_W$ , very stable, $z/L > +1.0$ . . . . .	109
25 . Variation of the reduced peak-frequencies of the longitudinal spectra with the dissipation parameter $\phi_U$ . . . . .	110
26 . Variation of the reduced peak-frequencies of the lateral spectra with the dissipation parameter $\phi_V$ . . .	111
27 . Variation of the reduced peak-frequencies of the vertical spectra with the dissipation parameter $\phi_W$ . . .	112
28 . Ratio of vertical and longitudinal velocity spectra versus reduced frequency, Run 6, 50-foot level . . . . .	113
29 . Ratio of lateral and longitudinal velocity spectra versus reduced frequency, Run 6, 50-foot level . . . . .	114
30a. Logarithmic spectra of the temperature fluctuations normalized by the variance versus $f/f_0$ , moderately unstable, $-1.0 < z/L < 0$ . . . . .	115
30b. Logarithmic spectra of the temperature fluctuations normalized by the variance versus $f/f_0$ , moderately stable, $0 < z/L < +1.0$ . . . . .	116
30c. Logarithmic spectra of the temperature fluctuations normalized by the variance versus $f/f_0$ , very stable, $z/L > +1.0$ . . . . .	117

<u>Figure</u>	<u>Page</u>
31 . Variation of reduced peak-frequencies $f_m$ for temperature spectra with $z/L$ . . . . .	118
32a. Logarithmic $uw$ cospectra normalized by the covariance $f/f_0$ , moderately unstable, $-1.0 < z/L < 0$ . . .	119
32b. Logarithmic $uw$ cospectra normalized by the covariance $f/f_0$ , moderately stable, $0 < z/L < +1.0$ . . . .	120
32c. Logarithmic $uw$ cospectra normalized by the covariance $f/f_0$ , very stable, $z/L > +1.0$ . . . . .	121
33 . Variation of reduced peak-frequencies $f_m^{uw}$ for the $uw$ cospectra with $z/L$ . . . . .	122
34a. Logarithmic $w\theta$ cospectra normalized by the covariance versus $f/f_0$ , moderately unstable, $-1.0 < z/L < 0$ . . . . .	123
34b. Logarithmic $w\theta$ cospectra normalized by the covariance versus $f/f_0$ , moderately stable, $0 < z/L < +1.0$ . . . . .	124
34c. Logarithmic $w\theta$ cospectra normalized by the covariance versus $f/f_0$ , very stable, $z/L > +1.0$ . . . .	125
35 . Variation of reduced peak-frequencies, $f_m^{w\theta}$ for the $w\theta$ cospectra with $z/L$ . . . . .	126

## LIST OF TABLES

<u>Table</u>	<u>Page</u>
1. Summary of mean data and integral statistics for all runs . . . . .	128
2. Summary of the spectral characteristics for the variance normalized logarithmic spectra versus the modified frequency $f/f_m$ . . . . .	130
3. Summary of the spectral characteristics for the variance normalized logarithmic spectra versus the modified frequency $f/f_0$ . . . . .	131

## LIST OF SYMBOLS

A,B	Constants (5.12)
$c_p$	Specific heat for constant pressure
$E_{ij}$	Transformation matrix
$f$	Frequency in Hertz, reduced frequency $nz/U$
$f_m$	Reduced peak frequency, $z/\lambda_m$
$f_0^\alpha$	Intercept of the inertial subrange with the line $n S_\alpha(n)/\sigma_\alpha^2 = 1$
$F_\alpha$	Universal spectral function in the inertial subrange
$g$	Acceleration due to gravity
$g_\alpha$	Spectral function for low frequency range
$H_f$	Discrete Fourier transform of a data block
$H_j$	Heat flux
$k$	Wave number $2\pi n/U$ , adiabatic exponent
$L_x^u$	Longitudinal integral scale of turbulence
$m$	Number of blocks per run
$n$	Frequency in Hertz
$N$	Number of data points per block, rate of dissipation of $\frac{1}{2} \overline{\theta'^2}$ (5.11)
$p$	Instantaneous pressure
$p'$	Pressure fluctuation
$P$	Mean pressure
$q$	Vertical heat flux

$R$	Gas constant for air, total number of reverse arrangements (4.5)
$R_f$	Flux Richardson number
$R(\tau)$	Autocorrelation coefficient
$S_x$	Power spectral density function
$S_{xy}$	Cross spectral density function
$S_\alpha(n)$	Spectral function, $\alpha = u, v, w, \theta$
$T$	Temperature
$T_0$	Reference temperature (dry adiabatic)
$T_1$	Temperature deviations from the reference temperature
$T_*$	Scaling temperature (2.28)
$u, v, w$	Velocity components in mean wind coordinate system
$u_i$	Velocity components in Cartesian coordinate system, $i = 1, 2, 3$
$u', v', w'$	Fluctuating velocity components in mean wind coordinate system
$u_i'$	Fluctuating velocity in Cartesian coordinate system, $i = 1, 2, 3$
$U$	Mean wind velocity in x-direction
$U_i$	Mean velocity components in Cartesian coordinate system, $i = 1, 2, 3$
$U_*$	Local shear velocity
$U_{*0}$	Ground shear velocity
$U_{j,i}$	Discrete time histories, $j = u, v, w, T$ , $i = 1, \dots, 8192$
$\bar{U}_j$	Block means, $j = u, v, w, T$

$w(j)$	Data window function
$x,y,z$	Mean wind coordinate system
$x',y',z'$	TSI coordinate system
$x_i$	Cartesian coordinate system, $i = 1,2,3$
$\bar{x}$	Sample mean, $x = u_1, u_2, u_3, \theta$
$\overline{x^2}$	Sample variance, $x = u_1, u_2, u_3, \theta$
$\overline{xy}$	Sample covariance, $x, y = u_1, u_2, u_3, \theta$
$\overline{x_m^2}$	Block variance, $x = u_1, u_2, u_3, \theta$
$\overline{xy_m}$	Block covariance, $x = u_1, u_2, u_3, \theta$
$z_0$	Roughness parameter
—	Overbar, denotes time averaging
$\alpha$	Index, $\alpha = u, v, w, \theta$
$\beta$	Probe yaw angle
$\gamma$	Lapse rate
$\Delta t$	Time increment
$\delta_{ij}$	Kronecker delta
$\epsilon$	Dissipation
$\epsilon_{ijk}$	Permutation symbol
$\theta'$	Fluctuating temperature
$\kappa$	Von Karman's constant
$\lambda$	Latitude
$\lambda_m$	Peak wave length
$\nu$	Kinematic viscosity
$\xi$	Stability parameter, $z/L$
$\xi_i$	External parameters (5.5)

$\rho$	Density
$\rho_0$	Density of air at the reference temperature
$\sigma_\alpha$	Standard deviation, $\alpha = u, v, w, \theta$
$\sigma_j$	Block standard deviation, $\alpha = u, v, w, \theta$
$\sigma_{ij}$	Stress tensor
$\sigma$	Time delay
$\phi$	Dimensionless velocity profile
$\phi_l$	Dimensionless temperature profile
$\phi_a$	Dimensionless dissipation function
$\omega$	Angular velocity of earth

## CHAPTER I

### INTRODUCTION

In recent years a large amount of data has been gathered for the study of turbulence in the atmospheric boundary layer. Unfortunately this data was gathered for rather simple types of flow, which is necessary to validate basic hypotheses, but is of little use for engineering applications. Very often the types of flow measured were over a surface that could be treated as horizontally homogeneous. In addition, the heights at which data was obtained were limited to the surface layer and as a result it was difficult to describe the portion of the flow that is of interest to engineering problems. The flow in the surface layer allows for a one-dimensional treatment of the problem. If this were the case in most real atmospheric flows, then the study of turbulence would be greatly simplified.

The types of flow of more interest to engineering applications contain horizontal inhomogeneities and do not correspond to the ideal situation. Sudden changes in surface roughness and temperature can occur and the theoretical one-dimensional model breaks down. One condition that would induce such a flow is a land-sea interface. As the air approaches the land, coming from the sea, it will experience changes that will set up a more complicated, three-dimensional type of flow. A thorough investigation of this flow would then enable one to extend, or prove, the already existent hypotheses for the more complex type of flow. With this information, problems such as air



pollution and hazards to low flying aircraft could be better understood.

In this report a more complicated type of flow is investigated which is an on-shore flow from the ocean crossing the beach at an oblique angle. Measurements of this flow have been taken at high sample rates and include measurements at various heights, high enough to describe the portion of the mean wind and temperature profiles and fluxes that are of interest for the solution of practical engineering problems. These problems could include air pollution (fumigation and plume trapping), operation of low flying aircraft, crop-spraying and crop-dusting operations.

## CHAPTER II

### THERMALLY STRATIFIED FLOW OF THE ATMOSPHERIC BOUNDARY LAYER

#### 2.1 Thermal Gradients

For the case of no flow the vertical force on a parcel of air at some arbitrary height  $z$  can be expressed as

$$F(z) = -g - \frac{1}{\rho} \frac{\partial p}{\partial z} \quad (2.1)$$

Using the equation of state for an ideal gas the pressure gradient in (2.1) can be written as follows

$$\frac{\partial p}{\partial z} = \rho R \frac{\partial T}{\partial z} = -\rho R \gamma \quad , \quad (2.2)$$

where

$$\gamma = -\frac{\partial T}{\partial z} \quad (2.3)$$

is the lapse rate of air. This then allows for equation (2.1) to take on the form of

$$F(z) = R(\gamma - g/R) \quad (2.4)$$

For positive values of  $F(z)$ , when the lapse rate  $\gamma$  is greater than  $g/R$  and  $\partial T/\partial z < -g/R$  a parcel of air which has been displaced upward will experience positive buoyancy and continue to rise. This situation is referred to as unstably stratified air.

For the case of a zero vertical force,  $\gamma = g/R$ , a neutral condition arises and hydrostatic equilibrium is obtained. When a fluid

particle is being moved to a different elevation the buoyancy force and weight balance each other.

In the event that  $\gamma$  is less than  $g/R$ , then if a parcel of air is displaced upward it will attempt to move back to its original location as a result of the weight of the parcel being larger than the buoyancy force. This then allows for a stable condition or inversion to develop (Fig. 1).

In the case where the temperature differences between different points in a flow field are small such that the velocity field is only slightly affected, the flow is referred to as forced convection. However, if the temperature differences are at the same time large enough to dominate the heating resulting from internal friction, the temperature inhomogeneities will simply move along with the fluid and be smoothed out under the influence of molecular thermal conductivity. In this case, the temperature is referred to as a passive admixture, and these conditions are realized for near neutrally stratified flow.

Another case that should be discussed is the case where temperature is not considered a passive admixture. This is the flow of a nonuniformly heated fluid in a gravitational field. This flow arises as a result of Archimedean forces which create an upward buoyancy of the lower warmer air and a downward motion of the higher and cooler air in unstable stratified air. In the case of stable stratification, the warmer air overlies the colder air and vertical motion is inhibited. These flows for a temperature-inhomogeneous fluid are commonly referred to as convection. If it is assumed that the velocity

of our motion is sufficiently small so that variations in density produced by variations in pressure can be ignored, then by using the aforementioned conditions, the continuity equation and the momentum equation can be formulated into the equations for free convection or the Boussinesq equations as they are commonly referred to [8].

It will be advantageous at this point to clarify some variables needed for further discussion. The potential temperature,  $\theta$ , is a term quite often encountered in atmospheric turbulence literature and is defined as the temperature a parcel of air would assume if brought isentropically to the standard pressure of 1000 mb. For an ideal gas it follows from the first law of thermodynamics that the potential temperature,  $\theta$ , is given by

$$Tp^{-k} = \theta (1000)^{-k} \quad (2.5)$$

where

$p$  = local atmospheric pressure in mb.

$T$  = local absolute temperature

$k = R/c_p$  for air

$\theta$  = potential temperature

Rewriting this yields the following form for  $\theta$ ,

$$\theta = T \left( \frac{1000}{p} \right)^k \quad (2.6)$$

It is commonly assumed that the temperature,  $T(x,y,z,t)$ , may be stated in the form

$$T = T_0 + T_1 \quad (2.7)$$

where  $T_0$  is some reference value, and  $T_1$  is some small deviation from the reference value.

With the aid of the above formulations the flux Richardson number  $R_f$  is defined as the ratio of rates of energy lost or gained by buoyancy to the energy introduced mechanically through the mean wind shear. In other words it is a measure of the deviation from the so-called neutrally stratified boundary layer ( $R_f = 0$ ) and in equation form is

$$R_f = \frac{\frac{g}{\theta} \overline{w'\theta'}}{\overline{u'w'} \frac{dU}{dz}} \quad (2.8)$$

$g$  = acceleration due to gravity

$\theta$  = mean potential temperature (local)

$w'\theta'$  = covariance between vertical velocity fluctuations and temperature

$u'w'$  = Covariance of the vertical and streamline velocity fluctuations

The last term  $dU/dz$  can be found by assuming a semilogarithmic expression for the velocity profile which is

$$U = A \ln z + B, \quad (2.9)$$

$$dU = \frac{A}{z} dz,$$

$$\frac{dU}{dz} = \frac{A}{z}, \quad (2.10)$$

where  $A$  and  $z$  are determined locally from experimental data.

For measurements in the atmospheric boundary layer, the quantity,  $\overline{u'w'}$ , is always less than zero and  $dU/dz$  is always greater than zero. Therefore, for positive values of  $\overline{w'\theta'}$ , the flux Richardson number is less than zero, corresponding to an unstable stratification. Conversely, for negative values of  $\overline{w'\theta'}$ , the Richardson number is greater than zero, which corresponds to a stable stratification. For a neutral condition,  $d\theta/dz$  is zero which corresponds to a zero vertical heat flux and thus the flux Richardson number is also zero.

## 2.2 The Governing Equations

In order to formulate the equations that govern turbulent flows one must begin by breaking up the flow quantities into a mean part and a fluctuating part, thus Reynolds decomposition is introduced:

$$\left. \begin{aligned} u_i &= U_i + u_i' & , & \quad \overline{u_i'} \equiv 0 , \\ T_1 &= \overline{T_1} + \theta' & , & \quad \overline{\theta'} \equiv 0 , \\ p &= P + p' & , & \quad \overline{p'} \equiv 0 . \end{aligned} \right\} \quad (2.11)$$

Now by applying Reynolds decomposition to the momentum, continuity, and thermodynamic energy equation and applying a time average, the equations for the mean motion and mean temperature are:

$$\frac{\partial U_i}{\partial t} + U_j \frac{\partial U_i}{\partial x_j} = \frac{1}{\rho_0} \frac{\partial}{\partial x_j} \sigma_{ij} + g \frac{\overline{T_1}}{T_0} \delta_{i3} - 2\epsilon_{ijk} \omega_j U_k , \quad (2.12)$$

$$\frac{\partial U_i}{\partial x_i} = 0 , \quad (2.13)$$

$$\frac{\partial \overline{T_1}}{\partial t} + U_j \frac{\partial \overline{T_1}}{\partial x_j} = - \frac{\partial}{\partial x_j} \frac{H_j}{c_p \rho_0} , \quad (2.14)$$

where the stress tensor is

$$\sigma_{ij} = -P \delta_{ij} + \nu \rho_0 \left( \frac{\partial U_i}{\partial x_j} + \frac{\partial U_j}{\partial x_i} \right) - \rho_0 \overline{u_i' u_j'} \quad (2.15)$$

and the heat flux tensor is

$$H_j = c_p \rho_0 \left( -\kappa_T \frac{\partial \bar{T}}{\partial x_j} + \overline{\theta' u_j'} \right), \quad (2.16)$$

and  $-2 \epsilon_{ijk} \omega_j U_k$  represents the Coriolis accelerations.

The terms  $-\rho_0 \overline{u_i' u_j'}$  and  $c_p \rho_0 \overline{\theta' u_j'}$  are turbulent additions to the molecular stresses and the turbulent heat fluxes, respectively.

In order to facilitate the study of the flow let us consider the following simplified case with the conditions:

- i. Steady mean flow  $\partial/\partial t = 0$
- ii. Mean flow parallel to earth surface,  $U_3 = 0$
- iii. Neglect horizontal turbulent fluxes as compared to vertical fluxes
- iv. Assume molecular terms to be negligible compared to corresponding turbulent ones
- v. Neglecting the vertical component of the Coriolis force as compared to the gravitational force

With these imposed constraints the equations for the mean flow take the following form.

Momentum Equation:

$$x_1\text{-direction: } U_1 \frac{\partial U_1}{\partial x_1} + U_2 \frac{\partial U_1}{\partial x_2} = -\frac{1}{\rho_0} \frac{\partial P}{\partial x_1} - \frac{\partial \overline{u_1' u_3'}}{\partial x_3} + f U_2. \quad (2.17)$$

( $f$  is  $2\omega \sin \lambda$ , where  $\omega$  is the angular velocity of the earth and  $\lambda$

is latitude.)

$$x_2\text{-direction: } U_1 \frac{\partial U_2}{\partial x_1} + U_2 \frac{\partial U_2}{\partial x_2} = - \frac{1}{\rho_0} \frac{\partial P}{\partial x_2} - \frac{\partial \overline{u_2' u_3'}}{\partial x_3} - f U_1 . \quad (2.18)$$

$$x_3\text{-direction: } 0 = - \frac{1}{\rho_0} \frac{\partial P}{\partial x_3} - \frac{\partial \overline{u_3' u_3'}}{\partial x_3} + g \frac{\overline{T_1}}{T_0} . \quad (2.19)$$

Continuity:

$$\frac{\partial U_1}{\partial x_1} + \frac{\partial U_2}{\partial x_2} = 0 . \quad (2.20)$$

Thermodynamic Energy Equation:

$$U_1 \frac{\partial \overline{T_1}}{\partial x_1} + U_2 \frac{\partial \overline{T_1}}{\partial x_2} = - \frac{\partial \overline{\theta' u_3'}}{\partial x_3} \quad (2.21)$$

As we focus our attention to the flow near the earth's surface, the Coriolis force and the pressure gradient force can be neglected with respect to Reynolds stresses, and the direction of the mean flow does not vary with height. With the mean wind in the  $x_1$  direction ( $U_2 = 0$ ), the governing equations reduce as follows:

Momentum:

$$x_1\text{-direction: } 0 = - \frac{\partial \overline{u_1' u_3'}}{\partial x_3} , \text{ or } \overline{u_1' u_3'} = \text{constant} = U_*^2 \quad (2.22)$$

$$x_2\text{-direction: } \overline{u_2' u_3'} = 0 \text{ (due to assumption of one-dimensional flow)} \quad (2.23)$$

$$x_3\text{-direction: } 0 = \frac{\partial \overline{u_3' u_3'}}{\partial x_3} + g \frac{\overline{T_1}}{T_0} , \quad (2.24)$$



Continuity:

$$\frac{\partial U_1}{\partial x_1} = 0 \quad , \quad U_1 = f(x_3) \quad (2.25)$$

Thermodynamic Energy Equation:

$$U_1 \frac{\partial \bar{T}_1}{\partial x_1} = - \frac{\partial \overline{\theta' u'_3}}{\partial x_3} \quad (2.26)$$

Assuming horizontal homogeneity of the temperature leads to

$$\frac{\partial \bar{T}_1}{\partial x_1} = 0 \quad (2.27)$$

and consequently

$$- \frac{\partial \overline{\theta' u'_3}}{\partial x_3} = 0 \quad , \quad \text{or } \overline{\theta' u'_3} = \text{constant} = \kappa U_* T_* \quad (2.28)$$

With these assumptions, the energy budget for the fluctuating portion of the flow becomes

$$\frac{\partial}{\partial x_3} \left( \overline{u'_3 e} + \frac{u'_3 p'}{\rho_0} \right) = - \overline{u'_1 u'_3} \frac{\partial U_1}{\partial x_3} + \frac{g}{T_0} \overline{\theta' u'_3} - \epsilon \quad , \quad (2.29)$$

where  $e = u_i u_i / 2$  is the turbulent kinetic energy per unit mass. The terms on the left hand side of this equation consist of the vertical turbulent energy flux and the pressure transport term. The first term on the right hand side is the mechanical production term which is usually positive. The second term on the right is the thermal production or vertical heat flux term which is positive in an unstable atmosphere and negative in a stable atmosphere. The last term on the right side represents the dissipation of turbulent energy into heat.

### 2.3 The Monin-Obukhov Similarity Hypothesis

The turbulence characteristics for the above thermally stratified flow model are functions of the following physical parameters:

$$\sqrt{u_1' u_3'} \equiv U_* - \text{shear velocity}$$

$$\overline{\theta' u_3'} = q / c_p \rho_0 - \text{vertical heat flux}$$

$$g/T_0 - \text{buoyancy parameter}$$

$$z - \text{height}$$

Therefore any non-dimensional parameter describing this type of turbulent flow needs to depend on one single non-dimensional variable obtained from the above four parameters. This means that the three quantities  $U_*$ ,  $q/c_p \rho_0$  and  $g/T_0$  should form some length parameter which from dimensional consideration has to be

$$L \equiv \frac{-U_*^3}{\kappa \frac{g}{T_0} \frac{q}{c_p \rho_0}} = \frac{-U_*^3}{\kappa \frac{g}{\theta} \frac{\overline{\theta' u_3'}}{c_p \rho_0}}, \quad (2.30)$$

where  $L$  is called the Monin-Obukhov (M-O) length scale.

In general, it follows that any non-dimensional parameter describing this type of flow should be a function of

$$\xi = \frac{z}{L}. \quad (2.31)$$

The  $\kappa$  appearing in the length scale is the Von Karman constant and was introduced in the definition of  $L$  by Obukhov [9]. The sign of  $L$  was chosen such that for positive values, a stable stratification is depicted with negative values for the heat flux,  $q$  (downward heat flux).

This means that the dimensionless wind shear, dimensionless temperature gradient, and the dimensionless variances of the turbulence quantities ( $\sigma_\alpha$ ,  $\alpha = u, v, w, \theta$ ), should be universal functions of  $\xi$ . Also the dimensionless spectra and cospectra of the turbulence fluctuations should be universal functions of  $\xi$  and the reduced frequency  $f = nz/U$  [9].

It should be added that the M-0 similarity theory is only valid in the surface layer, which is defined as the layer close to the ground where stress and heat flux can be considered to be constant.

By applying the M-0 similarity theory to the gradients of the mean velocity and mean temperature profiles one obtains the expressions

$$\frac{\kappa z}{U_*} \frac{dU}{dz} = \phi\left(\frac{z}{L}\right) \quad (2.32)$$

and

$$\frac{\kappa z}{T_*} \frac{d\bar{\theta}}{dz} = \phi_1\left(\frac{z}{L}\right) \quad , \quad (2.33)$$

where  $\phi$  and  $\phi_1$  should be universal functions of  $\xi$ .  $\kappa$  is the Von Karman constant and  $\phi$  is defined such that  $\phi(0) = 1$ . At neutral conditions when  $z/L = 0$ ,  $dU/dz = U_*/\kappa z$ , which after integration leads to the well-known semi-logarithmic velocity profile. A more detailed review of the universal functions  $\phi$ ,  $\phi_1$  and those functions for the variances is presented by Monin and Yaglom [8].

The universal functions are divided into two distinct parts corresponding to a stable or unstable stratification of the atmosphere in the surface layer. These regimes must approach each other as the

stratification becomes neutral (as  $q \rightarrow 0$ ). However Busch [ 1 ] finds that the turbulence structure in the surface layer experiences finite changes when stability changes from stable to unstable or vice versa.

Similarity arguments have been used to describe the universal functions  $\phi$  and  $\phi_1$  to the limiting cases of  $z/L \rightarrow -\infty$  (free convection) and  $z/L \rightarrow +\infty$  (highly stable stratified flow). Explicit equations for the functions  $\phi$  and  $\phi_1$  for all values of  $z/L$  can be obtained by interpolation between the three asymptotic cases (Monin and Yaglom [ 8 ]). The numerical evaluation of the coefficients in these expressions has to be obtained from experimental results. Many papers are available in the open literature which present theoretical and/or experimental results. Again Monin and Yaglom [ 9 ] give an excellent review of the existing interpolation and semi-empirical expressions for the universal functions  $\phi$  and  $\phi_1$ . More recently, these functions have been reviewed by Hicks [ 4 ].

### CHAPTER III

#### FLOW NEAR THE SEA-SHORE

When air blows over a sea and the surface temperature of the water is lower than the air above it, the lower layers of the atmosphere are cooled and an inversion develops. As this stable flow approaches a land-sea interface (Fig. 2) it sees a change in roughness length,  $z_{02} > z_{01}$ , and a possible change in surface temperature. Over land, the stable air is heated from below, when  $T_{02} > T_{01}$ , and as a result, with unstable stratification a new internal boundary layer (IBL) is developing with stable air above it. As this flow moves inland the IBL grows vertically. The rate of growth depends on the changes in surface roughness and temperature. Eventually, far enough inland, the IBL replaces the originally stable layer.

The vertical distribution of the Richardson number changes from negative to positive with increasing height and the point where the Richardson number is equal to zero corresponds to the height of the base of the inversion above the IBL. Under extremely stable conditions, which may occur during midday in the summer months, the turbulence in the inversion layer can be destroyed or reduced to very low levels. Because of the extreme low levels of turbulence, the flow in this layer loses dynamic contact with the IBL and is governed strictly by pressure gradient and Coriolis forces. This type of flow will only occur if the inversion layer coming in off of the sea is sufficiently deep. The viscous forces have a very small effect on this part of the

flow. Naturally an upper limit exists on this inversion layer, so that a stable layer of air between the IBL and the outer part of the planetary boundary layer (PBL) exists. For this type of flow the result is that the air in the inversion layer moves much faster than the layers above and below it. This type of flow can be considered as a low level jet. The turning of the wind in this layer, as a result of Coriolis forces, is appreciable, and the sudden changes in magnitude and direction of the wind vector can present a hazard to low flying aircraft. In addition, this type of flow enhances air pollution with the advent of fumigation and plume trapping.

Therefore, under ideal conditions one can encounter a stable layer of air (with extremely low turbulence levels) moving between the developing IBL and the outer part of the PBL. Because of the absence of turbulence in this layer under extreme stability conditions, depending on the difference between the sea temperature and the air above it, very little mixing takes place between this stable layer and the surrounding air. The result is that the viscous forces play a negligible role and the flow is governed by pressure gradient forces and Coriolis forces as was mentioned earlier. Because of the lack of the retarding effects due to turbulent mixing, the velocity in this layer can be expected to be high compared to the velocity in the neighboring layers.

## CHAPTER IV

### EXPERIMENTAL PROCEDURE

#### 4.1 Instrumentation

##### 4.1.1 NASA Facility

The data obtained, was gathered simultaneously from two separate wind sensing instrument systems. The first system consists of a two-dimensional wind speed transmitter, direction transmitter and temperature sensing instrument (Teledyne Geotech) operated by NASA and located on the 250-foot meteorological tower. The tower is located at Wallops Island, Virginia and is surrounded by the Atlantic Ocean from the east and a tidal flat on the west. Ten sets of wind and temperature sensors are located at 50-foot intervals with the first set of instruments at a height of 50 feet and the last set at a height of 250 feet. The wind speed transmitter is a three cup photo-chopper type unit. The output of the transmitter is a frequency proportional to the wind speed. The frequency speed relationship is linear with an accuracy of  $\pm 1$  percent of true. The wind direction transmitter consists of a vane which operates on the same principle as the wind speed transmitter unit but with a different frequency to direction ratio.

The temperature sensing instruments have an aspirated thermal radiation shield and are located near the wind and direction transmitters. Each of the cup-vane systems are mounted on opposite sides of the tower for a total of ten wind speed transmitters, wind

direction transmitters, and temperature sensors. An automatic switching unit specifies which side is to be used, based on the oncoming direction of the wind. At all times data are taken with the upstream instruments, thus eliminating any influence of the tower on the wind data.

#### 4.1.2 TSI Instrumentation

The second system is a three-dimensional split film anemometer (TSI-1080D) capable of high frequency velocity-vector and temperature measurements. Each probe consists of three split film sensors and a copper-constantan thermocouple for ambient temperature measurement. Each sensor is a 0.006 inch diameter quartz rod coated with a platinum film of about 1000 angström in thickness. The platinum film on each rod consists of two segments, separated from each other by two longitudinal splits 180 degrees apart. The total sensor length is two-tenths of an inch. The three sensors are mounted mutually perpendicular to form a Cartesian coordinate system and are secured at the end of a long and thin supporting structure. When the three sensors and thermocouple are not in use, they are protected by an aluminum shield which slides into place covering the fragile sensors. As an added precaution, filtered air blows across the sensors when the shield is in place in order to protect them from contamination of the salt air environment.

Five probes were mounted near the NASA cup-vane anemometers with an additional probe at the 30-foot level. Each probe is mounted on a rotor which is capable of rotating the probe about a vertical axis.



The rotor is controlled from the instrumentation trailer, which is parked at the base of the tower. The rotor allows for rotation of the probe about a vertical axis so as to align the probes approximately into the mean wind. For a more detailed review of the TSI instrumentation system, consult reference [12].

#### 4.1.3 Calibration Procedures

Calibration of both the NASA and TSI anemometer systems is carried out in the low speed Aerolab wind tunnel located in the Environmental Test Laboratory (ETL) on the main base at NASA Wallops Flight Center. The temperatures and air speed in the test section of the wind tunnel are monitored by an electric thermometer and two electric manometers. A Hastings Precision Air-Meter (hot wire anemometer) was used to obtain rough estimates of the test section wind velocities when they need to be changed. Calibration of the NASA cup-vane system was done by NASA personnel in the ETL.

In order to obtain data of a desired accuracy from the TSI probes, a completely new calibration and operating procedure was developed. Instead of using the calibration constants supplied by the factory all constants were obtained from calibration procedures carried out in the low speed wind tunnel and thermal chamber. This procedure proved to be both time consuming and complicated, however reliable and necessary. The outputs of the thermometer and electric manometers and six voltages from the TSI anemometers are fed into a data acquisition system which is controlled by a HP 9810A programmable calculator and a HP 2570A coupler/controller. These outputs are then

digitized and averaged for 100 samples. The average values of the temperature, standard velocity, and six bridge voltages from the TSI anemometer are then printed on paper tape for further reference.

The probe was mounted in the test section of the wind tunnel on a support that was able to rotate about a vertical axis. This allowed for calibration of the probe at various angles of attack ranging from plus to minus 50 degrees. Although the probe is calibrated for angles of attack between plus and minus 50 degrees, it is not recommended for use at angles in excess of 40 degrees. The procedures for obtaining the various constants necessary for the calculation of velocity components and temperature are reviewed in detail in reference [12].

#### 4.2 Data Acquisition and Data Handling

The Data Acquisition System is capable of sampling from one to thirteen TSI 1080 anemometer systems at a rate of 200 samples per second for a period of about one hour. The data acquisition system itself is housed in a trailer located directly beneath the 250-foot meteorological tower. The system consists of two main parts: a) the multiplexing and analog recording system, and b) the demultiplexing, digitizing and digital recording system. The output of each anemometer consists of seven analog voltages, one from the thermocouple and six from the hot films.

The multiplexed outputs from each anemometer are recorded on one channel of the analog recorder. Later, each channel is played back and the analog voltages passed through a low pass filter (100 Hz)

and into an analog to digital converter and finally recorded on digital magnetic tape.

The wind speed, direction, and temperature, from the NASA instruments whose outputs are in frequency form, are collected by a wind data system which is located at the base of the tower. After frequency to digital conversion, this system then transmits the data to the main base, which is approximately eight miles away, where it is then time correlated and stored on a seven track incremental digital tape recorder. These tapes, capable of storing up to eight hours of data, sampled every two seconds, are then analyzed on the HW-625 computer at NASA, Wallops Flight Center. The results include mean wind direction, mean temperature and low frequency spectral information of the streamwise and lateral velocity fluctuations.

#### 4.3 Data Analysis (TSI Instruments)

The digitized high-frequency data, written on nine track magnetic tapes, is taken to Virginia Polytechnic Institute and State University where it is analyzed with the aid of the IBM-370. Four computer programs have been developed to transform the data into the following statistical parameters: mean values, variances, covariances and spectra. These programs and their respective functions are discussed in the following sections.

##### 4.3.1 Conversion from Voltages to Velocities

As was discussed earlier the seven output voltages from the anemometers are recorded on a nine track magnetic tape. The first

step of the data analysis is to convert these seven voltages into a temperature and three velocity components (in the sensor oriented coordinate system) using the constants obtained from calibration. The temperature and the three velocity components are then stored on another nine track magnetic tape and await the next step of data reduction.

#### 4.3.2 Stationary Test and Calculation of Mean Wind Angle

As with all statistical and spectral analyses, the assumption of stationarity of time histories is mandatory. Therefore it is necessary that this assumption be checked. As was mentioned earlier, each sample of data from each TSI 1080 probe consists of four discrete time histories, namely the three velocity components in the sensor oriented coordinate system and the temperature, all sampled at a rate of 200 points per second for a time period of approximately one hour. The total number of data points in each time history is then about 680,000.

Because direct spectral analysis of this large quantity of data is clearly impossible, it is necessary to divide the time history into a number of data blocks and apply statistical and spectral analysis to each block separately. A specially developed fast Fourier transform algorithm [11] is used to calculate the spectra, and consequently it is necessary that the number of data points per block be an integer power of 2 in order that no data are lost. In view of the capabilities of the IBM-370, the number of data points per block was chosen to be  $N = 2^{13} = 8192$ . Although the number of data blocks in each time history

varied, on the average there were about 75 blocks per run. This corresponds to a total number of  $M \cdot N = 75 \times 8192 = 614,400$  points per time history that is analyzed. Each block represents a sample of 40.96 seconds in real time. The lowest frequency which can be analyzed is 0.02 Hz and the highest frequency is 100 Hz.

It is now possible to calculate the statistical quantities for each block that will help to determine the degree of stationarity of the data. One method will be to calculate and inspect the variation in block means, the block standard deviations and the block probe-yaw angles. Let the four discrete time histories be denoted by

$$U_{j,i} \begin{cases} U_{1,i} = x' \text{ component of velocity} \\ U_{2,i} = y' \text{ component of velocity} \\ U_{3,i} = z' \text{ component of velocity} \\ U_{4,i} = \text{temperature} \end{cases} \quad (4.1)$$

( $x', y', z'$  are the coordinate directions formed by the three sensors and  $i = 1, \dots, 8192$ ). The block mean,  $\bar{U}_j$  is then defined as

$$\bar{U}_j = \frac{1}{N} \sum_{i=1}^N U_{j,i} . \quad (4.2)$$

For each block the mean is calculated for all three velocity components and the temperature. The block standard deviations, denoted by  $\sigma_j$ , are defined by

$$\sigma_j = \left\{ \frac{1}{N} \sum_{i=1}^N U_{j,i} * U_{j,i} - \bar{U}_j * \bar{U}_j \right\}^{1/2} \quad (4.3)$$

The probe-yaw angle,  $\beta$ , for each block can be found by the following

$$\beta = \tan^{-1} \left\{ \frac{-1.22475 \times (\bar{U}_2 - \bar{U}_3)}{\bar{U}_1 + \bar{U}_2 + \bar{U}_3} \right\}, \quad (4.4)$$

due to the geometry of the probes.

With these quantities at hand, for all available data blocks, it is now possible to apply a nonstationarity trend test. If  $A^i$ ,  $i = 1, 2, \dots, m$  represents any of the statistical quantities calculated in the  $i^{\text{th}}$  block, the total number of reverse arrangements,  $R$ , is defined as

$$R = \sum_{i=1}^{m-1} \sum_{k=i+1}^m R_{ik} \quad (4.5)$$

where

$$R_{ik} = \begin{cases} 1 & , \quad \text{if } A^i > A^k \\ 0 & , \quad \text{if } A^i \leq A^k \end{cases}, \quad (4.6)$$

In the event that a set of block variables shows an upward trend, the total number of reverse arrangements will be some relatively large number. Also, if a set has a downward trend in magnitude, the total number of reverse arrangements will be a small number. If there is no real trend in the set then the total number of reverse arrangements will be some intermediate number [11].

The stationary trend test is performed on the three velocity components, the magnitude of the velocity vector and the probe-yaw angle, as well as for the standard deviations of the three velocity components and the temperature. If a normal distribution is assumed for the total number of reverse arrangements, then there exists an interval  $[R_1, R_2]$  for the values of  $R$ , such that a certain level of

confidence can be assumed, that there are no monotonic trends in the data sample. For values of  $R < R_1$ , a downward trend can be expected and for  $R > R_2$ , an upward trend is expected. The limits of the stationarity interval have been calculated in reference [11].

There are two methods available for stationarity test: a) visual inspection of the block means, and b) total number of reverse arrangements. Based on these facts a decision can be made whether or not to continue with the statistical analysis.

#### 4.3.3 Mean and Sample Covariances

The three velocity components in the sensor oriented coordinate system, determined by the direction of the sensors on the TSI probes, must be transformed into components in the mean wind coordinate system so as to obtain the desired statistical quantities. The three velocity components,  $u$ ,  $v$  and  $w$  in the mean wind oriented coordinate system, are found through the following transformation.

$$\begin{Bmatrix} u \\ v \\ w \end{Bmatrix} = E_{ijk} \begin{Bmatrix} U_1 \\ U_2 \\ U_3 \end{Bmatrix}, \quad (4.7)$$

where  $E_{ijk}$ , the direction cosines are a function of sensor geometry and probe-yaw angle,  $\beta$ .

The mean wind oriented coordinate system consists of 3 coordinate directions, the  $z$ -axis which is vertically upward, and the  $x$  and  $y$  axes which are horizontal. The system is aligned in such a manner that the direction of the sample mean wind lies parallel to the  $x$ -axis. Then,

by definition, the y-component of the sample mean velocity is zero. Also, since the flow in the atmosphere is most nearly horizontal, the z-component of the sample mean velocity will be small in comparison with the x-component. It should be pointed out that each level on the tower will have its own x-direction.

Now with the transformation of the velocity components into the mean wind coordinate system complete, the time histories to be analyzed are the longitudinal velocity component,  $u$ , the lateral velocity component,  $v$ , the vertical velocity component,  $w$ , and the temperature  $T$ . As was the case with the stationarity test, each time history will be divided into blocks with  $N = 8192$  data points per block. Block means are again calculated as before, but now using the transformed components, from the expression

$$\bar{x}_m = \frac{1}{N} \sum_{i=1}^N x_i, \quad (4.8)$$

where  $x$  can represent any one of the quantities,  $u$ ,  $v$ ,  $w$ , or  $T$ , and  $m$  is the reference to the data block. These block means are then averaged to obtain the sample mean values  $\bar{x}$ , for the complete time history as follows

$$\bar{x} = \frac{1}{m} \sum_{n=1}^m \bar{x}_n. \quad (4.9)$$

With the block means at hand it is now possible to calculate the variances and covariances since their values are obtained from time histories with a zero mean. The block variances,  $\bar{x}_m^2$ , and block covariances,  $\bar{xy}_m$ , are then calculated as



$$\overline{x_m^2} = \frac{1}{N} \sum_{i=1}^N (x_i - \bar{x}_m)^2 \quad (4.10)$$

and

$$\overline{xy}_m = \frac{1}{N} \sum_{i=1}^N (x_i - \bar{x}_m)(y_i - \bar{y}_m) \quad (4.11)$$

respectively.

The sample-variances,  $\overline{x^2}$ , and sample-covariances,  $\overline{xy}$ , are calculated as the average of the block-variances and block covariances as follows

$$\overline{x^2} = \frac{1}{m} \sum_{n=1}^m \overline{x_n^2} \quad , \quad (4.12)$$

$$\overline{xy} = \frac{1}{m} \sum_{n=1}^m \overline{xy}_n \quad .$$

The data, in the mean wind oriented coordinate system with the mean removed, are then rerecorded on a nine track magnetic tape and await spectral analysis.

#### 4.3.4 Spectra

The velocity components are now available in the mean wind oriented coordinate system with their mean removed. An efficient method of interpreting large amounts of data, as in this case, is to observe its behavior within the frequency domain. A function that describes the general frequency composition of a measured real and random quantity, say  $x(t)$ , is the power spectral density function,  $S_x(f)$ , which is expressed as

$$S_x(f) = 2 \cdot \lim_{T \rightarrow \infty} \frac{1}{2T} \left\{ \int_{-T}^T x(t) e^{-i2\pi f t} dt \right\}^2, \quad (4.13)$$

where  $f$  is frequency.

The joint properties of two real and random functions of time,  $x(t)$  and  $y(t)$ , in the frequency domain, are described by the cross-spectral density function,  $S_{xy}(f)$  which is expressed as

$$S_{xy}(f) = 2 \cdot \lim_{T \rightarrow \infty} \frac{1}{2T} \left\{ \int_{-T}^T x(t) e^{+i2\pi f t} dt \cdot \int_{-T}^T y(t) e^{-i2\pi f t} dt \right\} \quad (4.14)$$

The estimates of  $S_x(f)$  and  $S_{xy}(f)$  will be necessary in order to study the physical properties of the process in terms of its behavior within the frequency domain. The power spectrum will show how the variance or average power of the process is distributed over the entire frequency range. The spectral estimates are obtained by using the fast Fourier transformation of the discrete time series  $x_i$ , directly. A special program was developed for this purpose and is discussed in reference [11]. The first step is to obtain the Fourier transformation of the data in each block,

$$H_f = \Delta t \sum_{n=1}^n x_j e^{-i2\pi f j / n} W(j), \quad f = 0, 1, 2, \dots, n-1 \quad (4.15)$$

where  $W(j)$  is a data window, and  $\Delta t$  is the time increment (.005 seconds for the data of the TSI probes). This data window serves much the same purpose as an electrical filter and in general will change the mean and variances of the data sample since unequal weights are given to different portions of the time series. In effect, some data are destroyed

and as a result, degrees of freedom are lost; therefore, a scale factor is introduced to compensate for this loss in order to obtain accurate spectral estimates.

The power spectral estimate is then obtained as follows

$$S_x(f) = \frac{2}{n\Delta t} H_f H_f^* , \quad (4.16)$$

where  $H_f^*$  is the complex conjugate of  $H_f$ . A very thorough review of the spectral analysis technique is given in reference [11].

As a result of sampling data at equal time intervals,  $\Delta t$ , and later confusing some of the higher frequency contents with the lower frequency the problem of aliasing arises. Therefore bounds must be determined for the frequency interval for which we wish to obtain spectra. The Nyquist or folding frequency,  $f_s$ , determines the highest frequency at which data can be obtained without introducing aliasing errors and is expressed as

$$f_s = \frac{1}{2\Delta t} . \quad (4.17)$$

The lowest frequency at which data should be obtained is given by the following expression

$$f_l = \frac{1}{n\Delta t} , \quad (4.18)$$

where  $n$  is the total number of data points per block. Even though these bounds are imposed, some aliasing is still to be expected. One reason for this is that the 100 Hz low pass filter, discussed in section 4.2, is not perfect. Figure 3 shows the difference between the actual response of the filter and its ideal response.

As mentioned before, spectral estimates are calculated for each block. In order to obtain the spectral estimates for the complete time history, these block-spectral estimates,  $S_x^m$  and  $S_{xy}^m$ , must be averaged or smoothed. A combined smoothing technique is employed which first averages all of the block estimates and then averages over appropriate frequency intervals. Since energy is distributed nonuniformly over the entire frequency range, the frequency intervals for frequency smoothing are longer at the high frequency regions, where less power is present, and shorter at the low frequency regions, where more power is present. This type of smoothing yields more stable estimates for the complete time histories of one-hour duration.

#### 4.3.5 Conversational Monitor System

One attractive feature of the IBM-370 at V.P.I. & S.U. is the Conversational Monitor System (CMS). The VM/370 is a resource managing system running on one of the IBM-370 model 158's. It consists of a Control Program (CP) and the CMS. This allows a programmer to create, edit and execute programs in a conversational mode from a remote terminal. When large amounts of data are to be processed it frees the programmer from the burden of cards and greatly reduces the time in the manipulation of data sets. Also, the output from these programs can be stored within CMS and recalled later for further data reduction.

#### 4.3.6 Calculation of Covariances and Variances from Cospectra and Spectra

The covariances and variances are related to the cospectra and spectra, respectively, by the following relations

$$\overline{xy} = \int_0^{\infty} S_{xy}(f) df \quad (4.19)$$

and

$$\overline{x^2} = \int_0^{\infty} S_x(f) df . \quad (4.20)$$

Multiplication and division of the integrands by the frequency  $f$  leads to

$$\overline{xy} = \int_0^{\infty} f \cdot S_{xy}(f) d(\ln f) \quad (4.21)$$

and

$$\overline{x^2} = \int_0^{\infty} f \cdot S_x(f) d(\ln f) . \quad (4.22)$$

The variances and covariances obtained by this method, calculated over a finite frequency interval, can be compared to the values obtained from section 4.3.3 and should yield the same results.

Since the response of the thermocouples on the TSI probes is limited to 16 Hz, the variance of the temperature and the covariances involving the temperature, obtained by this integration process are used rather than the values that are calculated in section 4.3.3. By integrating only up to a frequency of 16 Hz, this will eliminate the electronic noise introduced in the frequency range of 16 Hz to 100 Hz.

## CHAPTER V

### DISCUSSION OF RESULTS

As was mentioned earlier, the data was gathered with instruments mounted on a 250 foot meteorological tower located at Wallops Island, Virginia. The island is bordered on the east by the Atlantic Ocean and on the west by a tidal flat consisting mainly of short grass and some water. The shore line of the island runs approximately in a northeast-southwest direction (Fig. 4). The 175-foot tall Aerobee launching tower is located at a distance of 1000 feet to the south-southwest from the meteorological tower. The distance from the edge of the ocean to the tower in the southerly direction is approximately 1000 feet.

Previous data has indicated that during the summer months a majority of the flows are from the south. Until recently, data were only collected during the summer with the probes mounted on the south side of the tower. Originally, thirteen one-hour data runs were taken; however, the last four were ignored because the flow passed intermittently through the tower before reaching the probes. As Table 1 shows, the nine runs which were analyzed are obtained from near southerly winds. The values of the direction angle,  $\phi$ , in Table 1 give the direction of the mean wind-vector measured clockwise with respect to north. It is from these nine runs that the following results will be discussed.

### 5.1 Mean Flow and Integral Statistics

The type of flow discussed in Chapter III does not differ greatly from the observed flow at Wallops Island. All obtained data are from southerly directions, with the flow originating over the Atlantic Ocean and approaching the shore of Wallops Island diagonally, crossing a narrow row of sand dunes (approximately 10 feet above sea level) and passing some other obstructions, such as the Aerobee tower, before arriving at the 250-foot meteorological tower. Keeping in mind the aforementioned type of flow, one would expect to find a lower, unstable layer of air (IBL) and an overlying stable air layer especially during warm summer afternoons. The flux Richardson numbers,  $R_f$ , (Table 1) depict such a flow. For every run the sign of  $R_f$  changes from negative at the 50-foot level to positive at the 100-foot level, indicating that the heat flux in the IBL is upward and downward in the inversion layer. Consequently, it may be concluded that the base of the inversion is somewhere between 50 and 100 feet ( $R_f = 0$ ). The prevailing on-shore winds from the south during a sunny summer day, crossing the shore at an angle of approximately  $45^\circ$ , give rise to a three dimensional type flow. As a result of the change in roughness, the flow near the surface may experience some change in direction because the velocity component normal to the beach is retarded more than the component parallel to the beach. However, this effect is not observed near the meteorological tower. In the IBL, the surface temperature is larger than the temperature of the air off the ocean and the vertical heat transfer is responsible for heating the air at higher elevations.

On the other hand, air near the surface, but to the west of the tower, has travelled further over land and can be expected to be warmer than air at the same elevation but just to the east of the tower. This should result in a turbulent heat transfer from west to east, or  $\overline{v^T \theta^T}$  should be negative at these lower levels in the IBL. Similarly, the air to the west of the tower has travelled further over land and should have slowed down more than the air to the east, which theoretically should lead to  $\overline{u^T v^T} > 0$  at the lower levels. The air, as it travels over land picks up heat and consequently one can expect a turbulent heat flux in the negative x-direction, or  $\overline{u^T \theta^T} < 0$  in the IBL. These predictions are not always exactly verified by the experimental results. However, the experimental results such as the mean velocity and mean temperature distribution as well as the turbulent fluxes indicate that the flow is far from homogeneous or one-dimensional, and therefore is not governed by the set of equations 2.22 through 2.27. The flow over land just past the shoreline is governed by the change in roughness, the change in surface temperature, the angle of the flow with the shore line and the thickness of the inversion layer above the ocean (Fig. 2). All these factors influence the type of flow one encounters at the 250-foot meteorological tower.

For most of the runs, the velocity profiles when plotted in the usual semi-logarithmic fashion show one or more "kinks". However, extrapolation of the velocity distribution at 50 and 30 foot elevations lead to extremely high roughness lengths,  $z_0$ , especially for runs 2, 7, 8 and 9 ( $z_0 > 1$  foot). Typical values for the roughness



parameter for onshore winds are of the order 0.04 inches or less. A slight adjustment may be necessary to take care of the stability effect, however, the flow in the lower 50 feet is near neutral. These extremely high roughness lengths indicate an abnormal boundary layer with velocities at the upper levels much higher than under normal conditions when large-scale turbulence provides a much more uniform velocity profile. In the absence of large eddies or in the absence of any mechanism to slow the flow down, Coriolis effects may become sufficiently important to affect the flow. The results do indicate this effect and runs 1, 7 and 8 show a maximum clockwise rotation of the flow of 4 to 10 degrees between the 50 and 250 foot level for each run.

The mean temperature distribution for the 9 runs do not show a log-linear distribution. Instead they show several "kinks" usually between the 100 and 150 foot levels. The most interesting sequence of mean temperature distributions is from runs 7, 8 and 9 (Fig. 5) which were taken on the afternoon of August 13, 1976 starting at 2:12 P. M., 3:37 P. M. and 5:05 P. M., respectively. The first two runs show a decrease in temperature up to the 100 foot level and an increase in temperature for higher elevations. The temperature decreases with height in the IBL, and in the case the upstream inversion layer is higher than 250 feet the temperature should decrease with height above the IBL (Fig. 2). Apparently as the afternoon progresses, the positive temperature gradient of the upstream inversion layer is decreasing. The run starting at 5:05 P. M. shows a decrease in surface temperature

with a subsequent cooling trend in the lower 50 feet. This cooling has not yet affected the air above 50 feet. Between 100 and 150 feet the temperature is increasing, indicating that the height of the upstream inversion layer has decreased to 150 feet.

Runs 3 and 4, taken on the afternoon of August 5, 1976 starting at 1:49 P. M. and 3:37 P. M., respectively, as well as runs 5 and 6 taken on the afternoon of August 12, 1976 show very similar temperature distributions. The temperatures decrease with height up to the 100 foot level, then show a slight increase between the 100 and 150 foot levels and decreasing temperatures above the 150 foot level. This seems to indicate that the height of the upstream inversion layer during these afternoons was constant and approximately 150 feet.

The standard deviations of the three velocity components normalized with the local shear velocity,  $\sigma_\alpha/U_\star$ ,  $\alpha = u, v, w$ , are plotted in Figures 6, 7 and 8 versus the stability parameter  $z/L$ , where the different symbols indicate different elevations. For near neutral conditions the average values of  $\sigma_\alpha/U_\star$  are 1.75, 1.5 and 1.4, respectively. No simple relationship between  $\sigma_\alpha/U_\star$  and  $z/L$  exists according to these results. The plots indicate that the values of  $\sigma_\alpha/U_\star$  increase for deviations from the neutral conditions in both the stable and unstable regime.

The values of the covariance of  $\overline{u'w'}$  are all negative as expected. In the spectral analysis, the local shear velocity,  $U_\star = \sqrt{-\overline{u'w'}}$ , was used to non-dimensionalize the spectral values (Figs. 16, 17, 18), and the results match the Kansas data [7], showing that the  $\overline{u'w'}$  covariances

are accurate. The  $\overline{w'\theta'}$  covariances show positive values in the IBL and negative values in the overlying inversion layer. The magnitude of the covariances are probably not too reliable as a result of electronic noise entering the thermocouple circuits. In addition, the thermocouples have a flat frequency response up to maximum of 16 Hz and the voltage representing the temperature was digitized at the same rate as the voltages from which the velocities were obtained. At the present time it is not quite clear how reliable these covariances are. Except for the 50-foot level, the covariances have low magnitudes and therefore noise may influence these results as well as their cospectra.

At the present, data are taken from the north side of the tower with flow approaching over the tidal flat with a relatively uniform terrain roughness. The results should not show an IBL, and the heat flux should be either positive or negative and not mixed as is the case for the data currently analyzed. Temperature data should be available from all levels, however for the current data none was available for the 30-foot level or the 250-foot level in runs 5, 6, 7, 8 and 9. In addition, the thermocouple circuit has been completely redesigned and should give more reliable data. The results from the north side of the tower should match the data available from other sources much better. After this comparison has been made a definite conclusion can be made as to the accuracy of the temperature measurements.

The characteristic length scale of the energy containing eddies can be obtained from the normalized autocorrelation function with the use of Taylor's hypothesis

$$L_X^u = U \int_0^{\infty} R(\tau) d\tau \quad (5.1)$$

This is referred to as the integral length scale for the streamwise velocity fluctuations. In table 1 the values of  $L_X^u$  were obtained from the measurements made with the NASA cup-vane instruments. This type of instrumentation does not respond to high-frequency velocity fluctuations and therefore the calculated values for  $L_X^u$  may be somewhat high.

An alternate method for obtaining a measure of the scale of the energy containing eddies is the wave length corresponding to the reduced peak frequency of the logarithmic velocity spectra:

$$\lambda_m^u = z/f_m^u \quad (5.2)$$

Kaimal [6] gives the following relation for these two length scales

$$\lambda_m^u \approx 2\pi L_X^u \quad (5.3)$$

This relation is based on the assumption that the normalized logarithmic spectra in the low-frequency range vary linearly with  $f/f_0$  down to zero reduced frequency. According to the results listed in Table 1, there does not seem to exist a simple relation between  $\lambda_m^u$  and  $L_X^u$ . For most runs  $\lambda_m^u > L_X^u$  for the unstable flow in the IBL. This trend is reversed for the stable flow above the IBL, the integral length scale,  $L_X^u$ , is in most cases larger than  $\lambda_m^u$  by a factor of 1.5 - 2.0.

## 5.2 Spectra and Cospectra

The M-0 similarity states that the logarithmic spectrum functions,  $n S_{\alpha}(n)$ , normalized with the shear velocity,  $U_{*}$ , should be universal functions of the reduced frequency,  $f = \frac{nZ}{U}$ , and the dimensionless height,  $z/L$ , so that

$$\frac{n S_{\alpha}(n)}{U_{*}^2} = F_{\alpha}\left\{f, \frac{z}{L}\right\} \quad \alpha = u, v, w \quad (5.4)$$

Panofsky [10] found that the vertical spectra obey similarity theory up to a height of approximately 50 m. The longitudinal and lateral velocity spectra however did not obey the M-0 similarity theory. In later years when more reliable data over a larger frequency range became available, notably the Kansas data (Kaimal et al. [7]), the above findings were corroborated.

Vertical velocity spectra obtained at different heights along a meteorological tower show a systematic shift towards higher frequencies. These observations led to the modification of the frequency scale to  $f/f_m$ , where  $f_m$  represents the value of  $f$  at the peak of the logarithmic spectrum functions. Because of the flatness of the logarithmic spectra at the peak, accuracy of  $f_m$  is poor. Kaimal et al [7] suggested to modify the frequency scale to  $f/f_0$ , where  $f_0$  is the intercept of the inertial subrange with the line  $n S_{\alpha}(n)/\sigma_{\alpha}^2 = 1$ .

Further studies indicated that the spectra were best described by normalizing the logarithmic spectra and cospectra with their respective variances and covariances. If the variances and the reduced peak frequency,  $f_m$ , or  $f_0$  are universal functions of  $z/L$  then M-0

similarity theory should be applicable.

Using Kolmogorov's law in the inertial subrange and based on available data, Busch [1] proposed to normalize the logarithmic spectra with the parameter  $(\kappa \epsilon \lambda_m)^{2/3}$ , where  $\kappa$  is von Karman's constant,  $\epsilon$  the dissipation rate and  $\lambda_m \left[ \lambda = \frac{U}{n} \right]$  is the wave length at the peak of the logarithmic spectrum of the vertical velocity component. This normalizing scheme collapses the spectral data in the inertial subrange for  $f/f_m > 0.2$ , but in the low frequency range, a systematic variation of the spectra with stability is observed. In order to take care of all the variations in the low frequency range, Busch [5] proposed the following expression for the normalized logarithmic spectra for all stability ranges

$$\frac{n S_\alpha(n)}{(\kappa \epsilon \lambda_m)^{2/3}} = g_\alpha \left( \frac{f}{f_m}, \xi_i \right) F_\alpha \left( \frac{f}{f_m} \right), \quad (5.5)$$

where  $g$  is the same function for all three velocity components. The function  $g$  is unity in the inertial subrange  $f/f_m \geq 0.2$  and dependent on the normalized reduced frequency and external parameters which modify the spectra in the low frequency range. The external parameters are represented by the symbol  $\xi_i$  which include long-term trends, other nonstationarities, terrain roughness, nonhomogeneities in terrain roughness and surface temperature variations, and variations in data processing. The determination of the dependence of  $g$  on the external parameters mentioned above is a rather formidable task. The spectral results obtained in this research program at heights up to 250 feet and over a nonhomogeneous surface are to be compared with the spectral

results obtained in the surface layer from previous experiments.

In the following the frequency spectra, and not the wave number spectra are used. The two forms of the spectra are related by the use of Taylor's hypothesis, so that

$$\int_0^{\infty} S_{\alpha}(k) dk = \sigma_{\alpha}^2 = \int_0^{\infty} S_{\alpha}(n) dn . \quad (5.6)$$

The wave number (radians per unit length) is related to the frequency as  $k = 2\pi n/U$ , and consequently  $k S_{\alpha}(k) = n S_{\alpha}(n)$ , which is referred to as the "logarithmic" spectral form. For engineering applications as well as for future comparison purposes it is advantageous to normalize the logarithmic spectra with the variance,  $\sigma_{\alpha}^2$ , rather than using the surface shear velocity,  $U_{*0}$ . In many occasions, the shear velocity is not available and it is often difficult to measure. However, the M-0 hypothesis predicts that the variances normalized with the shear velocity are universal functions of  $z/L$ , which then leads to

$$n S_{\alpha}(n)/\sigma_{\alpha}^2 = F_{\alpha}(f, z/L) . \quad (5.7)$$

All frequency spectra are defined such that

$$\int_0^{\infty} (n S_{\alpha}(n)/\sigma_{\alpha}^2) d(\ln n) = 1 \quad (5.8)$$

For stationary and high Reynolds number flows Kolmogorov's law predicts an inertial subrange for velocity spectra and temperature spectra. In this wave number range the turbulence is transferred from low wave numbers to high wave numbers without being affected by production or dissipation. Dimensional arguments then lead to the following

relation in the inertial subrange:

$$F_{\alpha}(k) = K_{\alpha} \epsilon^{2/3} k^{-5/3}, \quad \alpha = u, v, w. \quad (5.9)$$

where  $K_{\alpha}$  are the Kolmogorov constants

$$K_v = K_w = \frac{4}{3} K_u. \quad (5.10)$$

For the temperature spectra, Corrsin [ 3 ] proposed the following form for the inertial subrange

$$F_{\theta}(k) = K_{\theta} N \epsilon^{-1/3} k^{-5/3}, \quad (5.11)$$

where  $N$  is the rate of dissipation of  $\frac{1}{2} \overline{\theta'^2}$ . The universal constant,  $K_u$ , for the Kansas data [ 7 ] is 0.5, which according to other estimates is an acceptable value. The value for  $K_{\theta}$  is not well established, however an indirect method used for the Kansas data estimates this constant to be of the order of 0.8.

### 5.2.1 Spectra of Velocity

The spectra and cospectra measured in this research program fall in the stability range of moderately unstable to extremely stable. Because of the type of flow encountered, the spectra from the 30 and 50 foot level fall in the moderately unstable group ( $-1 < z/L < 0.0$ ). For higher levels, the air was stable and the spectra were placed either in the moderately stable category ( $0 < z/L < +1.0$ ) or the strongly stable category ( $z/L > +1.0$ ). The turbulence intensity levels at the two lower levels are much higher than in the stable air above 50 feet. Under stable conditions the values of  $\sigma_{\alpha}$  are very low



(1 fps or less), and often the spectral measurements in the high frequency range are affected by electronic noise as well as possible aliasing. The spectra were initially plotted in similarity coordinates  $n S_{\alpha}(n)/\sigma_{\alpha}^2$  and  $f = nz/U$ . All spectra showed a clear  $-2/3$  region in the high frequency range. The peaks of the logarithmic spectra are of the order of 0.32. With increased height and increased stability the spectra are being shifted systematically to higher reduced frequencies. Spectral values up to 100 Hz were calculated, however 60 cycle noise could be clearly recognized and aliasing occurred in this high frequency region notwithstanding the applied low pass filtering at 100 Hz. Some spectra, especially those obtained above the 50-foot level occasionally showed aliasing or some scatter at the higher frequencies. The lowest frequency at which spectral values were calculated is 0.0244 Hz. For most runs, 75 blocks of  $8192 = 2^{13}$  data points each were analyzed. This means that the spectral value at the lowest frequency is based on a maximum of 75 occurrences. Stable spectral estimates at low frequencies should be based on at least 100 occurrences and preferably more. Consequently, the first 6 spectral values in the low frequency range show some scatter. For the vertical and lateral spectra these are the points which determine the spectral shape for frequencies smaller than the frequency where the spectral peaks occur. For both the lateral and vertical velocity spectra the slope of the log-log spectra plots in the low frequency range is of the order of unity. For the longitudinal velocity spectra the first six spectral values do not show a definite trend and a spectral peak

is often difficult to discern.

Only for the vertical spectra the reduced peak-frequencies,  $f_m$ , were determined and the spectra were grouped in the before mentioned stability categories. The spectra in each group were graphically represented on a single plot using the modified reduced frequency of  $f/f_m$  (Fig. 9). The spectra from the moderately unstable category originated in the internal boundary layer and the spectra for the two stable groups all originated in the overlying stable air.

The spectra in the moderately unstable category collapse very nicely; however, the spectra in the two stable categories showed some scatter. The logarithmic spectra have a low frequency variation of  $f/f_m$  and a  $f/f_m^{-2/3}$  variation in the high-frequency range for  $f/f_m \geq 0.5$ . Table 2 shows average peak spectral values and average reduced peak frequencies for the three stability categories. The average values for the reduced peak frequencies correspond quite well to the results reported by Kaimal et al (Fig. 18) [7].

Busch and Panofsky [2] and Kaimal et al. [7] have found that near-neutral vertical-velocity spectra are well described by the following empirical expression

$$\frac{n S_w(n)}{\sigma_w^2} = \frac{A(f/f_m)}{1 + B(f/f_m)^{5/3}} \quad (5.12)$$

The constant A is determined in such a way that the computed value of  $n S_w(n)/\sigma_w^2$  at  $f/f_m = 1.0$  and the maximum observed value are equal.

The constant B can be varied to fit the data at either the high or the

low frequency range. No single value for B exists to fit the data simultaneously at both spectral legs and the peak. In addition, the above empirical expression should integrate to a value close to unity.

The vertical spectra in the stable categories are reasonably well approximated by the expression (5.12), with  $A = 0.685$  and  $B = 1.5$ . The vertical spectra in stable air at higher elevations become broader for increased stability and consequently it is more difficult to locate the spectral peak accurately. Instead of trying to fit a single expression to the spectra it is more convenient and more accurate to determine the intercepts of the extrapolated low-frequency and high frequency spectral legs with the line  $n S_{\alpha}(n)/\sigma_{\alpha}^2 = 1$ . These intercepts as well as the peak spectral values are also listed in Table 2.

In order to deal with the uncertainty of the location of the spectral peaks, especially for those spectra from stable air, Kaimal et al [7] modified the frequency scale to  $f/f_0$ , where  $f_0$  is the intercept of the  $f^{-2/3}$  line in the inertial subrange with the line  $S_{\alpha}(n)/\sigma_{\alpha}^2 = 1$ . This normalization scheme collapses all spectra to a single curve in the inertial subrange. Kaimal et al [7] suggested the following empirical expression to describe the spectra:

$$\frac{n S_{\alpha}(n)}{\sigma_{\alpha}^2} = \frac{A(f/f_0)}{1 + A(f/f_0)^{-5/3}}, \quad (5.13)$$

where A is a constant determined by the line of best fit in the low frequency range. The spectral peak for this expression is located at  $f/f_0 \approx 3.8$ , which leads to a spectral peak value of 0.25 with  $A = 0.164$ .

In Figures 10, 11 and 12 the longitudinal, lateral and vertical velocity spectra from this study are plotted against the modified frequency  $f/f_0$  for the three stability categories. The u-spectra show a great deal of scatter in the low frequency range and no single curve can be fitted to the data in this range. In addition, their spectral peaks are difficult to recognize. The lateral and vertical spectra show excellent similarity for all three stability categories. In all cases the logarithmic spectra vary linearly with the modified frequency  $f/f_0$ , although the intercepts with the line  $n S_\alpha(n)/\sigma_\alpha^2 = 1$  vary somewhat with stability (Table 3). The spectral peaks fall between 0.27 and 0.32 which is higher than the value predicted by Kaimal's empirical equation of 0.25.

The intercepts for the low frequency legs of the v and w spectra have higher values in moderately unstable air than in stable air (Table 3). This indicates that the stable spectra are broader. The stable spectra are obtained at higher elevations (above the IBL) and therefore these spectra are obtained in air which has not yet been influenced by the presence of the land surface. Busch and Panofsky [2] also noted that spectra over the sea have relatively more energy at low frequencies than those over land. In addition, the vertical spectra seem to be somewhat broader than the lateral spectra.

The variation in reduced frequencies where the spectral peaks occur does not seem significant; the average value for  $f_m/f_0$  is approximately 3.3. The Kansas spectra [6] for stable conditions show a spectral peak at  $f_m/f_0 \approx 3.8$ . The intercept of the low frequency

leg for the stable Kansas spectra is of the order of 6.1, which is somewhat higher than for the stable Wallops data. Again, this verifies that spectra over the ocean have somewhat higher spectral levels at low frequencies than over land. In general, it can be seen that the Wallops spectra are remarkably similar to the Kansas spectra. If spectra follow the M-0 similarity it will be necessary that among other things,  $f_m$  or  $f_0$  are unique functions of  $z/L$ . Figures 13, 14 and 15 show the variation of the reduced peak frequencies  $f_m$  of the vertical, longitudinal and lateral velocity spectra with stability. For moderately stable conditions ( $0 < z/L < +2.0$ ) the results seem to follow the Kansas data quite well. For very stable conditions, the values of  $f_m$  do not show the same trend as was established in the moderately stable range. The very stable conditions were encountered at the higher elevations, which means that at these heights the air has not been affected by the land and is still governed by the conditions above the ocean.

Using Kolmogorov's Law (5.9) for the inertial subrange and the relation between wave-number spectra and frequency spectra, the logarithmic spectra normalized with the shear velocity,  $U_*$ , become

$$\frac{n S_\alpha(n)}{U_*^2} = \frac{K_\alpha}{(2\pi \kappa)^{2/3}} \left( \frac{\kappa z \epsilon}{U_*^3} \right)^{2/3} \left( \frac{nz}{U} \right)^{-2/3} \quad (5.14)$$

Introducing the reduced frequency and the dimensionless dissipation function,  $\phi_\epsilon = \frac{\kappa z \epsilon}{U_*^3}$ , the above expression becomes

$$\frac{n S_{\alpha}(n)}{U_{*}^2} = \frac{K_{\alpha}}{(2\pi \kappa)^{2/3}} \phi_{\epsilon}^{2/3} f^{-2/3} \quad (5.15)$$

In order to compare the spectra in the inertial subrange, the measured values of  $n S_{\alpha}(n)/U_{*}^2$  evaluated at  $f = 10$  are compared with the calculated values obtained from empirical expressions for the dimensionless dissipation rate,  $\phi_{\epsilon}$ .

These expressions are presented by Wyngaard and Coté [13], and relate  $\phi_{\epsilon}$  with the stability parameter  $z/L$ :

$$(\phi_{\epsilon})^{2/3} = 1 + 0.5 |z/L|^{2/3}, \quad -2.0 \leq z/L \leq 0 \quad (5.16)$$

and

$$(\phi_{\epsilon})^{2/3} = 1 + 2.5 |z/L|^{3/5}, \quad 0 \leq z/L \leq +2.0. \quad (5.17)$$

The basis for these expressions are the Kansas results and the independent evaluation of the dissipation,  $\epsilon$ , was obtained through time differentiation of the longitudinal velocity component. With  $\kappa = 0.35$ , as was obtained from the Kansas data,  $K_u = 0.5$  and  $f = 10$ , the expression (5.15) becomes

$$\left[ \frac{n S_u(n)}{U_{*}^2} \right]_{f=10} = 0.0637 \phi_{\epsilon}^{2/3} \quad (5.18)$$

For the  $v$  and  $w$  spectra the constant in expression (5.18) is 0.0854. Figures 16, 17 and 18 show the measured results in comparison with the predictions from expressions (5.16), (5.17) and (5.18). For values of  $z/L < 3$  the agreement is quite good. However, for very stable conditions at the higher elevations, the Wyngaard-Coté expressions for the

dimensionless dissipation,  $\phi_\epsilon$ , do not match the data. Since the results do follow the predictions in the range  $z/L < 2.0$  ( $z/L = 2$  is the upper stability limit of the Kansas data), one may conclude that for the moderate stability range  $-1 \leq z/L \leq 2.0$ , the Wallops data appear to follow the Kolmogorov's law. Consequently, it is assumed that the spectral results in the inertial subrange can be used to obtain the dissipation,  $\epsilon$ . In expression (5.15) the logarithmic spectrum functions are normalized with the local shear velocity and not the shear velocity near the ground. Because of the good agreement between the results and the predictions, it can be concluded that it is quite appropriate to use the local shear velocities in the normalization schemes, calculations of the M-0 stability lengths and flux Richardson numbers. Using the Kolmogorov's Law, the velocity spectra can be normalized in the following form:

$$\frac{n S_\alpha(n)}{(\kappa z \epsilon)^{2/3}} = \frac{K_\alpha}{(2\pi\kappa)^{2/3}} f^{-2/3} \quad (5.19)$$

This normalization method collapses all spectra regardless of their stability classification in the inertial subrange. The plots of the logarithmic velocity spectra normalized in this fashion are shown in Figures 19, 20 and 21. The Kansas spectra in this form [7], which were obtained in the surface layer at three different heights, show systematic changes with stability in the low frequency range, especially for stable spectra. The low frequency range of the unstable spectra do not show the same systematic change with  $z/L$ . The Wallops data show somewhat similar features, however the data have not been analyzed for

sufficiently low frequencies to make conclusions about any systematic variations in the low frequency range. The Wallops spectra show the development of a similar trend in the low frequency range, but no excluded regions between stable and unstable spectra in the low frequency range can be discerned. The Kansas u, v and w spectra [7] all show a definite gap in the low frequency range when the stability parameter switches sign.

The Wallops spectra in the very stable category show two distinct groups, one with more energy at low frequencies and the other with distinctly less energy in this range. The spectra of the latter group are associated with runs 1, 7 and 8 and with elevations above the IBL. These three runs are the only ones which show a clear clockwise rotation of the wind direction at higher elevations. This Coriolis effect can only be important in the case that no large eddies are present in the stable layer and no mixing takes place between the IBL and the overlying inversion layer. Consequently, the spectra obtained in the stable layer when Coriolis effects are appreciable should show reduced energy levels at low wave numbers (large eddies).

From previous results it was already concluded that the values for  $\epsilon$  are in agreement with those of the Kansas data in the stability range  $-2.0 \leq z/L \leq +2.0$ . The fact that the spectra in the inertial subrange collapse for all three stability categories, using the universal constant  $K_u = 0.50$ , indicates that in very stable air the dissipation can be obtained from the Kolmogorov law.



Another useful presentation of the spectra is to normalize the spectral values with the variance and to modify the frequency scale according to the Kolmogorov law, to  $f/\phi_\alpha$ . Here,  $\phi_\alpha$  is the non-dimensional dissipation parameter  $\kappa z \epsilon / \sigma_\alpha^3$ , which should be a universal function of  $z/L$ . With  $K_U = 0.5$  and  $\kappa = 0.4$ , the spectral relations in the inertial subrange become:

$$n S_u(n) / \sigma_u^2 = 0.27 (f/\phi_u)^{-2/3} \quad (5.20)$$

and

$$n S_{v,w}(n) / \sigma_{v,w}^2 = 0.36 (f/\phi_{v,w})^{-2/3} \quad (5.21)$$

Figures 22, 23 and 24 show the velocity normalized in this fashion for each stability category. The modified frequency scales  $f/\phi_\alpha$  and  $f/f_0$  both should produce identical spectral shapes and collapse of the spectra in the inertial subrange. The latter requirement leads to a direct relation between  $f_0$  and  $\phi_\alpha$ . Since  $f_m/f_0 \approx 3.3$ , one obtains

$$f_m^u = 0.463 \phi_u \quad (5.22)$$

and

$$f_m^{v,w} = 0.713 \phi_{v,w} \quad (5.23)$$

Figures 25, 26 and 27 show that the measurements follow these expressions excellently for all stability categories. The above relations (5.20) and (5.21), valid in the inertial subranges should intersect the line  $\frac{n S_\alpha(n)}{\sigma_\alpha^2} = 1$  at the points  $f/\phi_u = 0.140$  and  $f/\phi_{w,v} = 0.216$ , respectively. The spectral results match these predictions for all three stability categories.

It would have been more meaningful if the dissipation,  $\epsilon$ , could have been obtained independently from the Kolmogorov law. By assuming isotropic turbulence the dissipation can be obtained from the variance of the instantaneous time derivatives of the turbulence. The assumption of local isotropy of the turbulence cannot only be based on the existence of a  $f^{-2/3}$  region in the logarithmic spectra. Another consequence for the one-dimensional velocity spectra in the inertial subrange is that the ratios  $S_w(n)/S_u(n)$  and  $S_v(n)/S_u(n)$  have the magnitude of 1.33. Figures 28 and 29 show a set of spectral ratios for simultaneous data. This was the best set of data available to show the approach to a ratio of 4/3 in the inertial subrange. For most measurements this requirement was not satisfied especially for spectra outside the IBL. At this time it is difficult to say whether this problem is due to a misalignment of the probes in the vertical plane, a data analysis problem, or that the turbulence is not yet sufficiently developed for this requirement to be satisfied. The answer should become clear as soon as data for winds from northerly directions become available. If it turns out that the turbulence in the IBL has not had sufficient time to develop, then it is questionable whether or not accurate estimates of the dissipation can be obtained from the variance of the time derivative of the velocity.

### 5.2.2 Spectrum of Temperature

The temperature spectrum has not been investigated as extensively as the velocity spectra. The form of the temperature spectrum in the inertial subrange has been proposed by Corrsin [3] as

$$F_{\theta}(k) = K_{\theta} \epsilon^{-1/3} N k^{-5/3} \quad (5.24)$$

or in terms of reduced frequencies

$$\frac{n S_{\theta}(n)}{\sigma_{\theta}^2} = \frac{K_{\theta}}{(2\pi)^{2/3}} \frac{N \epsilon^{-1/3} z^{2/3}}{\sigma_{\theta}^2} f^{-2/3} \quad (5.25)$$

Estimates of the universal constant,  $K_{\theta}$ , seem to center around 0.8.

$N$  represents the dissipation rate of  $\sigma_{\theta}^2/2$ , and has to be estimated from the temperature fluctuation production,  $\overline{w'\theta'} \frac{\partial \bar{\theta}}{\partial z}$ .

As figure 30 indicates, the measured temperature spectra will collapse to a single curve if the logarithmic spectra are normalized with the variance and the frequency scale is modified to  $f/f_0$ . Again  $f_0$  is the intercept of the line of best fit in the inertial subrange with the line  $n S_{\theta}(n)/\sigma_{\theta}^2 = 1$ . The temperature spectra plotted in these coordinates are also brought together in the low frequency range for all stability categories. A single expression,  $\frac{n S_{\theta}(n)}{\sigma_{\theta}^2} = 0.186 f/f_0$ , fits the measured spectra quite well in this range. The spectral peak,  $\left[ \frac{n S_{\theta}(n)}{\sigma_{\theta}^2} \right]_{\max}$ , for the moderately unstable category is 0.29. The spectral peaks of the temperature spectra in the two stable categories are 0.32. In all cases the spectral peaks occur at the modified peak frequency of  $f_m/f_0 = 3.35$ . These results indicate that the temperature and velocity spectra nondimensionalized in the above manner are quite similar. It is impossible to present the entire temperature spectrum with a single empirical expression as suggested by Kaimal [6].

The logarithmic temperature spectra discussed above, all show a  $f/f_0^{-2/3}$  region, although some of these spectra show a steeper slope at

higher frequencies. Many spectra, especially those of runs 3, 4, 5 and 6 all show steeper slopes and no  $f/f_0^{-2/3}$  region at all. The magnitude of these slopes for the logarithmic spectra in the high frequency range lies between 1.0 and 1.2. At the present time it is not clear whether or not these steep slopes are real or not. Most temperature spectra show little or no scatter at all. A few show some aliasing at the higher frequencies. The temperature spectra were analyzed between 0.0244 Hz and 16 Hz, and the thermocouple and its electronic circuit show a flat frequency response in this range.

Figure 31 shows the variation of the reduced peak-frequencies for the temperature spectra with stability. The results suggest that for the same stability and the same height, the peak wavelength,  $\lambda_m$ , is smaller for the Wallops data than for the Kansas data. The values of  $f_m$  for the  $u$ ,  $v$ ,  $w$  and  $\theta$  spectra at neutral stability are 0.15, 0.35, 0.5 and 0.4, respectively. Kaimal et al. [7] compared temperature spectra of different sources, and the shift of the peak to higher reduced frequencies of the Bomex spectra taken over the ocean in comparison to the spectra of the other sources is very striking. The temperature data show a great deal of intermittency at higher elevations by just observing the voltage trace on a cathode ray tube. At one point during visual observation of a velocity voltage-trace from a probe at 200 and 250 feet, the fluctuations disappeared altogether as a result of extreme stability of the flow. A number of sources such as three-dimensionality of the flow, strong advection, measuring equipment and differences in data analysis may be responsible for the differences

between the Wallops and Kansas data. At the present, data are being acquired and analyzed from northerly directions. The wind approaches the tower over a tidal flat with some small stretches of water, and not over the ocean as is the case for the set of data discussed in this report. This new set of data should be very similar to the data taken by many other sources. If discrepancies still exist between the Wallops data and these other sources it can probably be blamed on either the instrumentation or the data analysis or both.

### 5.2.3 Cospectra of Reynolds Stress and Heat Flux

In this section the behavior of the  $uw$  and  $w\theta$  cospectra will be discussed. These are essentially the cospectra of the shearing stress and vertical heat flux respectively. These measurements are much more sensitive to instrument levelling and alignment than the measurement of power spectra. Often the correlation between the two variables is very small and electronic noise enters the cospectra. An additional problem in the  $w\theta$  cospectra is the limited frequency response of the temperature sensor (16 Hz) and a much higher response (approximately 1000 Hz) for the velocity sensors. Both the velocity and temperature voltages are being sampled at a rate of 200 samples per second and spectral information is available up to 100 Hz. Consequently, the values of the  $w\theta$  cospectra in the frequency range between 16 Hz and 100 Hz must be regarded as noise. No Kolmogorov law exists for the spectral variation in the inertial subrange; of course when the turbulence becomes truly isotropic at a certain wave number all

cospectra should vanish. Based on the measurements, the 4/3 ratio of the vertical or lateral velocity spectra and the longitudinal velocity spectrum seems to be satisfied for values of reduced frequency,  $f$ , of 5 or higher. The cospectra for both  $uw$  and  $w\theta$  seem to exist for maximum values of reduced frequency,  $f$ , of 10 to 100.

The  $uw$  cospectra collapse to a single curve if the logarithmic cospectra are normalized with the covariance and the frequency scale is modified to  $f/f_0$ . Here,  $f_0$  is the intercept of the line of best fit in the high frequency range with the line  $S_{uw}(n)/\overline{u'w'} = 1$ . The  $uw$  cospectra plotted in these coordinates show a great deal of similarity in both the low and high frequency ranges independent of stability (Fig. 32). The high-frequency and low-frequency ranges can best be fitted by the following expressions

$$\frac{n S_{uw}(n)}{\overline{u'w'}} = \begin{cases} (f/f_0)^{-4/3} & \text{for } f > f_0 \\ 1.69 (f/f_0) & \text{for } f < f_0 \end{cases} \quad (5.27)$$

$$(5.28)$$

Because of the scatter of the data the value of the spectral peak cannot be evaluated with a great deal of certainty; however a maximum value of  $\left[ \frac{n S_{uw}(n)}{\overline{u'w'}} \right]_{\max} = 0.42$  fits the available data best for all stability categories. The peak spectral value seems to occur at the modified frequency  $f_m/f_0 \approx 1.26$ . Because of the scatter of the  $uw$  cospectra the coefficients and exponents may not be as accurate as similar coefficients for the power spectra. Figure 33 shows the variation of the reduced-peak frequencies for the  $uw$  cospectra with stability. Again, for the moderately stable range  $0 < z/L < +2.0$  the results agree

reasonably well with those of Kaimal et al. [7] which were obtained in the surface layer. For very stable conditions outside the IBL, the values of  $f_m^{uw}$  do not follow the same trend as was established in the moderately stable range. Apparently,  $f_m^{uw}$  does not continue to increase with stability or the maximum wavelength does not continue to decrease with stability. Under very stable conditions  $z/L > +10$  the peak reduced frequency seems to be a constant in the order of 0.6. Similar conclusions can be drawn from the results of the peak reduced frequencies for the spectra of the velocity and temperature. The  $w\theta$  cospectra normalized by the covariance  $\overline{w'\theta'}$  and plotted versus reduced frequency shows a great deal of similarity. Some of these cospectra show both positive and negative values, especially the cospectra whose covariance is near zero. Of course, the stable air when entering the IBL shows a negative value (downward heat flux) and as soon as the stable air enters the unstable IBL the covariance must switch signs (upward heat flux). The process of changing the  $w\theta$  covariance from negative to positive does not take place instantaneously, but possibly starts at low wave numbers and gradually continues into the high wave number range. Only those  $w\theta$  cospectras were plotted which were either positive or negative in the entire frequency range (Fig. 34). For either the moderately unstable or the two stable categories the  $w\theta$  cospectra collapse to a single curve if the logarithmic cospectra are normalized with the covariance  $\overline{w'\theta'}$  and the frequency scale is modified to  $f/f_0$ . Here,  $f_0$  is the intercept of the best fitting line with a  $-4/3$  slope in the high frequency range,

with the line  $S_{w\theta}(n)/\overline{w'\theta'} = 1.0$ . Despite some appreciable scatter of the data, the high frequency range can best be fitted with the following expression

$$\frac{n S_{w\theta}(n)}{\overline{w'\theta'}} = 0.6 (f/f_0)^{-9/8}$$

This is a less steep slope than suggested by Kaimal [6] and less steep than encountered for the  $uw$  cospectra. The peaks of the logarithmic cospectra occur approximately at  $f/f_0 = 1.0$ , with a peak value of about 0.35. Figure 35 shows the variation of the reduced-peak frequencies for the  $w\theta$  cospectra with stability. In the moderately stable region the Wallops data follow the results of the Kansas data quite well. For very high stable thermal stratification the peak reduced-frequencies do not seem to follow any specific trend.



## CHAPTER VI

### CONCLUSIONS

This thesis describes the experimental study of the turbulent flow in a stable on-shore flow modified by changes in surface roughness and surface temperature. NASA cup-vane anemometers and temperature sensors and TSI hot-film anemometers and fine wire thermocouples were used for measurement of the variances and covariances and their spectra. These instruments were mounted on six levels along a 250-foot meteorological tower located adjacent to the shoreline on Wallops Island, Virginia.

The results indicate that the boundary layer in this flow is not an ordinary one. Due to the increased surface temperature that the stable flow off the ocean encounters as it crosses the shore an unstable internal boundary layer (IBL) develops. The vertical heat flux is positive in the IBL and negative in the overlying inversion. For the nine one-hour runs analyzed, the change in heat flux occurs somewhere between 50 and 100 feet. The magnitude of the variances of the turbulence and temperature as well as the magnitude of the fluxes decreases rapidly across the boundary between these layers. Mean velocity profiles indicate that the flow is not an ordinary boundary layer-type flow. The intercept of the semi-logarithmic velocity distribution with the z-axis is unusually high, indicating that the velocities are higher than usual in the inversion layer.

Mean temperature profiles indicate that the flow in the IBL is usually unstably stratified on warm summer afternoons. The mean temperature profiles above the IBL are governed by the depth of the undisturbed inversion layer off the ocean. If this depth is less than 250 feet then the mean temperature profile will show a "kink" just above the IBL and continue to decrease with height. In the case where the depth of the inversion layer is larger than 250 feet the temperature profile will show a continuous increase with height above the IBL.

The turbulence levels in the inversion layer above the ocean are extremely low. In certain instances where the conditions were extremely stable it has been observed that the turbulence at the 200 and 250 foot level completely disappear. Usually the turbulence does not disappear completely, but its power at low frequencies (large scale eddies) show an abnormal decrease. Under these conditions the air in this layer has no dynamic contact through large-scale mixing with the IBL and the remainder of the planetary boundary layer (PBL) above it. As a result, Coriolis forces become important and the inversion layer shows, in addition to an excessively high velocity, also an appreciable clockwise change in direction. The maximum change in direction between the top of the IBL and the 250 foot level has been measured at 10 degrees.

The standard deviations of the three velocity components normalized with the local shear velocity show normal values for near neutral stability but show a great deal of scatter with increased stability. This scatter is attributed to the uncertainty in the

measurements of the covariances because of their low values. However, at the 250 foot level the peak wavelengths of all three velocity components show their lowest values for those runs with the greatest Coriolis effects. This shows that the large scale eddies promote mixing between the layers, and in the absence of these large scale eddies not enough mixing occurs and as a result the flow does not encounter any retarding effect. In addition, Coriolis forces gain importance and result in a noticeable clockwise rotation of the wind direction above the IBL.

The  $u$ ,  $v$ ,  $w$  and  $\theta$  spectra as well as the  $uw$  and  $w\theta$  cospectra were placed in three stability categories: moderately unstable  $-1 < z/L < 0.0$ , moderately stable  $0.0 < z/L < +1.0$ , and very stable  $z/L > +1.0$ . The variance normalized logarithmic spectra and cospectra of the turbulence for all heights and all stability categories collapse into near universal curves when plotted against the modified frequency scale  $f/f_0$ . Here,  $f_0$  is the intercept of the spectrum in the inertial subrange with the line  $n S_\alpha(n)/\sigma_\alpha^2 = 1$  and is directly related to the peak reduced frequency,  $f_m^\alpha$ . In the stability range  $0 < z/L < +2.0$ , the peak reduced frequencies for all three velocities follow the Kansas results which were obtained in the surface layer above a field of wheat stubble.

For increased stability  $z/L > +2.0$ , the peak reduced frequencies do not follow the trend which was established in the moderate stability category. The values of  $f_m^\alpha$  show a great deal of scatter with stability but seem to have a lower magnitude than the largest value encountered

at  $z/L \approx +2.0$ . The peak reduced frequency,  $f_m^w$ , seems to become constant for higher stabilities which indicates that the peak wave length  $\lambda_m^w$  becomes proportional to  $z$  outside the IBL. This indicates that the maximum wave length,  $\lambda_m^w$  for very stable flow is proportional to height, thus in contrast to the results reported by Busch and Panofsky [2]. The peak reduced frequencies,  $f_m^w$ , which show a near constant value for the stability range  $z/L > +2.0$  were obtained from elevations above the IBL. At these heights the air has not been affected by the changes in surface roughness and surface temperature and are still governed by the conditions above the ocean.

Similar conclusions can be drawn from the spectral values evaluated at a fixed reduced frequency,  $f = 10$ . The parameter  $[n S_\alpha(n)/U_*^2]_{f=10}$  follows the Kansas data closely for  $z/L < +2.0$ . However for increased stability this trend is discontinued and the results show a great deal of scatter.

These results indicate that there does not seem to be a critical Richardson number above which the turbulence disappears. However, basic changes in the turbulence do occur when the stability parameter increases past  $z/L \approx +2.0$ . The turbulence levels decrease drastically and if, in addition, the large scale eddies disappear, it would not take very long for the small scale eddies to dissipate if no large eddies are present to draw energy from.

At the present it is not clear what specific conditions need to be satisfied for all turbulence to disappear. At one point in time when the data-acquisition system was on-line (no data were recorded

during this time), this condition was observed at the 200 and 250 foot level. It is difficult to accept absolute no-turbulence in the air which is moving along with a mean speed of approximately 20 fps.

## REFERENCES

1. Busch, N. E., "The Surface Boundary Layer", Boundary Layer Meteorology, Vol. 4, pp. 213-240, April 1973.
2. Busch, N. E. and H. A. Panofsky, "Recent Spectra of Atmospheric Turbulence", Quarterly Journal of the Royal Meteorological Society, Vol. 94, pp. 132-148, April 1968.
3. Corrsin, S., "On the Spectrum of Isotropic Temperature Fluctuations in an Isotropic Turbulence", Journal of Applied Physics, Vol. 22, pp. 469-473, 1951.
4. Dyer, A. J., "A Review of Flux-Profile Relationships", Boundary Layer Meteorology, Vol. 7, pp. 363-372, 1974.
5. Busch, N. E., "On the Mechanics of Atmospheric Turbulence", Workshop on Micrometeorology, American Meteorological Society, Boston, Mass., pp. 1-65.
6. Kaimal, J. C., "Turbulence Spectra, Length Scales and Structure Parameters in the Stable Surface Layer", Boundary Layer Meteorology, Vol. 4, pp. 289-309, April 1973.
7. Kaimal, J. C., J. C. Wyngaard, Y. Izumi, and O. R. Coté, "Spectral Characteristics of Surface Layer Turbulence", Quarterly Journal of the Royal Meteorological Society, Vol. 98, pp. 563-589, 1972.
8. Monin, A. S. and A. M. Yaglom, Statistical Fluid Mechanics, The MIT Press, Cambridge, Mass., 1971.
9. Obukhov, A. M., "Turbulence in an Atmosphere with a Non-Uniform Temperature", (Originally appeared in Works of the Institute of Theoretical Geophysics, Academy of Science, USSR, No. 1, 1943), Boundary Layer Meteorology, Vol. 2, 1971.
10. Panofsky, H. A., "Spectra of Atmospheric Variables in the Boundary Layer", Radio Science, Vol. 4, No. 12, pp. 1101-1109, December 1969.
11. Tieleman, H. W. and W. W. L. Chen, "Statistical Analysis of Low Level Atmospheric Turbulence", NASA-CR-137456, 1974.
12. Tieleman, H. W. and S. C. Tavoularis, "A Method for the Measurement and the Statistical Analysis of Atmospheric Turbulence", NASA-CR-140586, 1974.

13. Wyngaard, J. C. and O. R. Coté, "The Budgets of Turbulent Kinetic Energy and Temperature Variance in the Atmospheric Surface Layer", Journal of the Atmospheric Sciences, Vol. 28, pp. 190-200, 1970.

## FIGURES



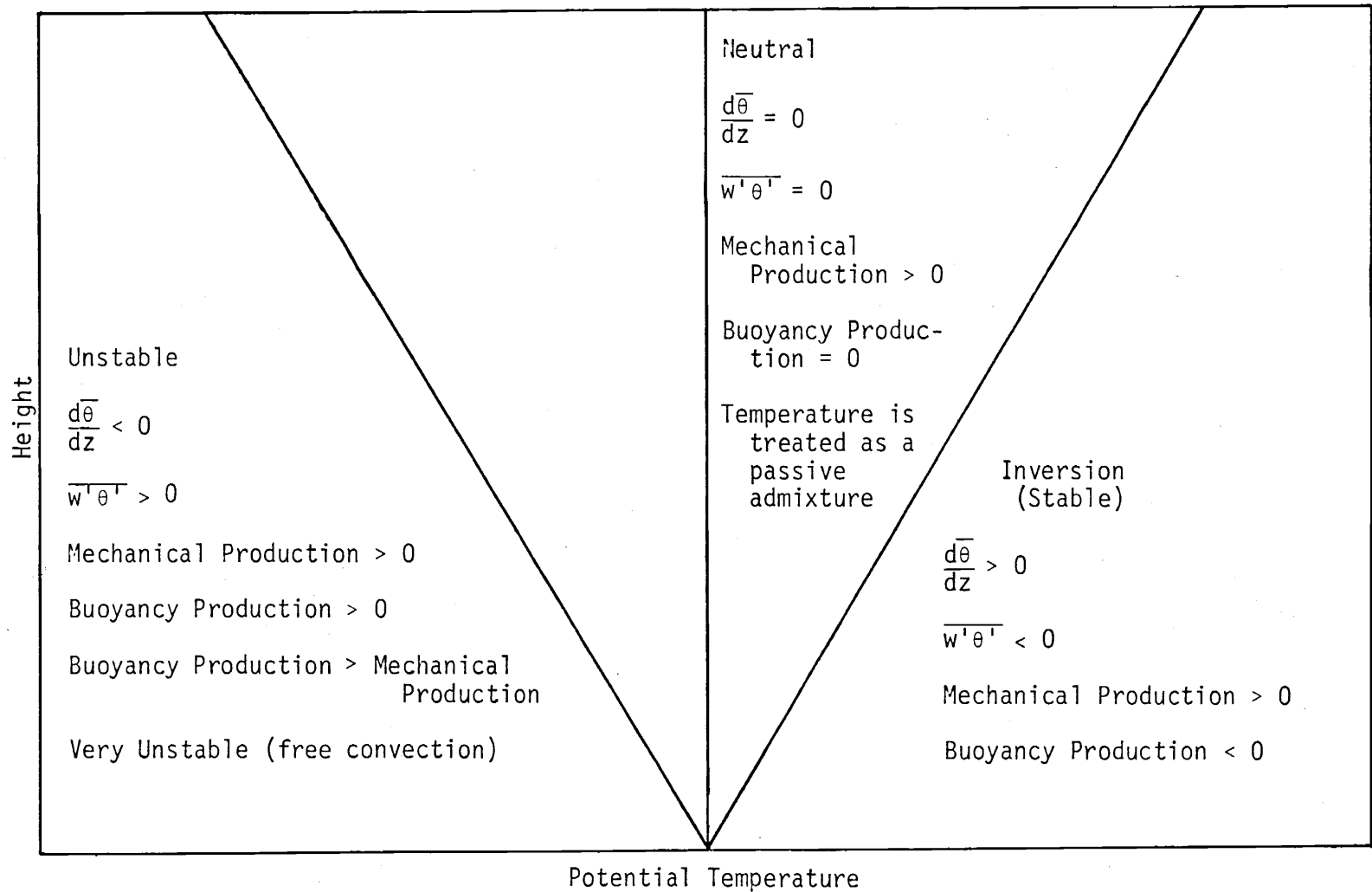


Figure 1. Potential temperature profiles for stable, neutral and unstable thermal stratification.

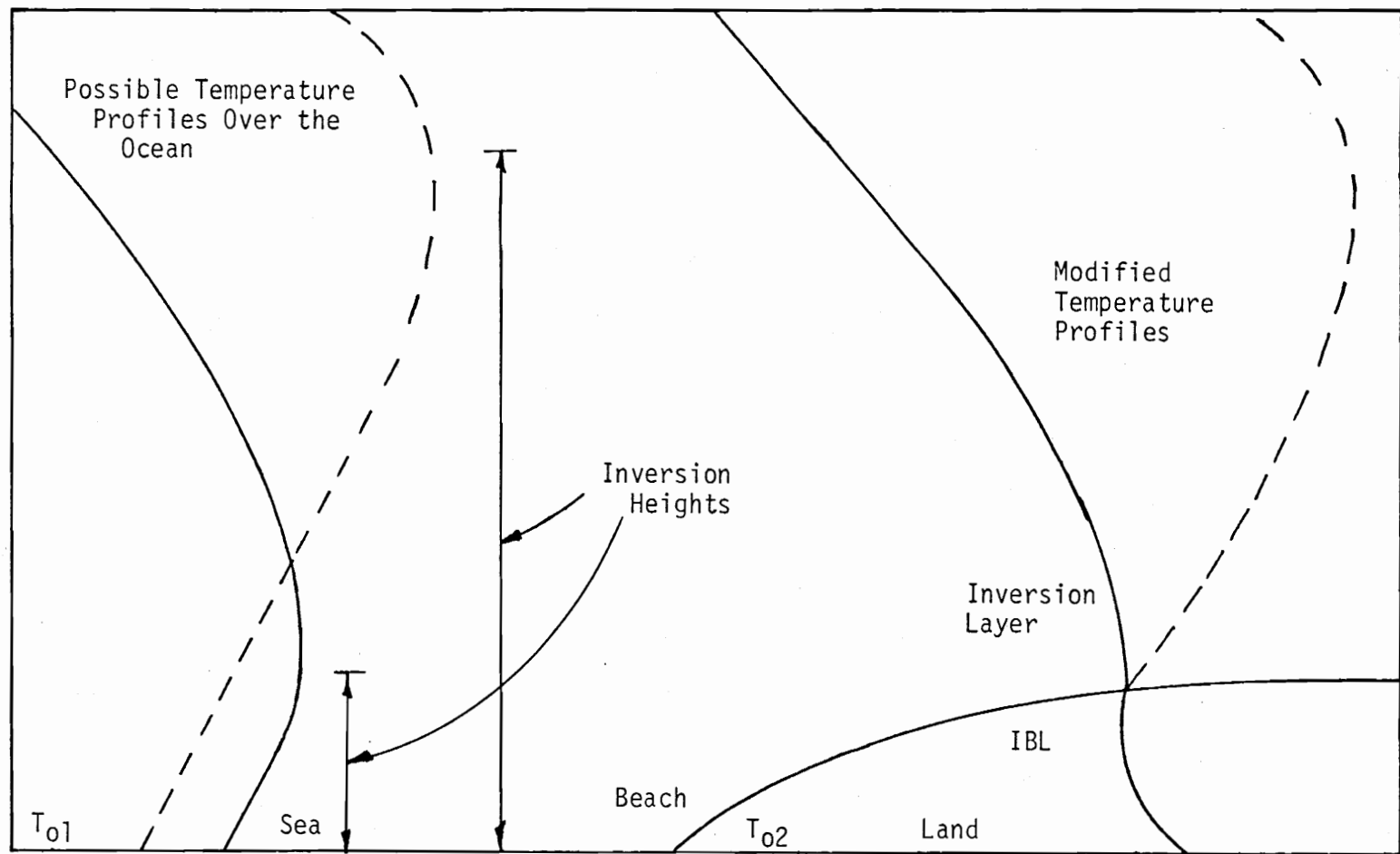


Figure 2. Model for the temperature profiles for on-shore flow and the internal boundary layer (IBL).

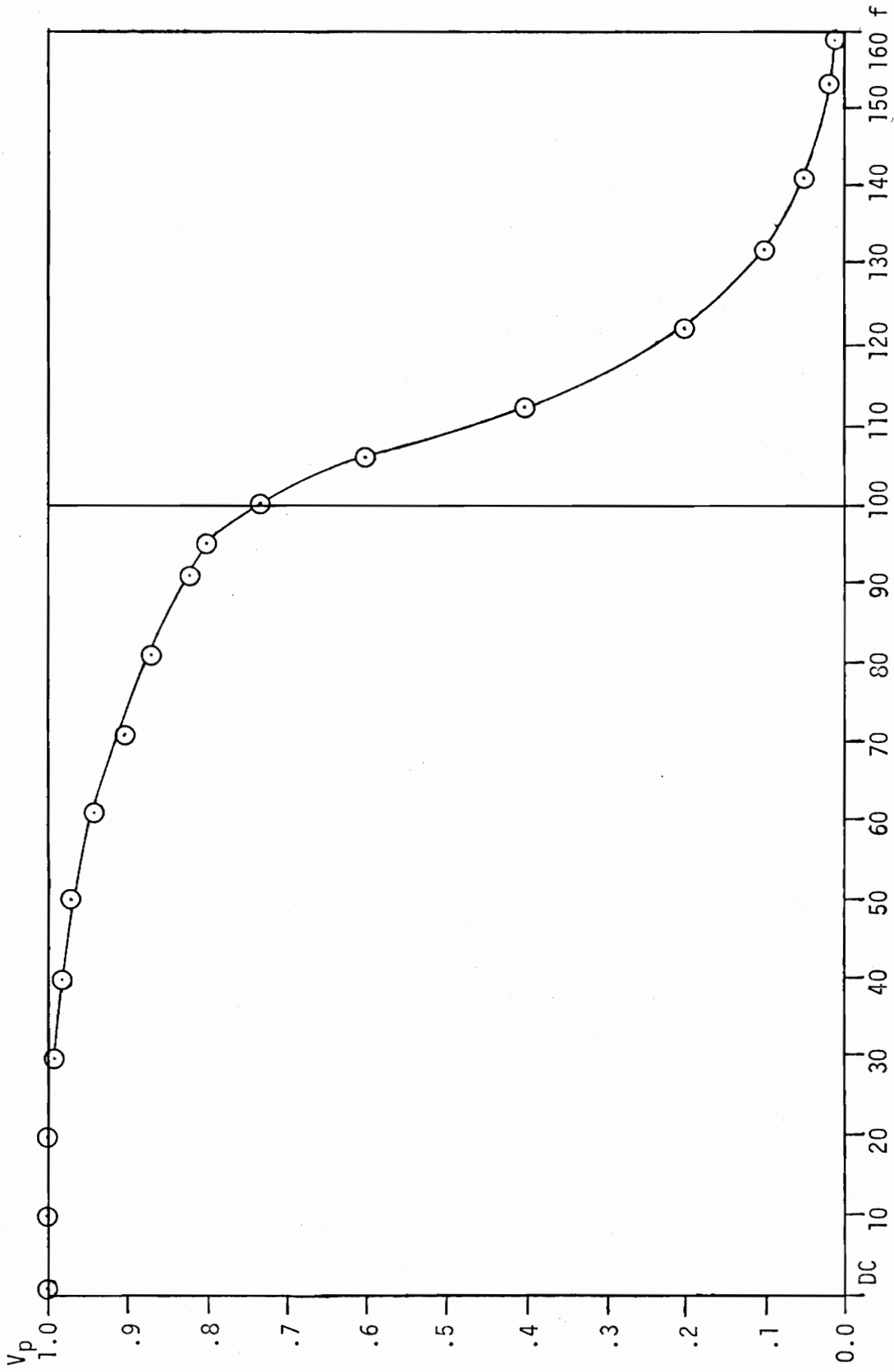


Figure 3. 100 Hz low-pass filter.

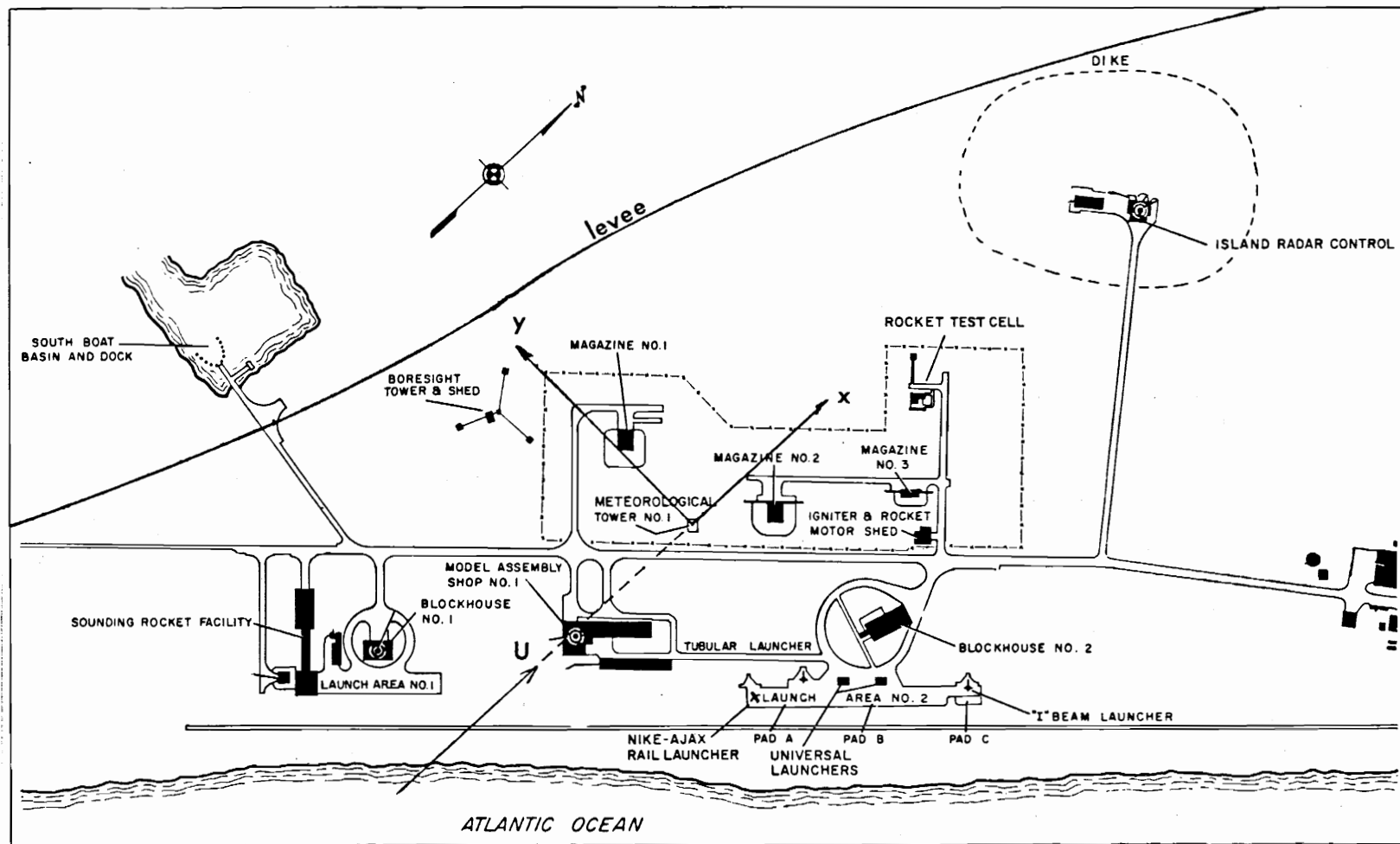


Figure 4. Tower location on Wallops Island and orientation of a general coordinate system.

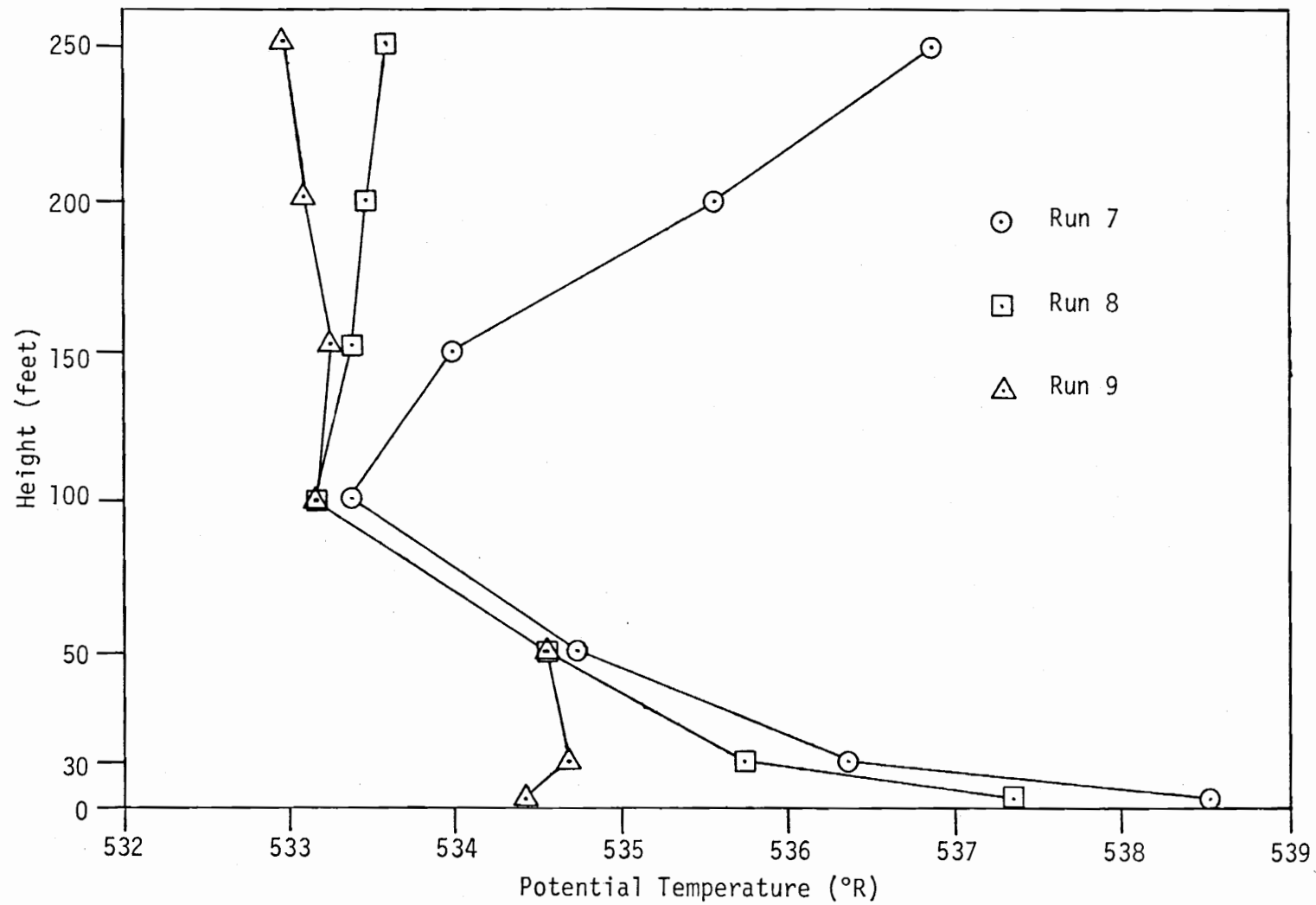


Figure 5. Vertical temperature distributions for runs 7, 8 and 9.

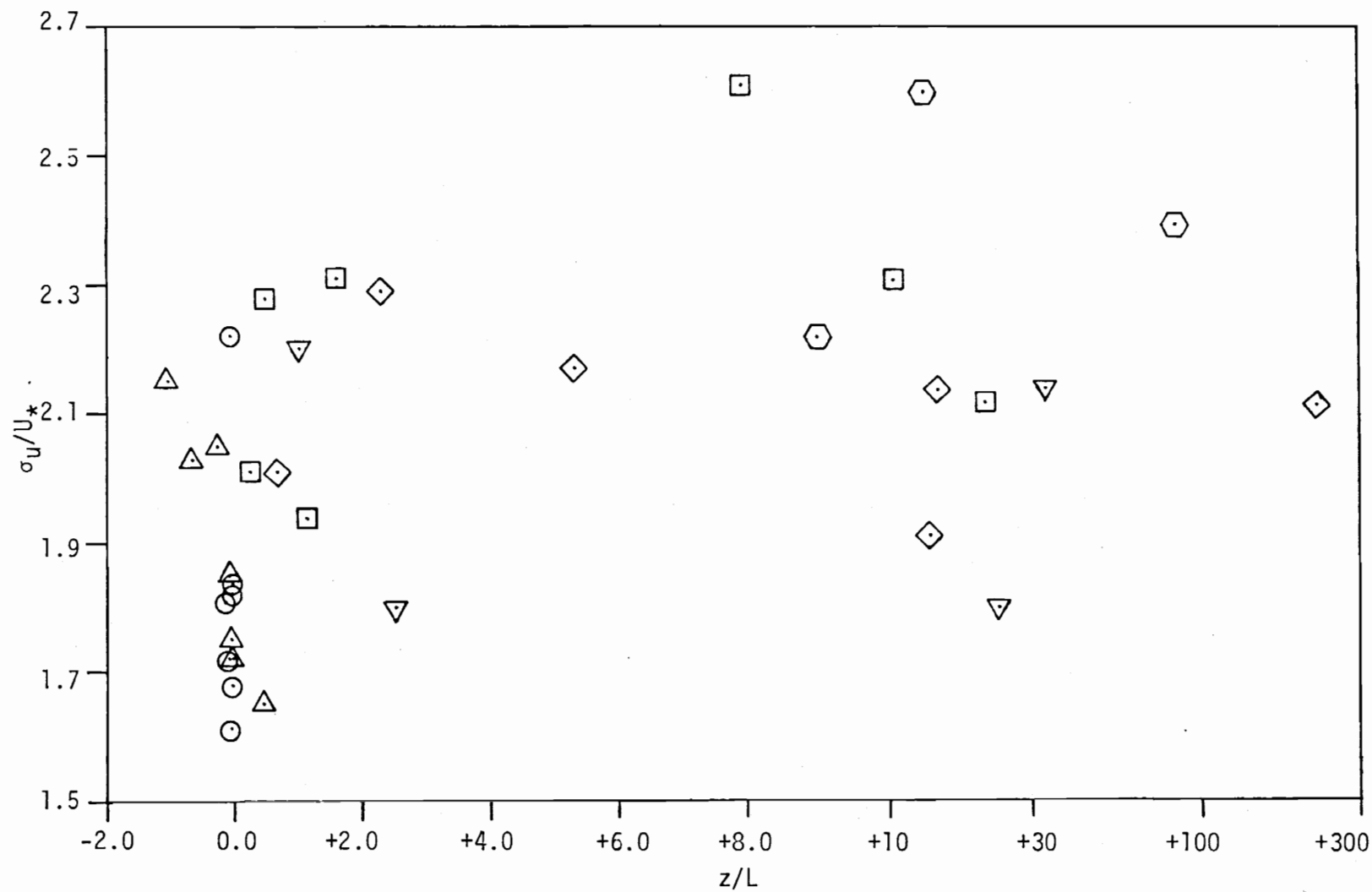


Figure 6. Ratio of standard deviation of longitudinal velocity to local friction velocity as a function of  $z/L$ .

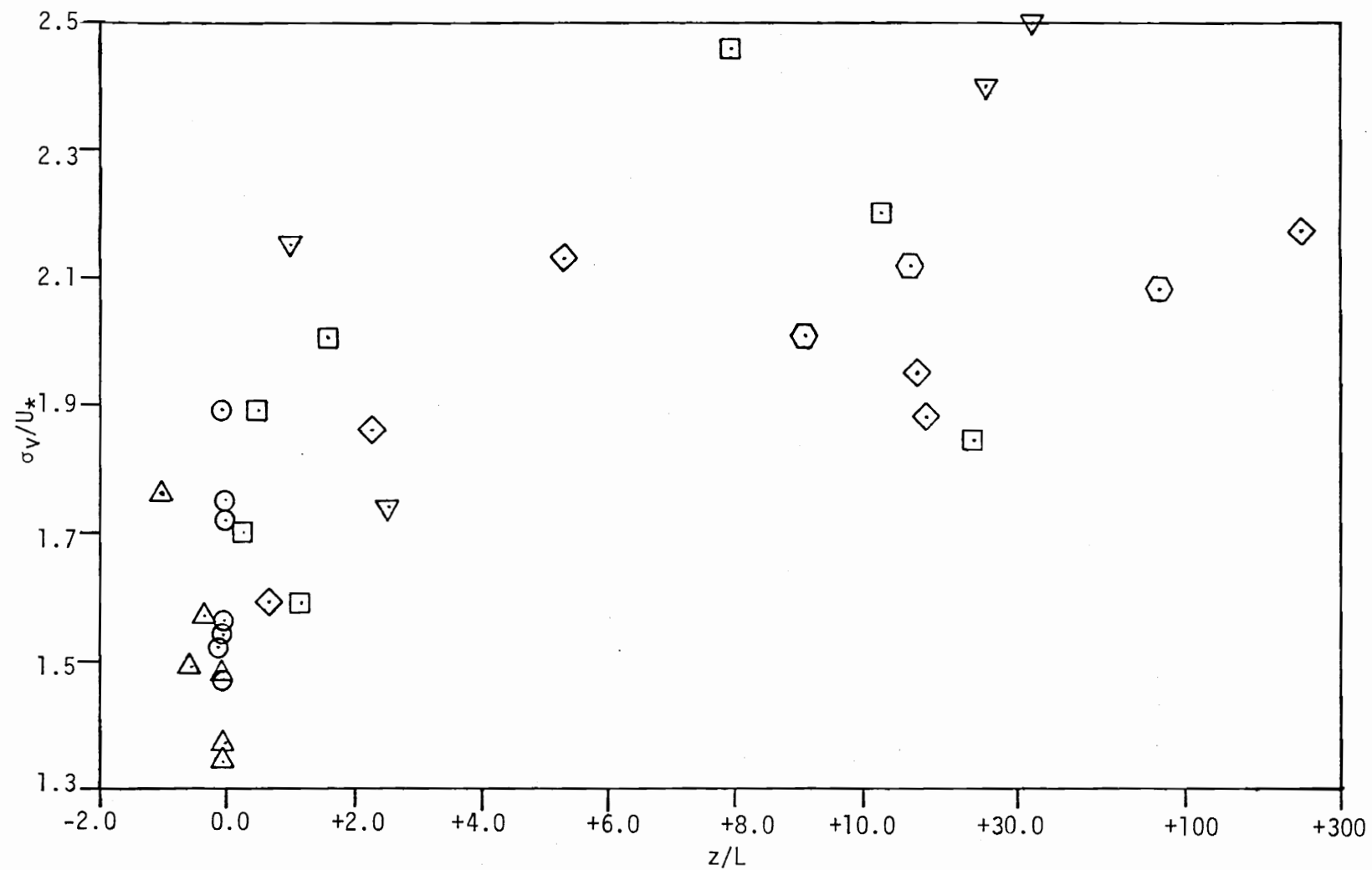


Figure 7. Ratio of standard deviation of lateral velocity to local friction velocity as a function of  $z/L$ .

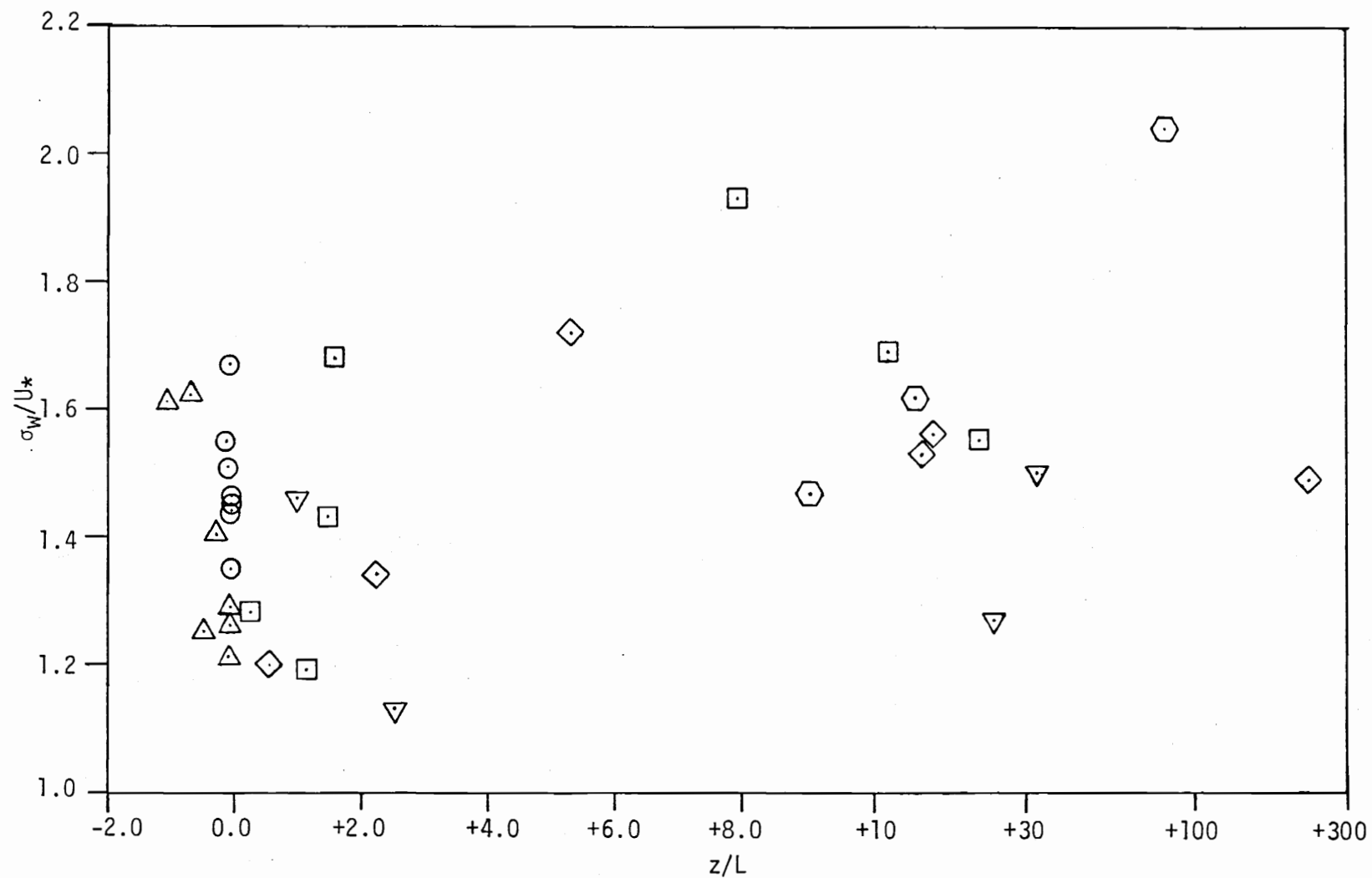


Figure 8. Ratio of standard deviation of vertical velocity to local friction velocity as a function of  $z/L$ .



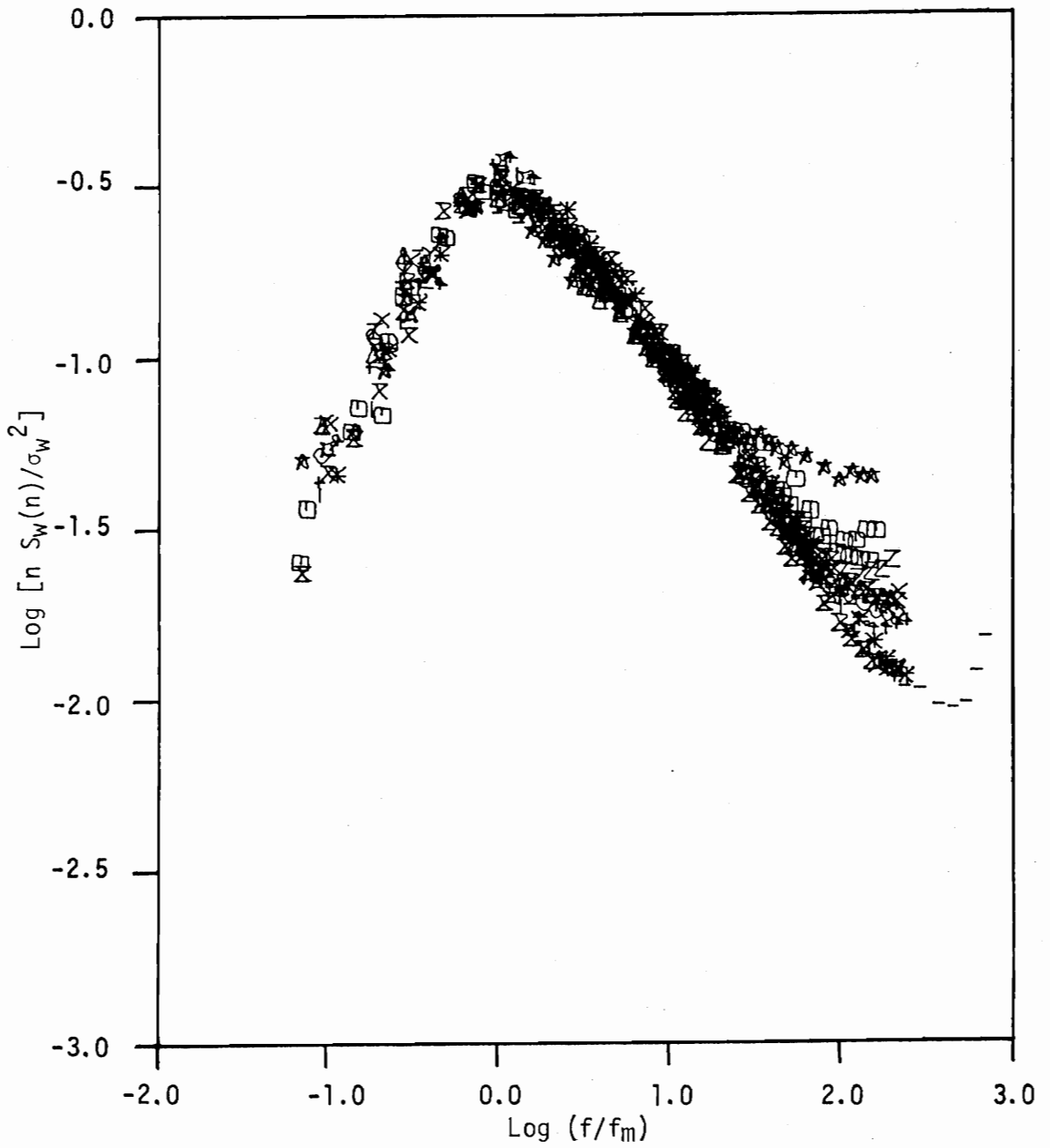


Figure 9a. Logarithmic spectra of the vertical velocity normalized by the variance versus  $f/f_m$ , moderately unstable,  $-1.0 < z/L < 0$ .

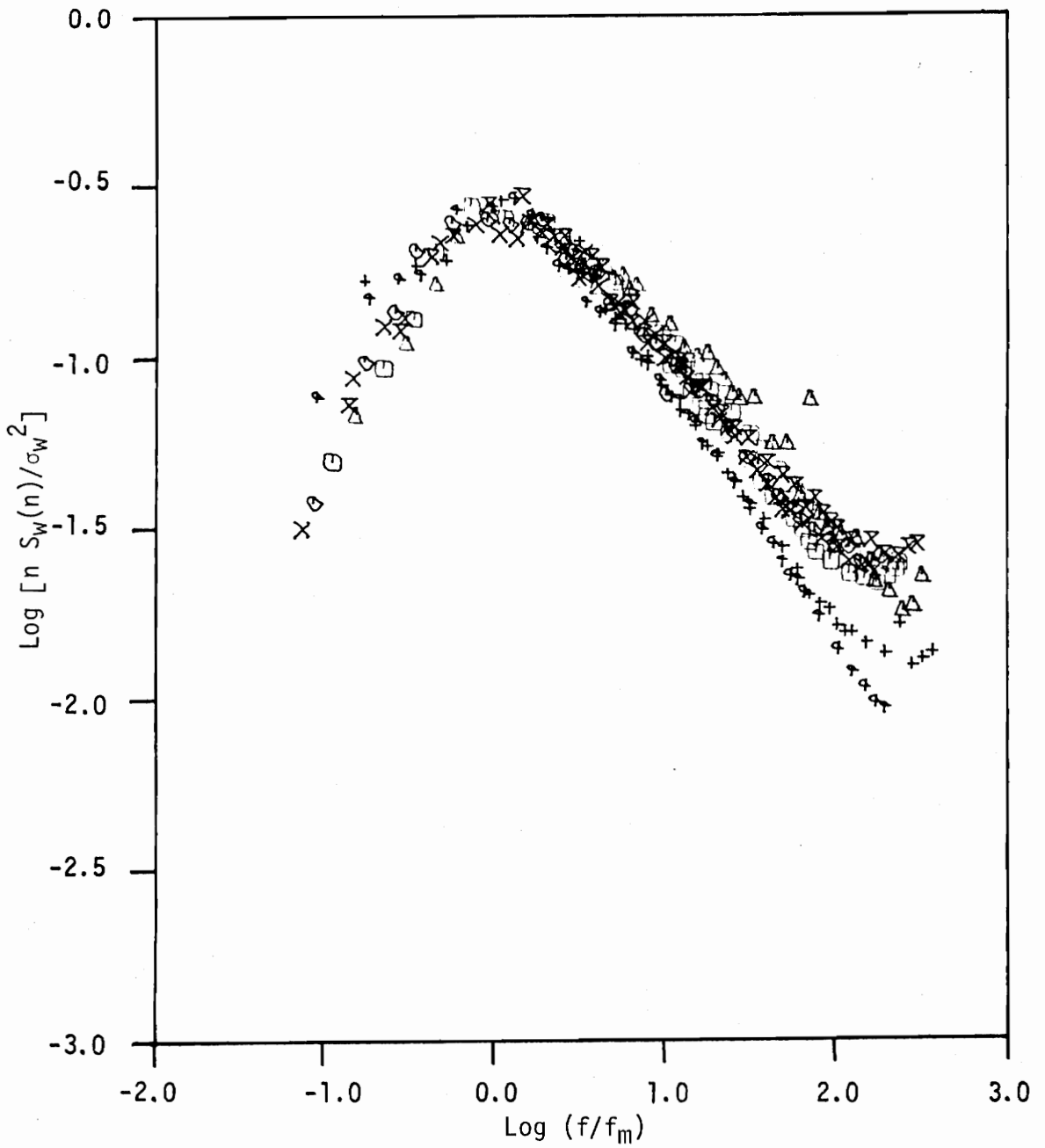


Figure 9b. Logarithmic spectra of the vertical velocity normalized by the variance versus  $f/f_m$ , moderately stable,  $0 < z/L < +1.0$ .

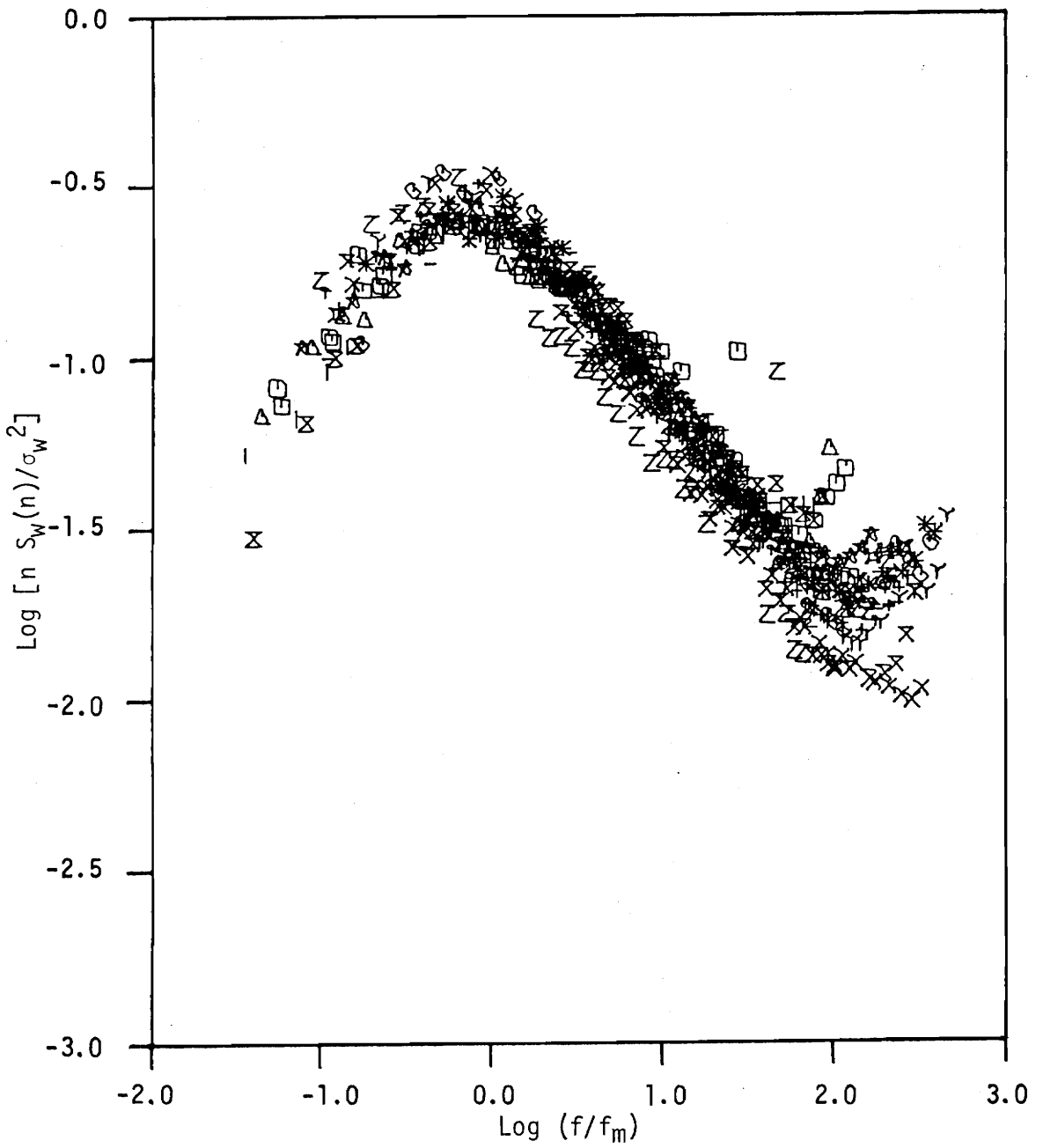


Figure 9c. Logarithmic spectra of the vertical velocity normalized by the variance versus  $f/f_m$ , very stable  $z/L > +1.0$ .

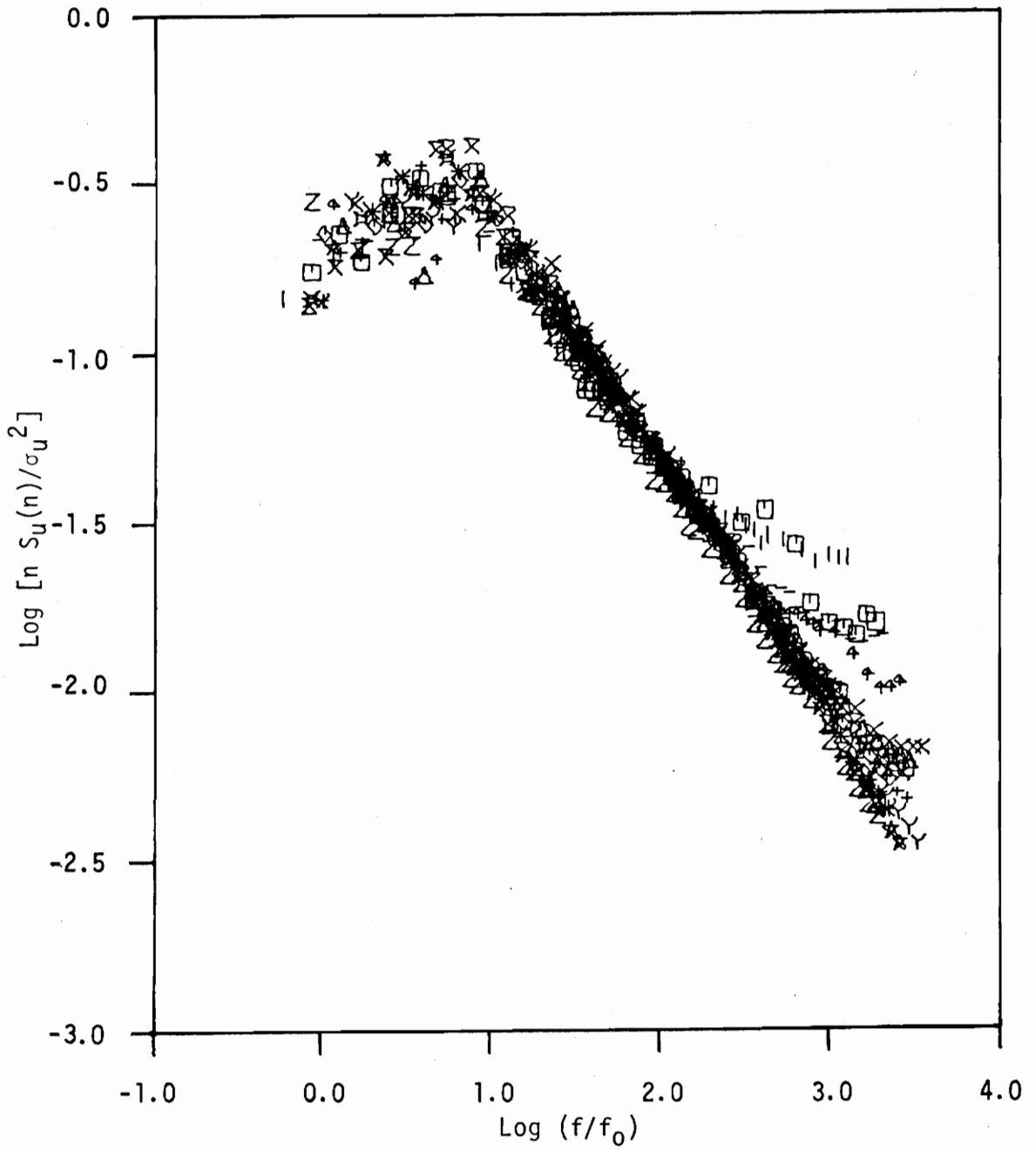


Figure 10a. Logarithmic spectra of the longitudinal velocity normalized by the variance versus  $f/f_0$ , moderately unstable,  $-1.0 < z/L < 0$ .

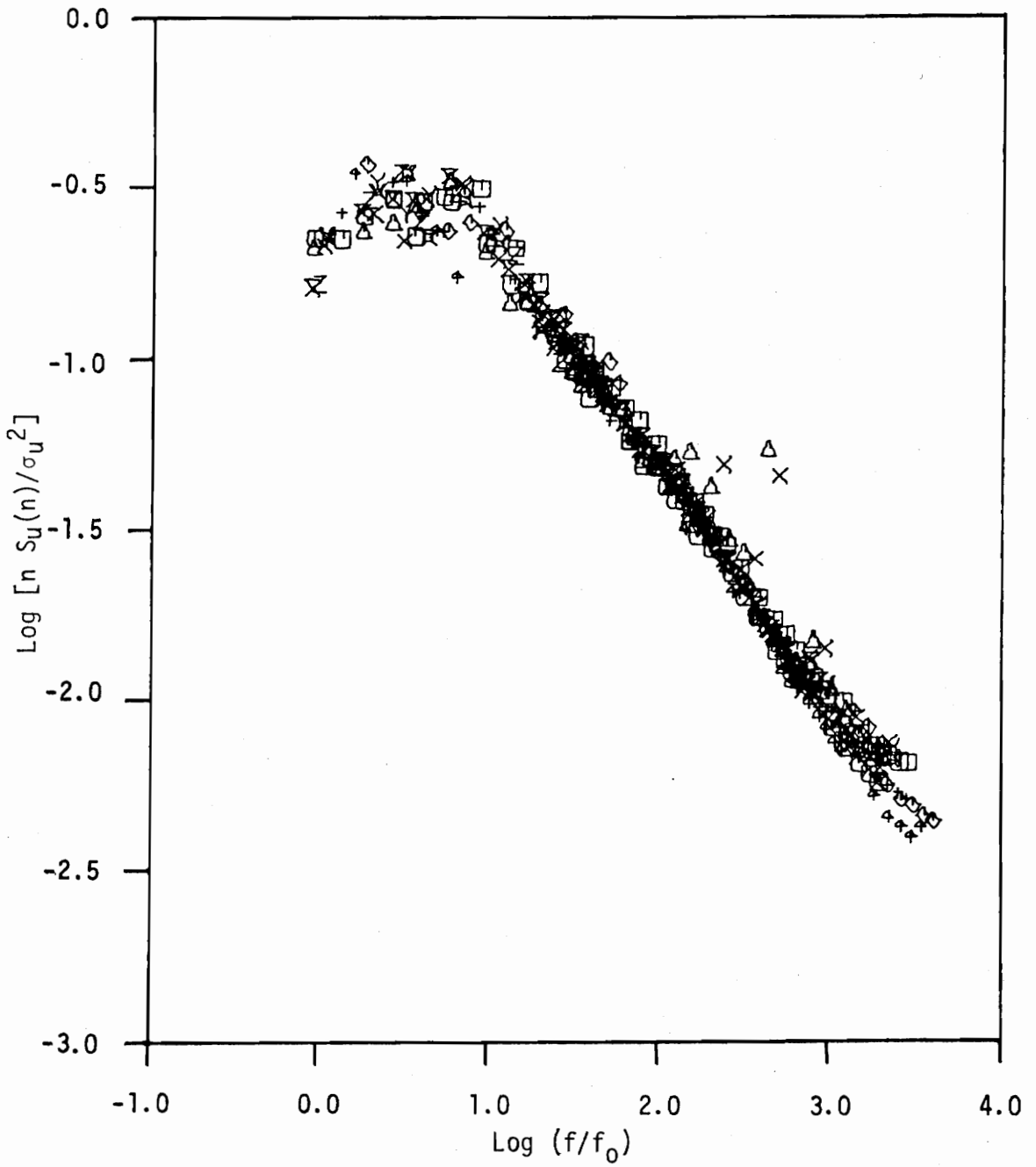


Figure 10b. Logarithmic spectra of the longitudinal velocity normalized by the variance versus  $f/f_0$ , moderately stable,  $0 < z/L < +1.0$ .

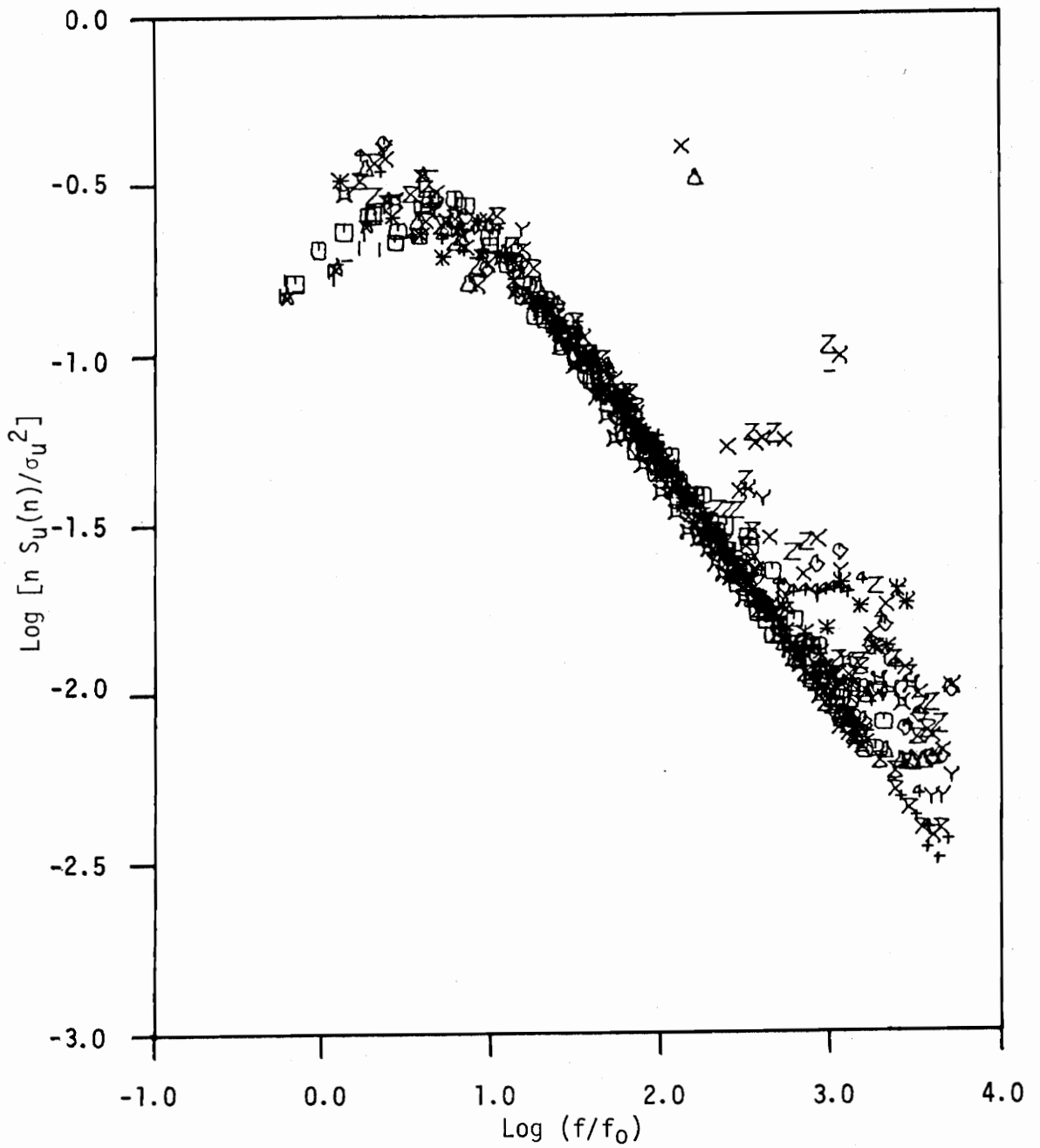


Figure 10c. Logarithmic spectra of the longitudinal velocity normalized by the variance versus  $f/f_0$ , very stable,  $z/L > +1.0$

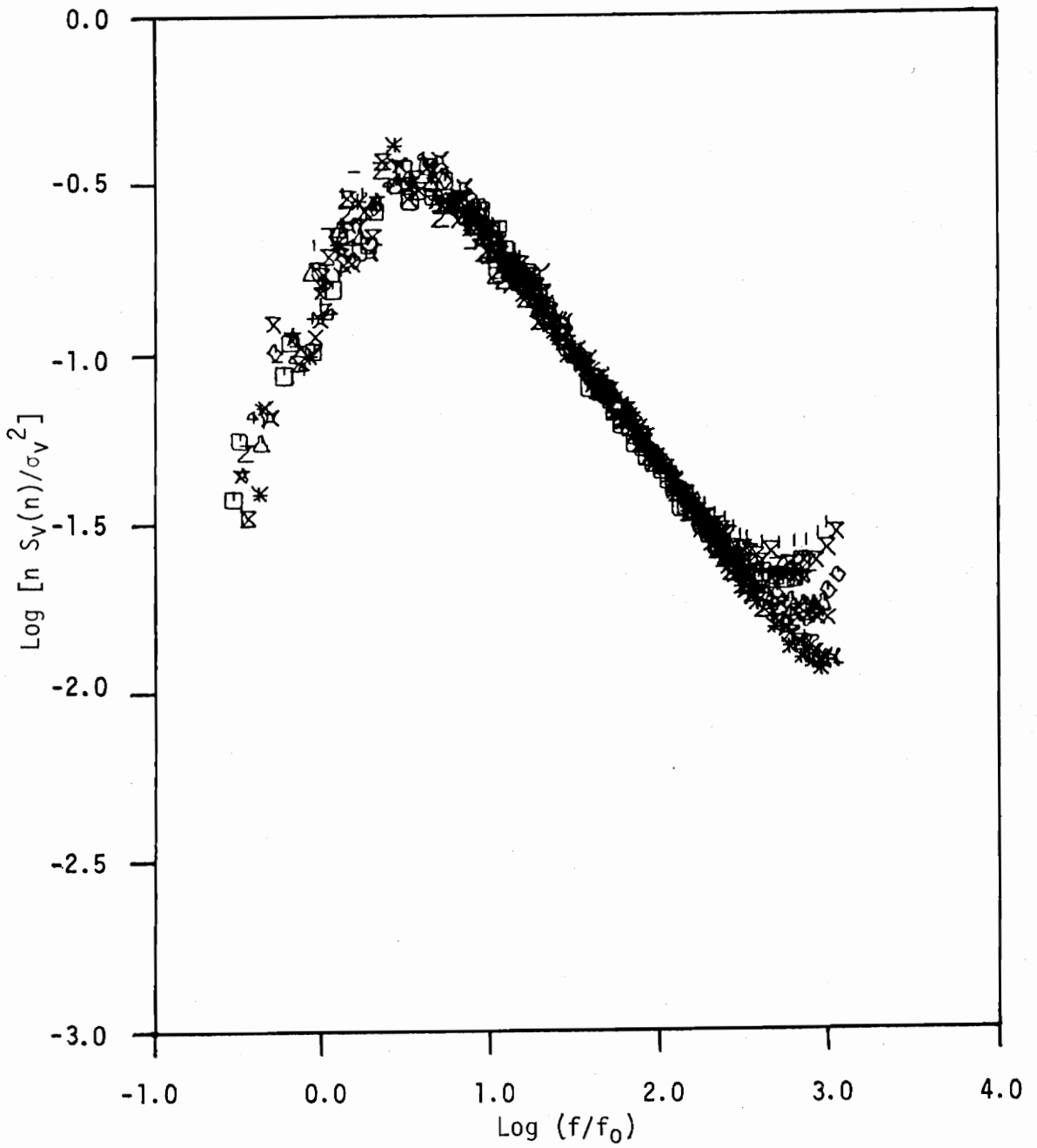


Figure 11a. Logarithmic spectra of the lateral velocity normalized by the variance versus  $f/f_0$ , moderately unstable,  $-1.0 < z/L < 0$ .

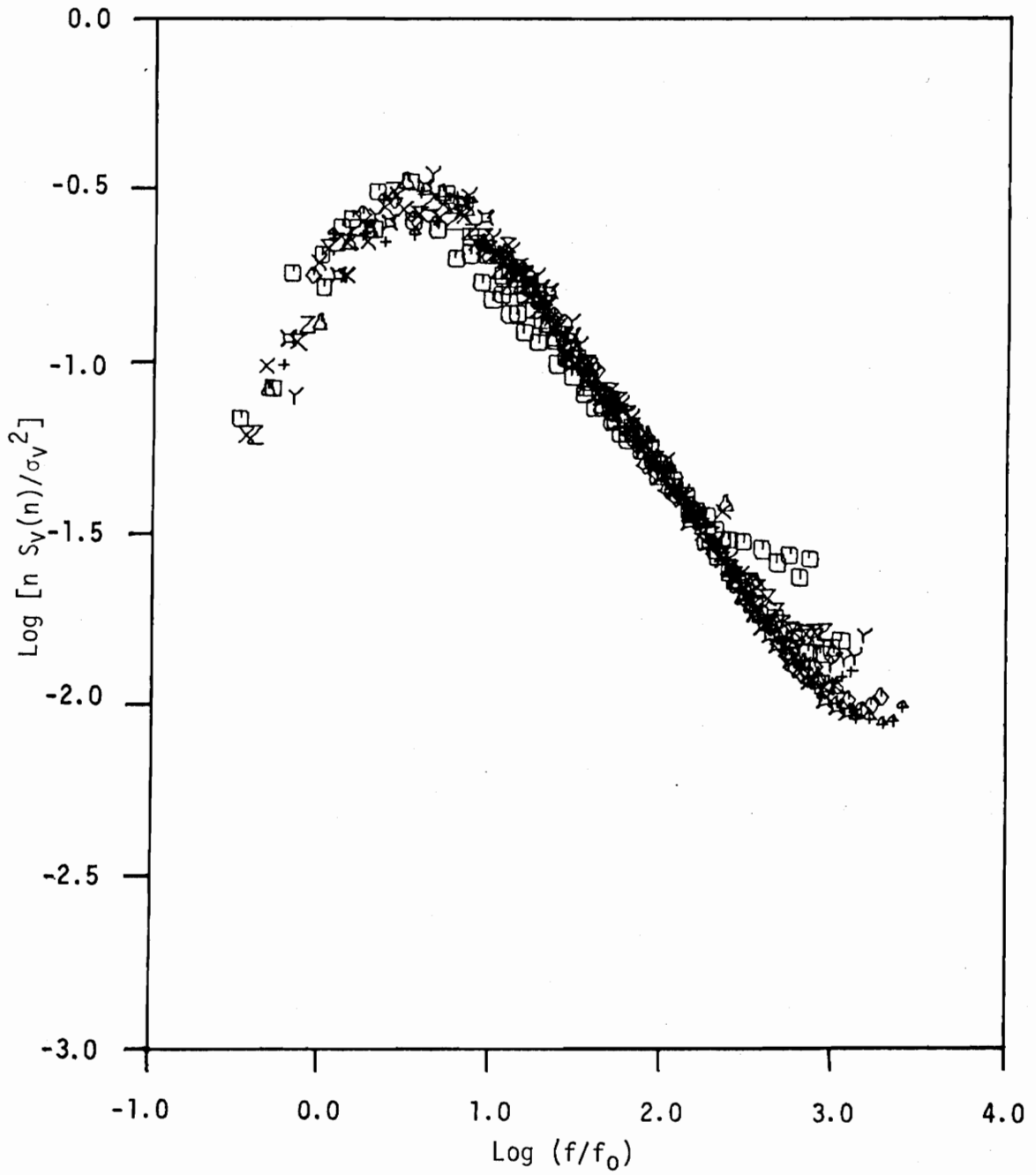


Figure 11b. Logarithmic spectra of the lateral velocity normalized by the variance versus  $f/f_0$ , moderately stable,  $0 < z/L < +1.0$ .



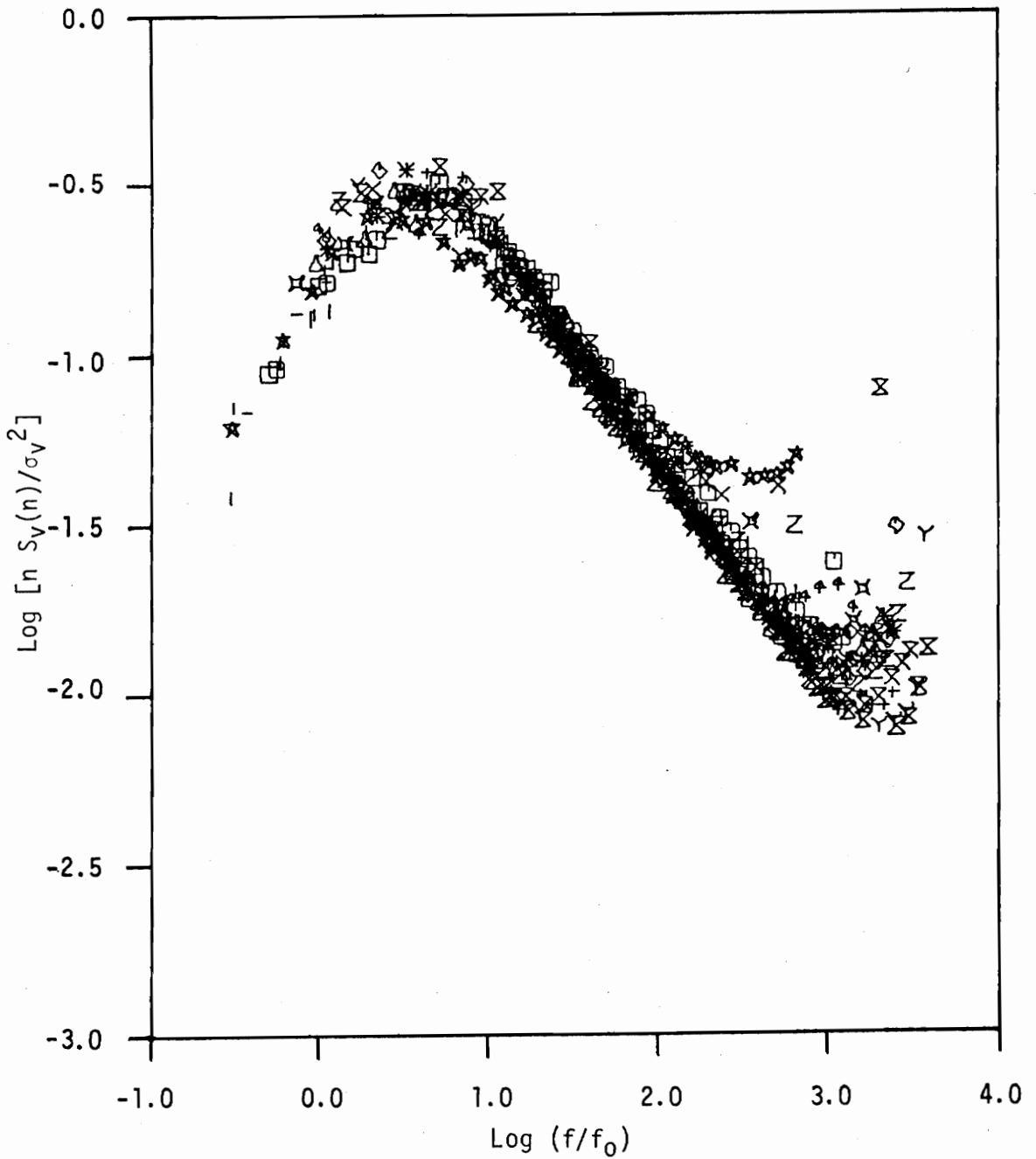


Figure 11c. Logarithmic spectra of the lateral velocity normalized by the variance versus  $f/f_0$ , very stable,  $z/L > +1.0$ .

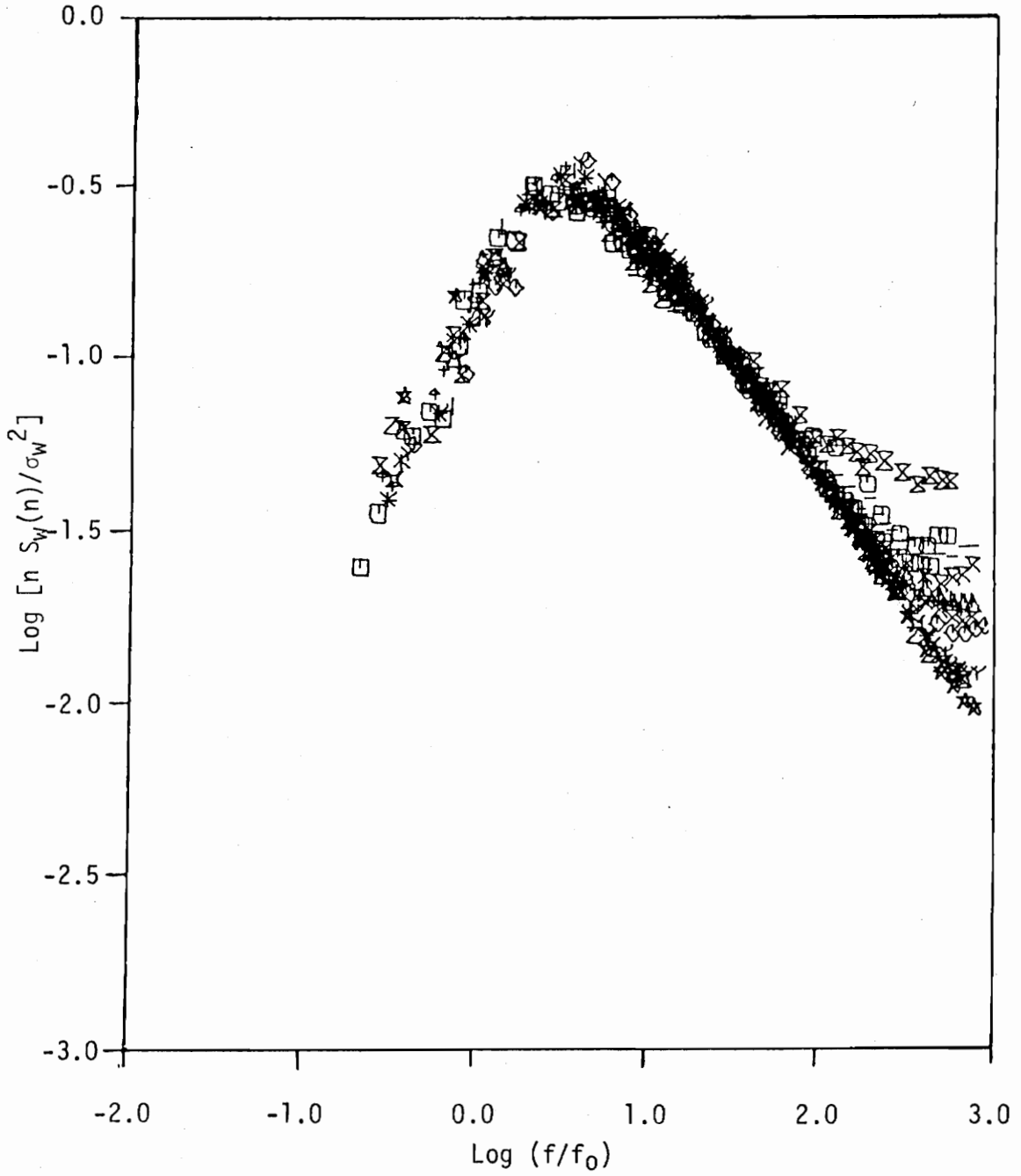


Figure 12a. Logarithmic spectra of the vertical velocity normalized by the variance versus  $f/f_0$ , moderately unstable,  $-1.0 < z/L < 0$ .

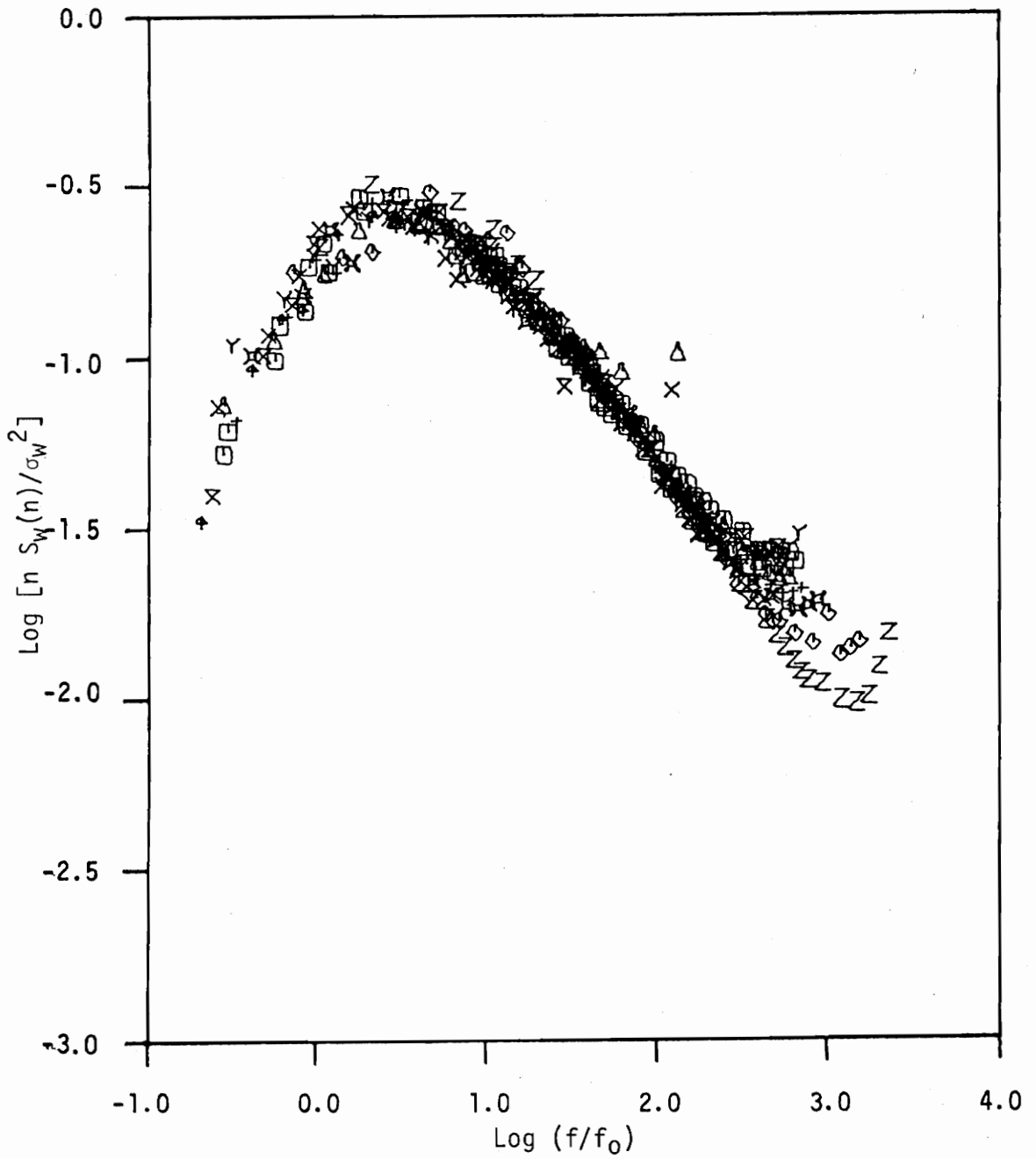


Figure 12b. Logarithmic spectra of the vertical velocity normalized by the variance versus  $f/f_0$ , moderately stable,  $0 < z/L < +1.0$ .

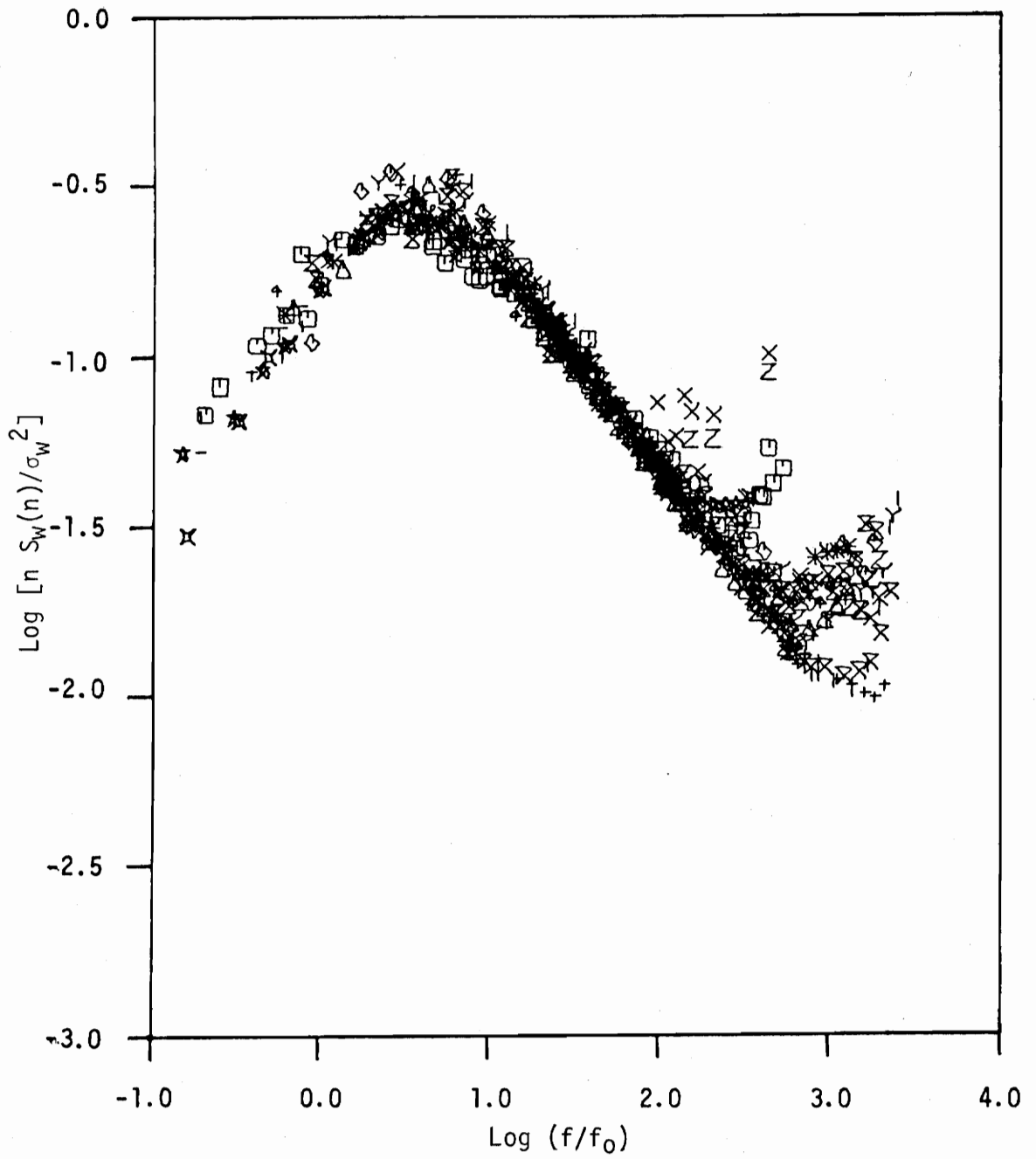


Figure 12c. Logarithmic spectra of the vertical velocity normalized by the variance versus  $f/f_0$ , very stable,  $z/L > +1.0$ .

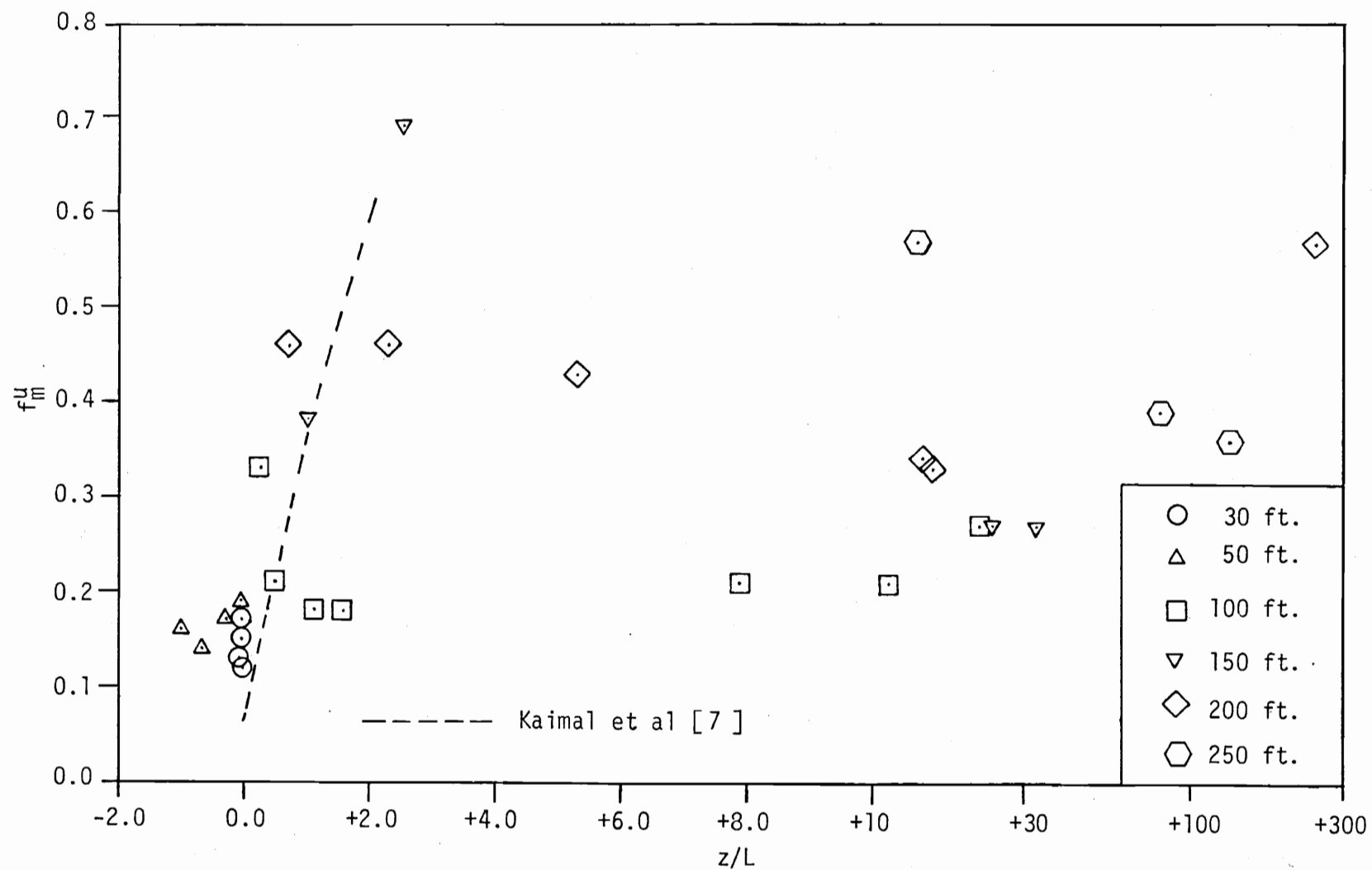


Figure 13. Variation of reduced peak-frequencies  $f_m^u$  for longitudinal velocity spectra with  $z/L$ .

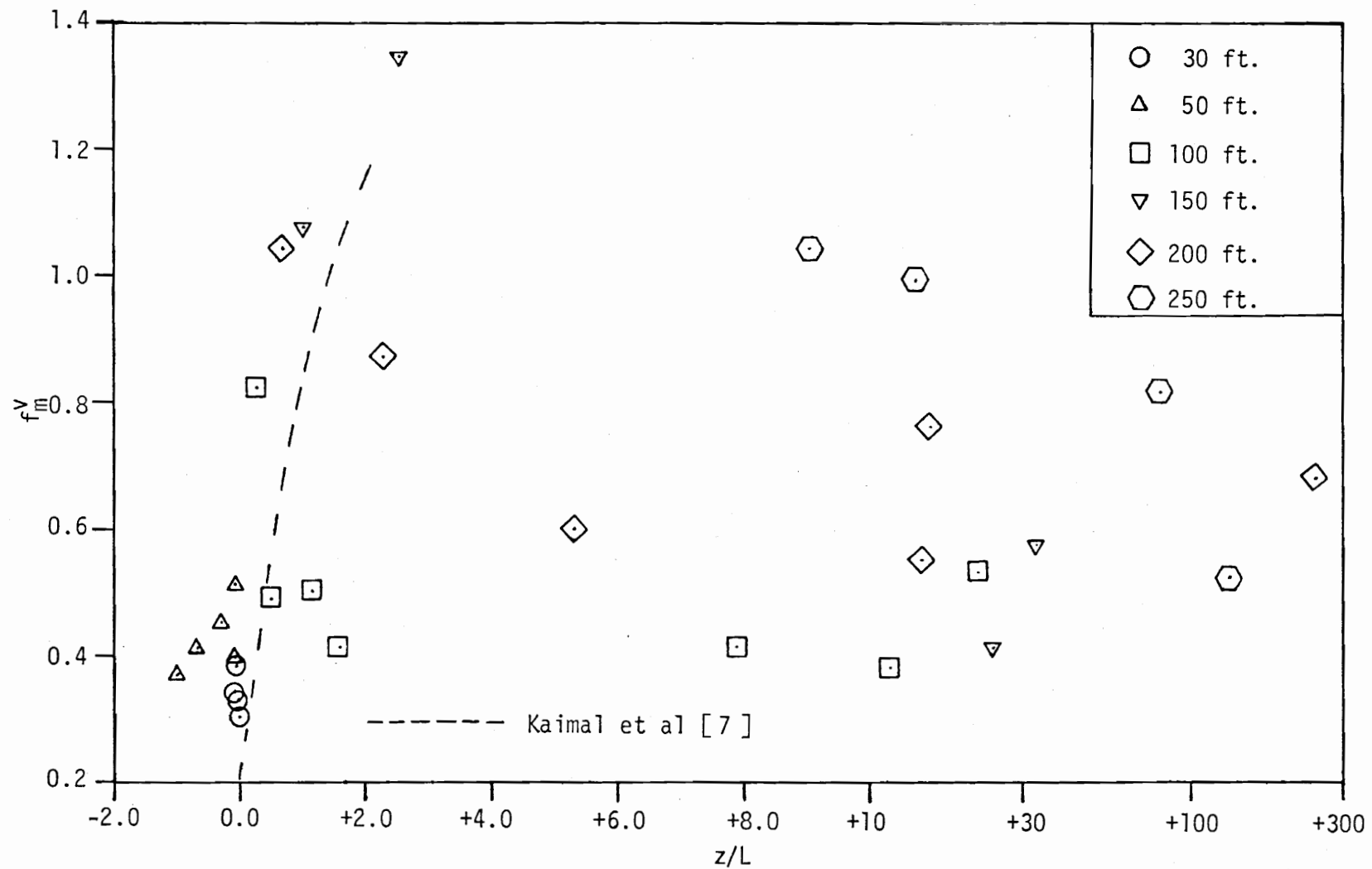


Figure 14. Variation of reduced peak-frequencies  $f_m^V$  for lateral velocity spectra with  $z/L$ .

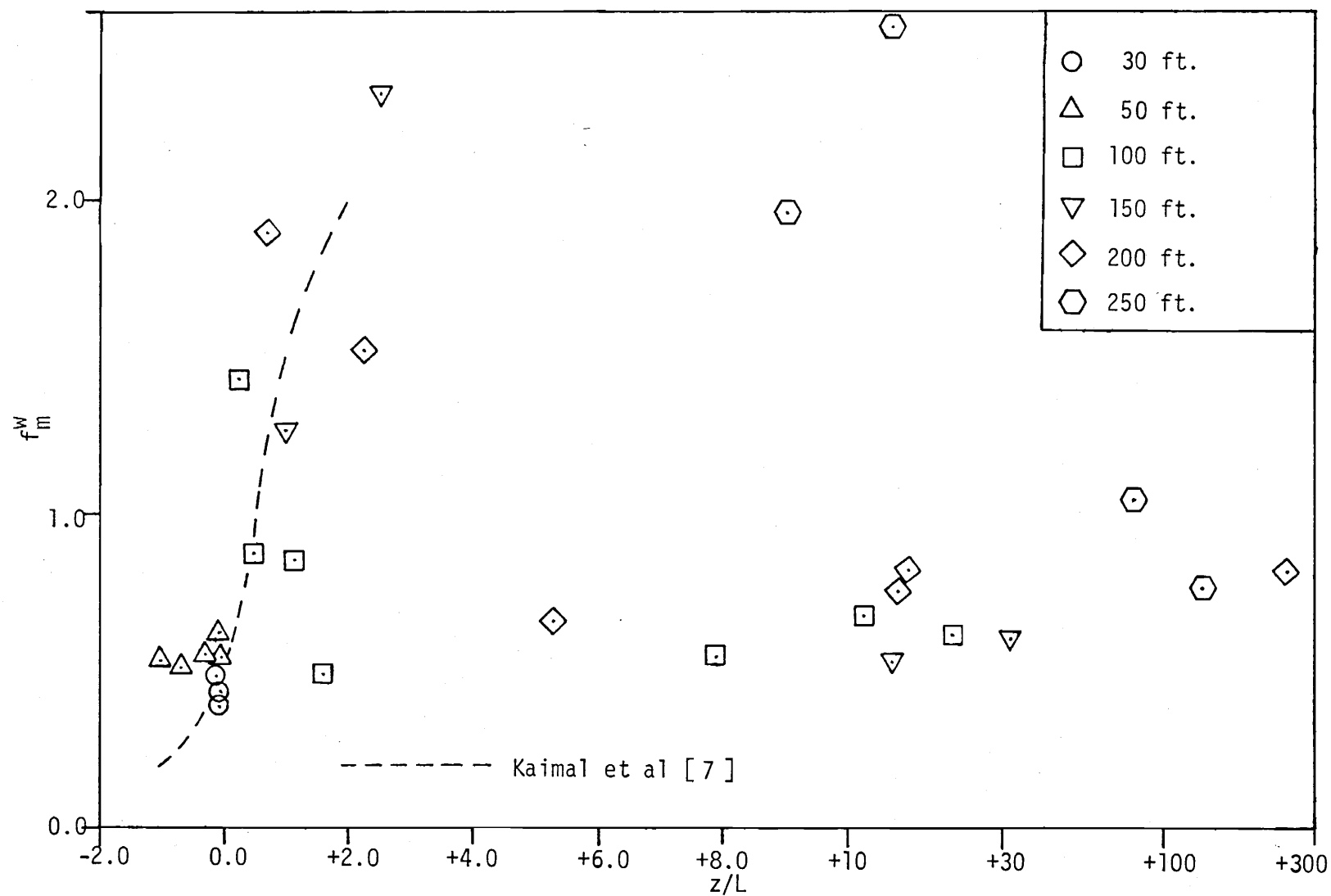


Figure 15. Variation of reduced peak-frequencies  $f_m^w$  for vertical velocity spectra with  $z/L$ .

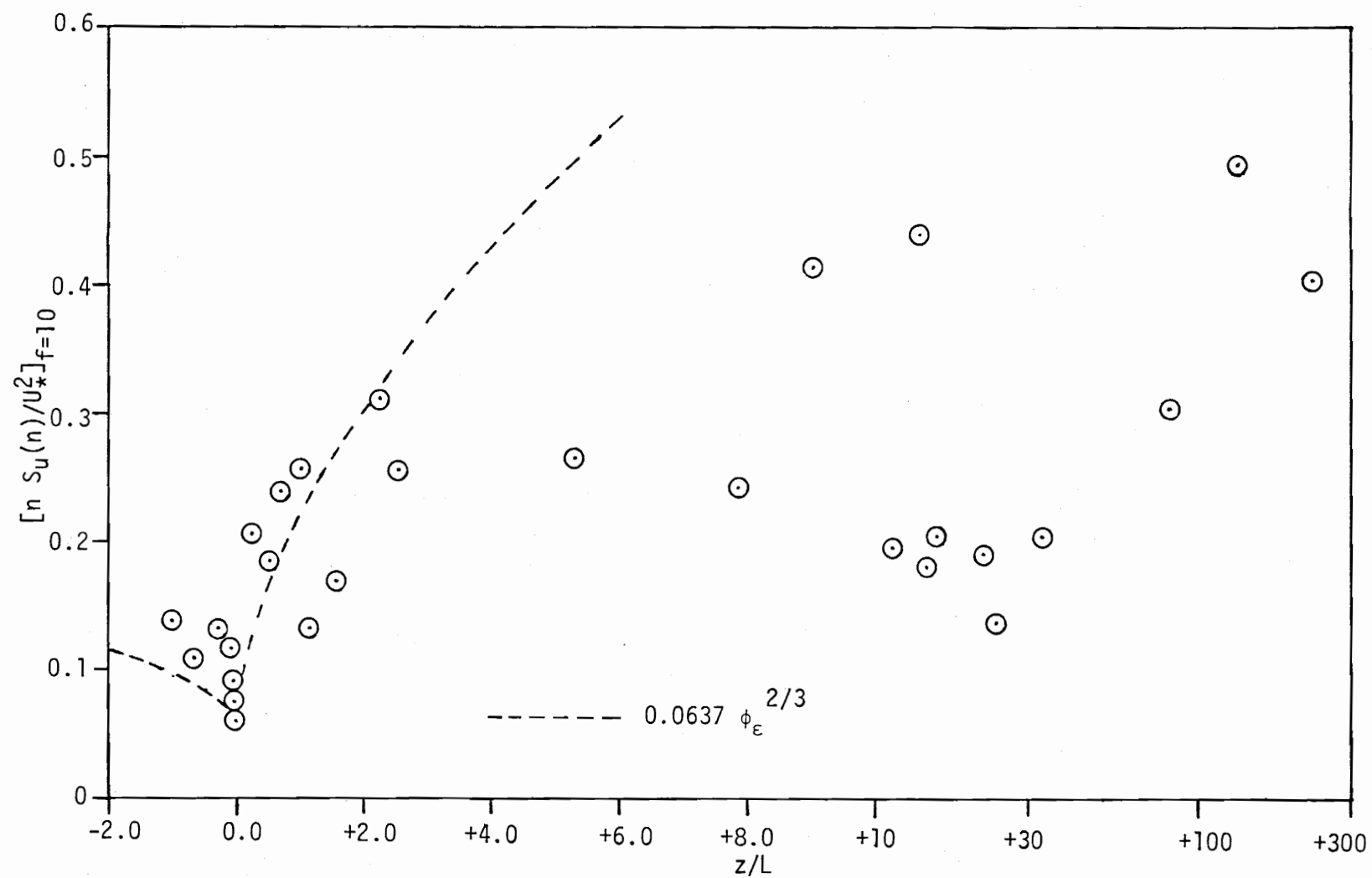


Figure 16. Estimates of the logarithmic spectra of the longitudinal velocity normalized by the local shear velocity at  $f=10$  versus stability.



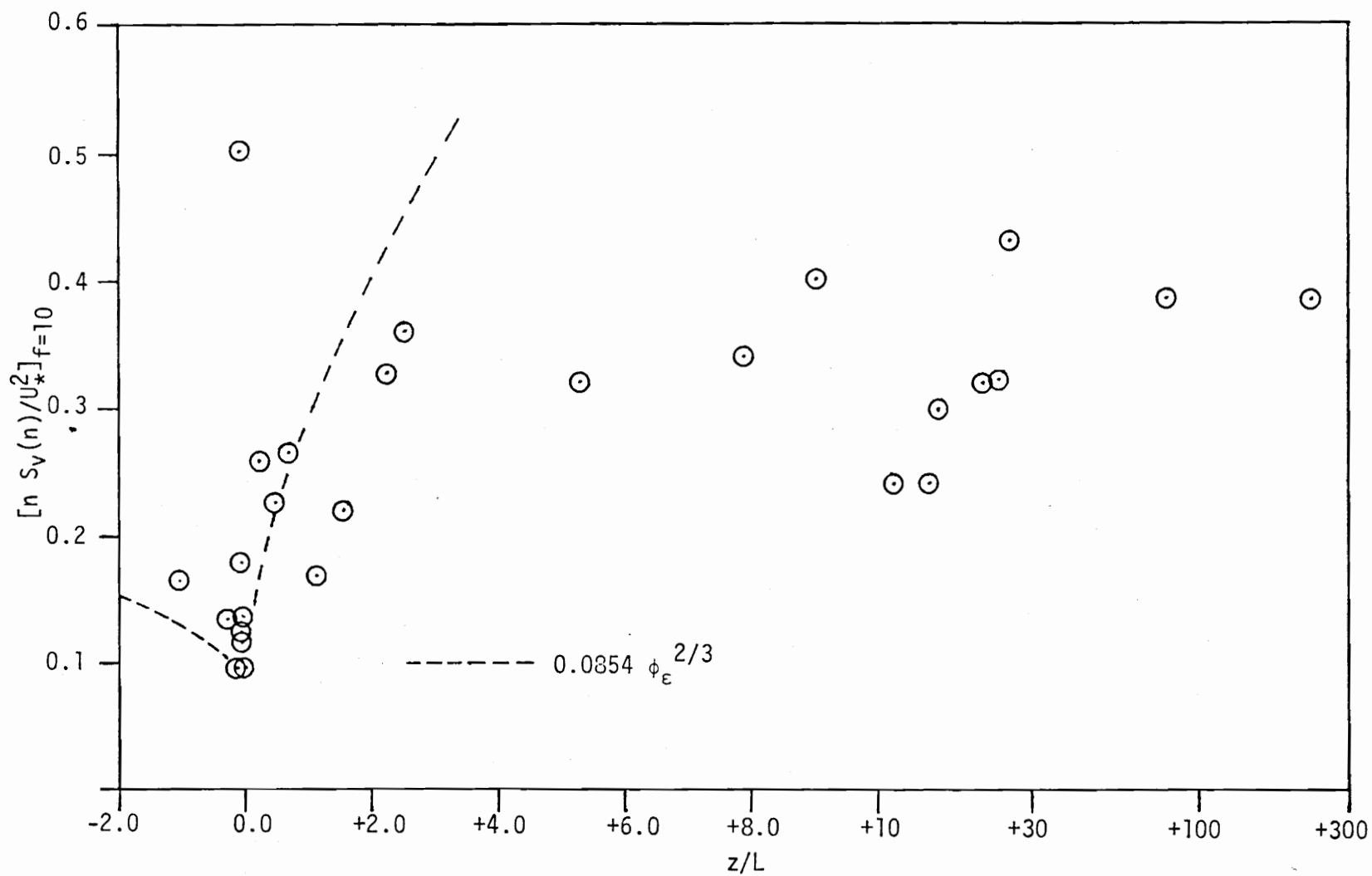


Figure 17. Estimates of the logarithmic spectra of the lateral velocity normalized by the local shear velocity at  $f=10$  versus stability.

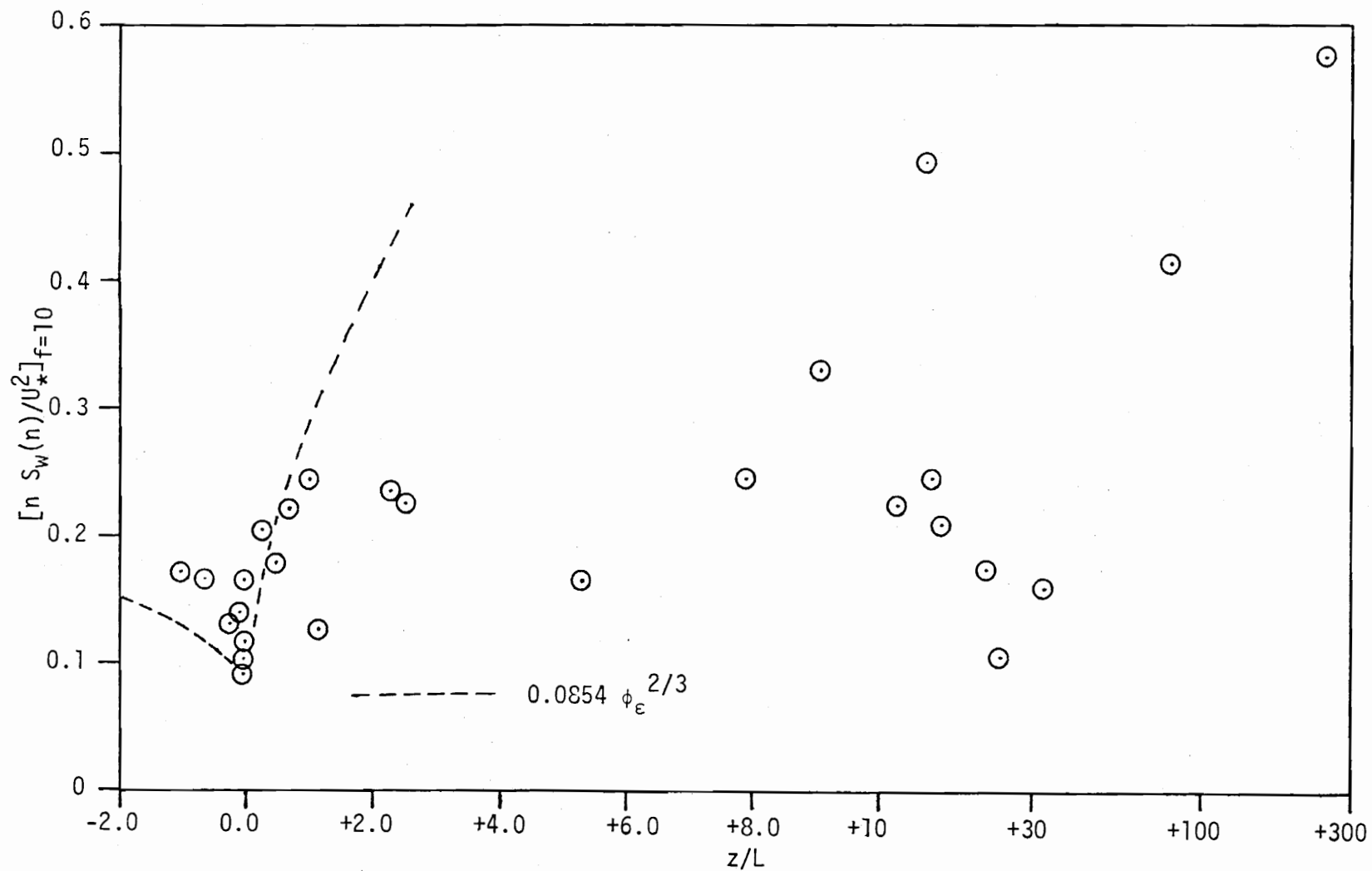


Figure 18. Estimates of the logarithmic spectra of the vertical velocity normalized by the local shear velocity at  $f=10$  versus stability.

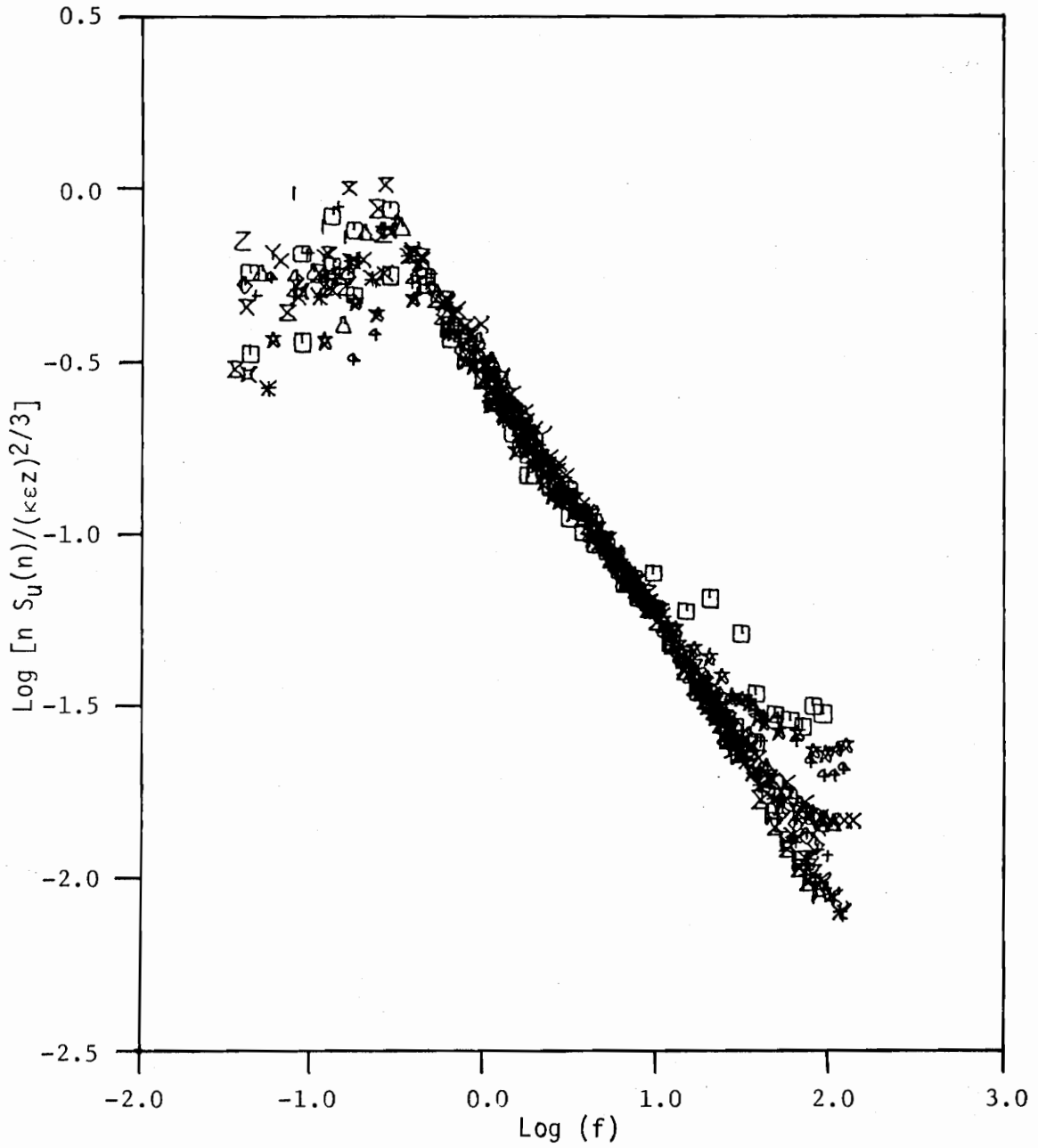


Figure 19a. Logarithmic spectra of the longitudinal velocity normalized with  $(\kappa \epsilon z)^{2/3}$  versus the reduced frequency, moderately unstable,  $-1.0 < z/L < 0$ .

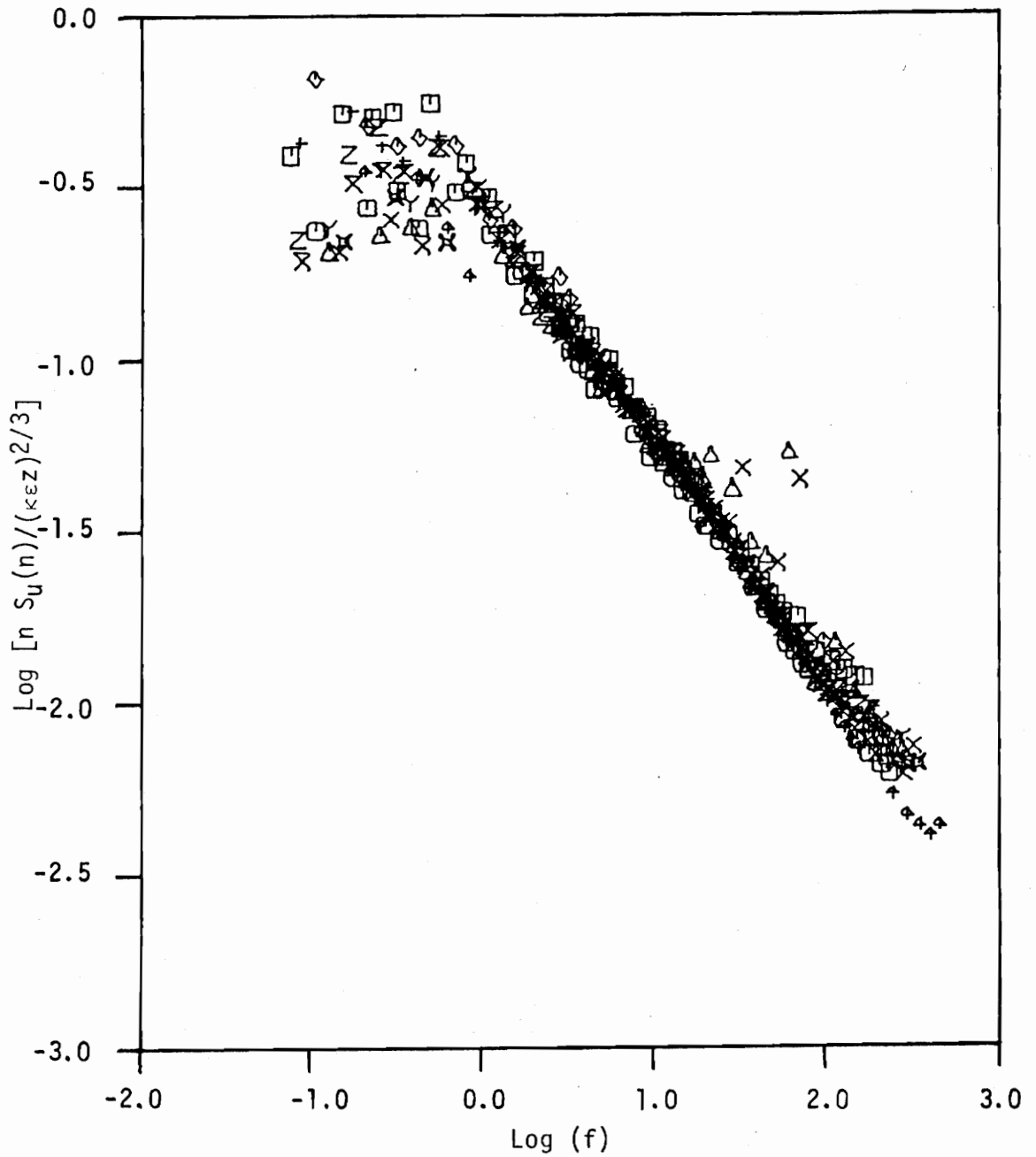


Figure 19b. Logarithmic spectra of the longitudinal velocity normalized with  $(\kappa \epsilon z)^{2/3}$  versus the reduced frequency, moderately stable,  $0 < z/L < +1.0$ .

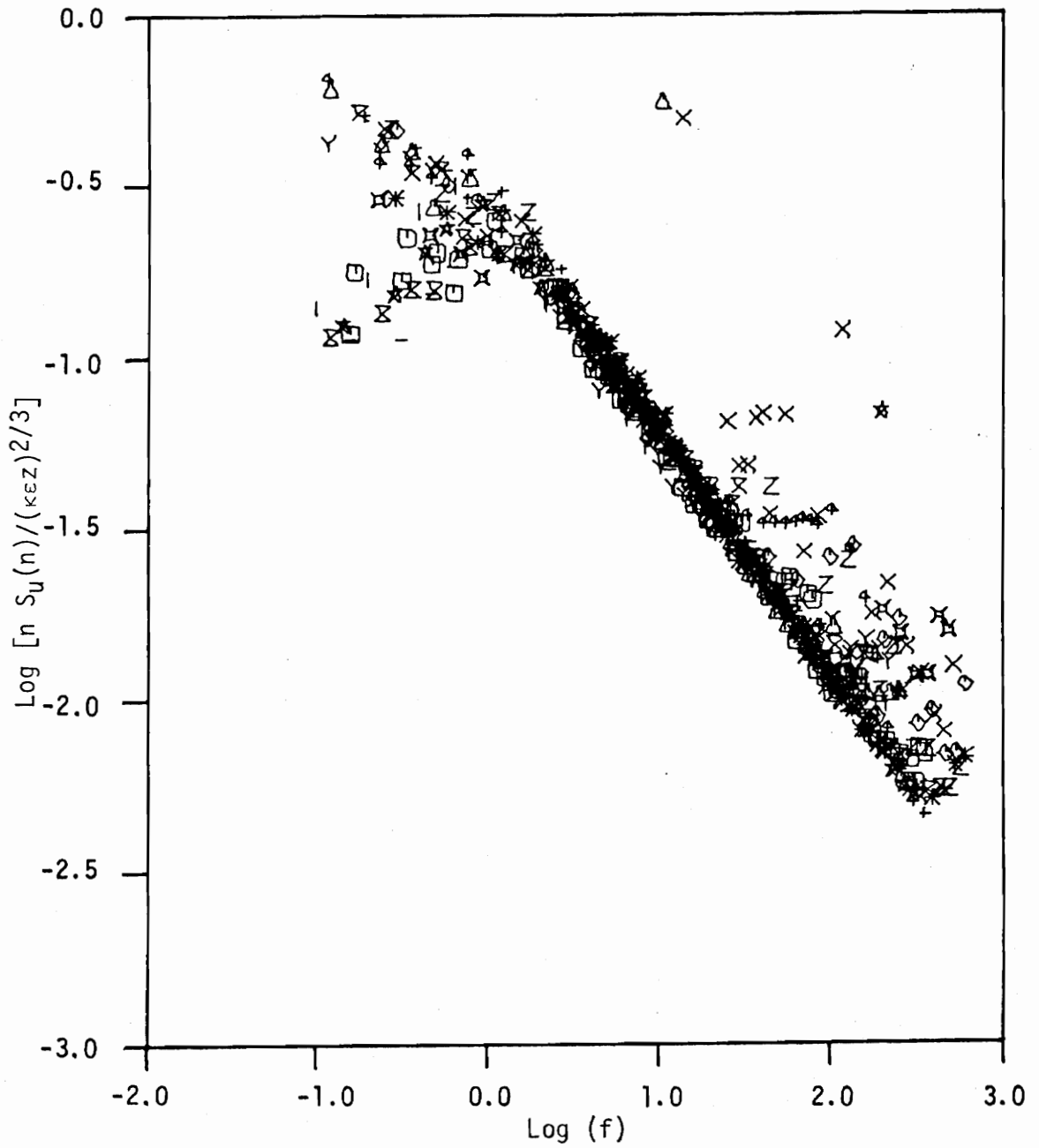


Figure 19c. Logarithmic spectra of the longitudinal velocity normalized with  $(\kappa \epsilon z)^{2/3}$  versus the reduced frequency, very stable,  $z/L > +1.0$ .

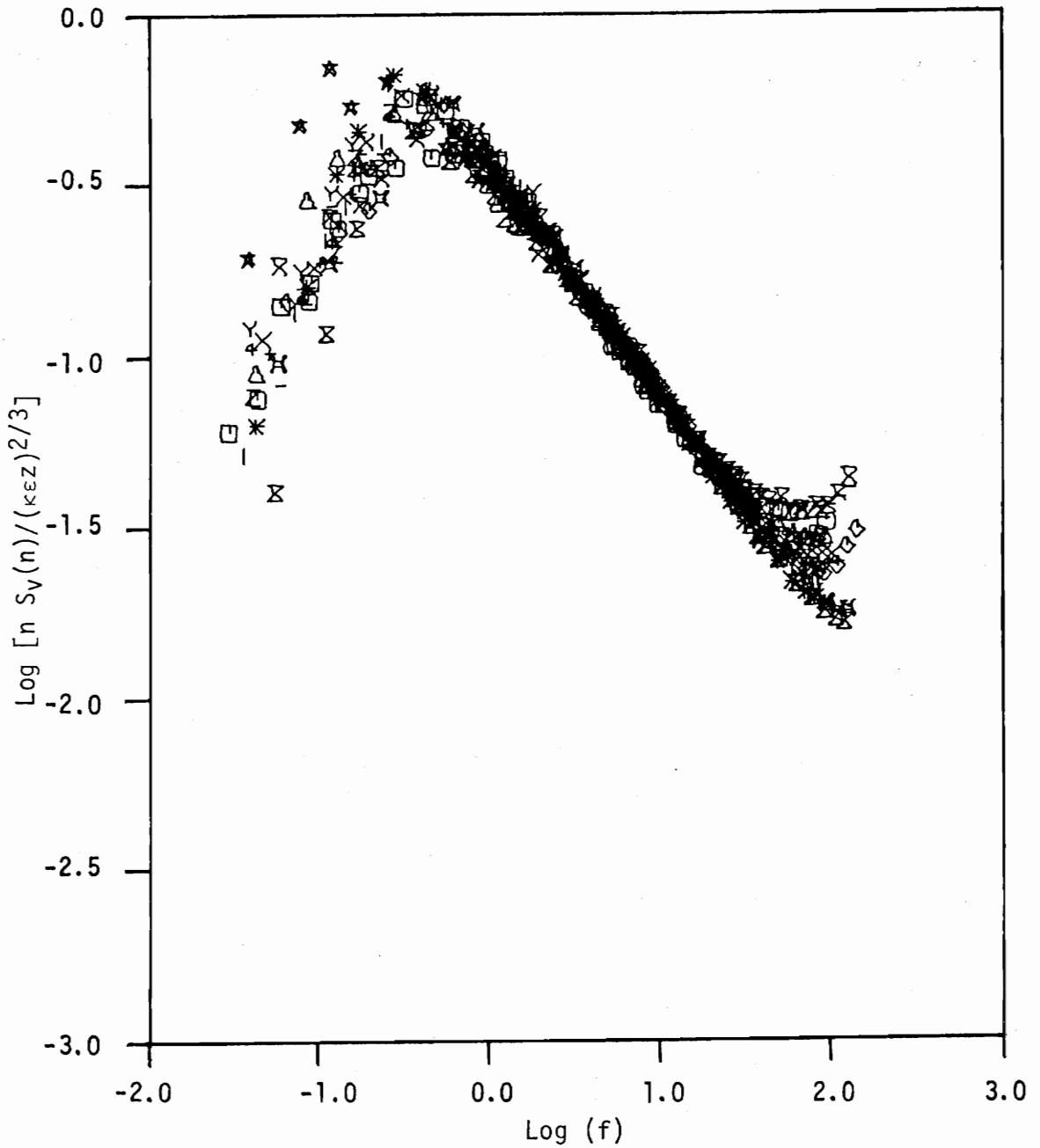


Figure 20a. Logarithmic spectra of the lateral velocity normalized with  $(\kappa \epsilon z)^{2/3}$  versus the reduced frequency, moderately unstable,  $-1.0 < z/L < 0$ .

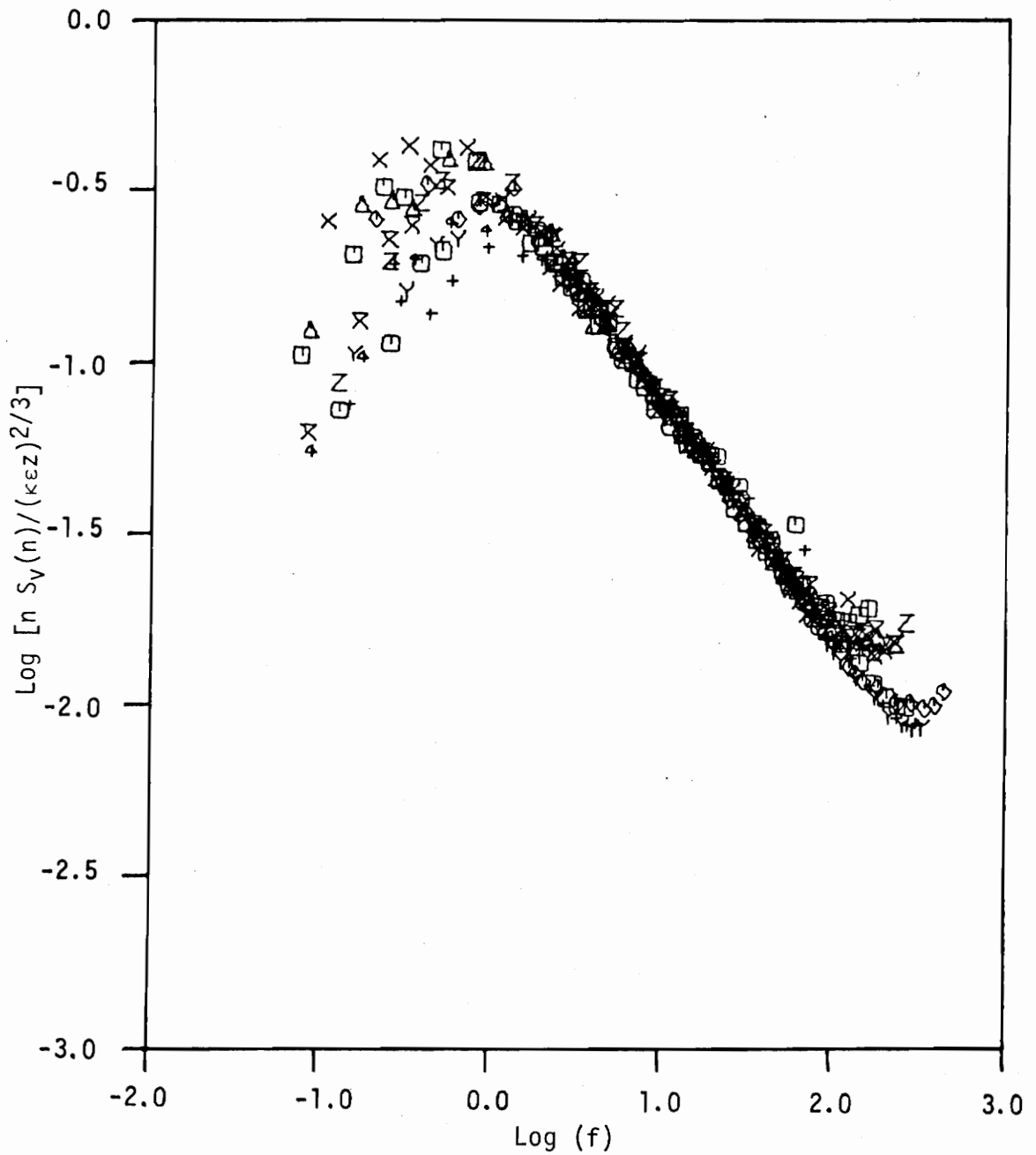


Figure 20b. Logarithmic spectra of the lateral velocity normalized with  $(\kappa \epsilon \zeta)^{2/3}$  versus the reduced frequency, moderately stable,  $0 < z/L < +1.0$ .

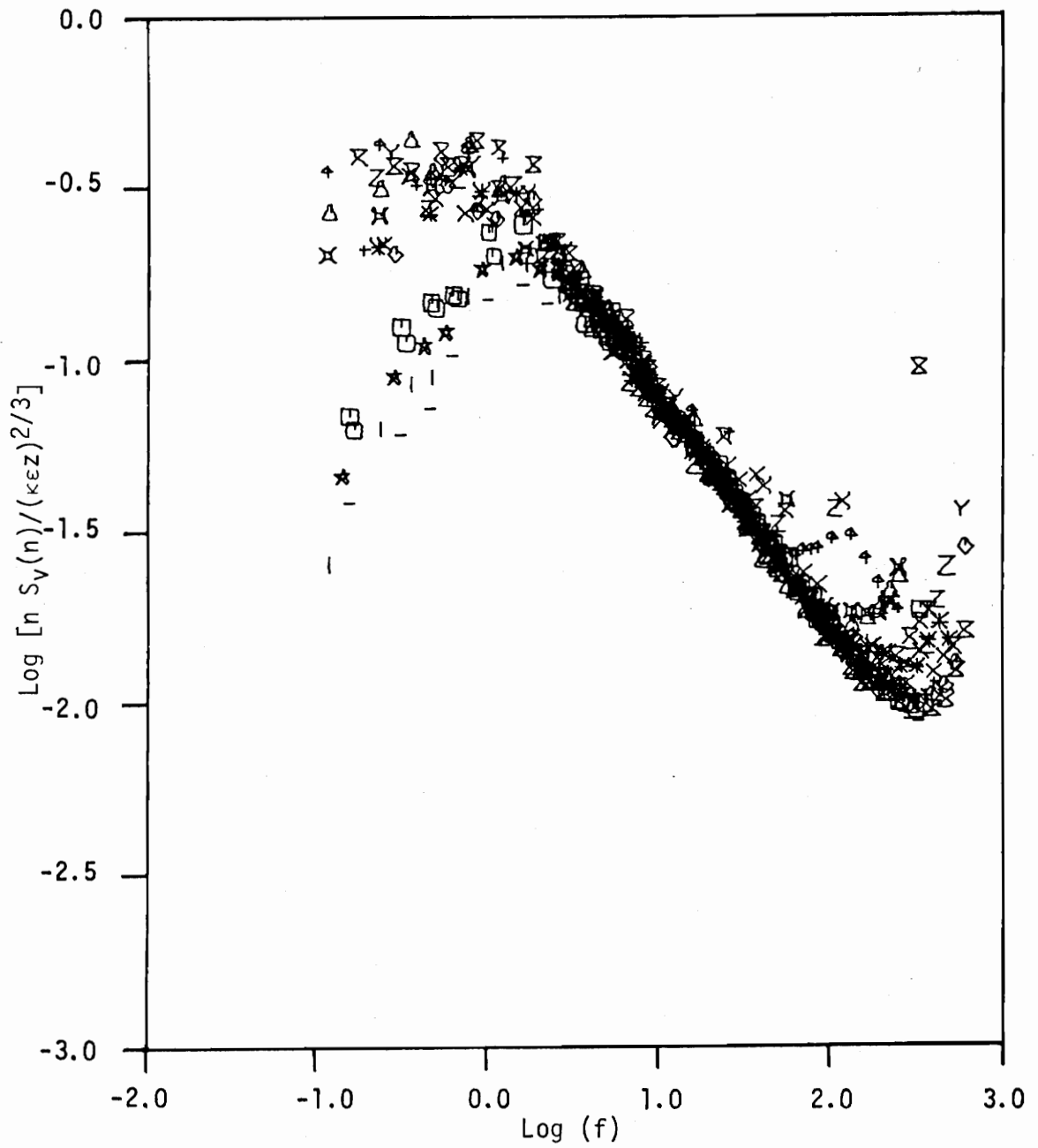


Figure 20c. Logarithmic spectra of the lateral velocity normalized with  $(\kappa \epsilon z)^{2/3}$  versus the reduced frequency, very stable,  $z/L > +1.0$ .



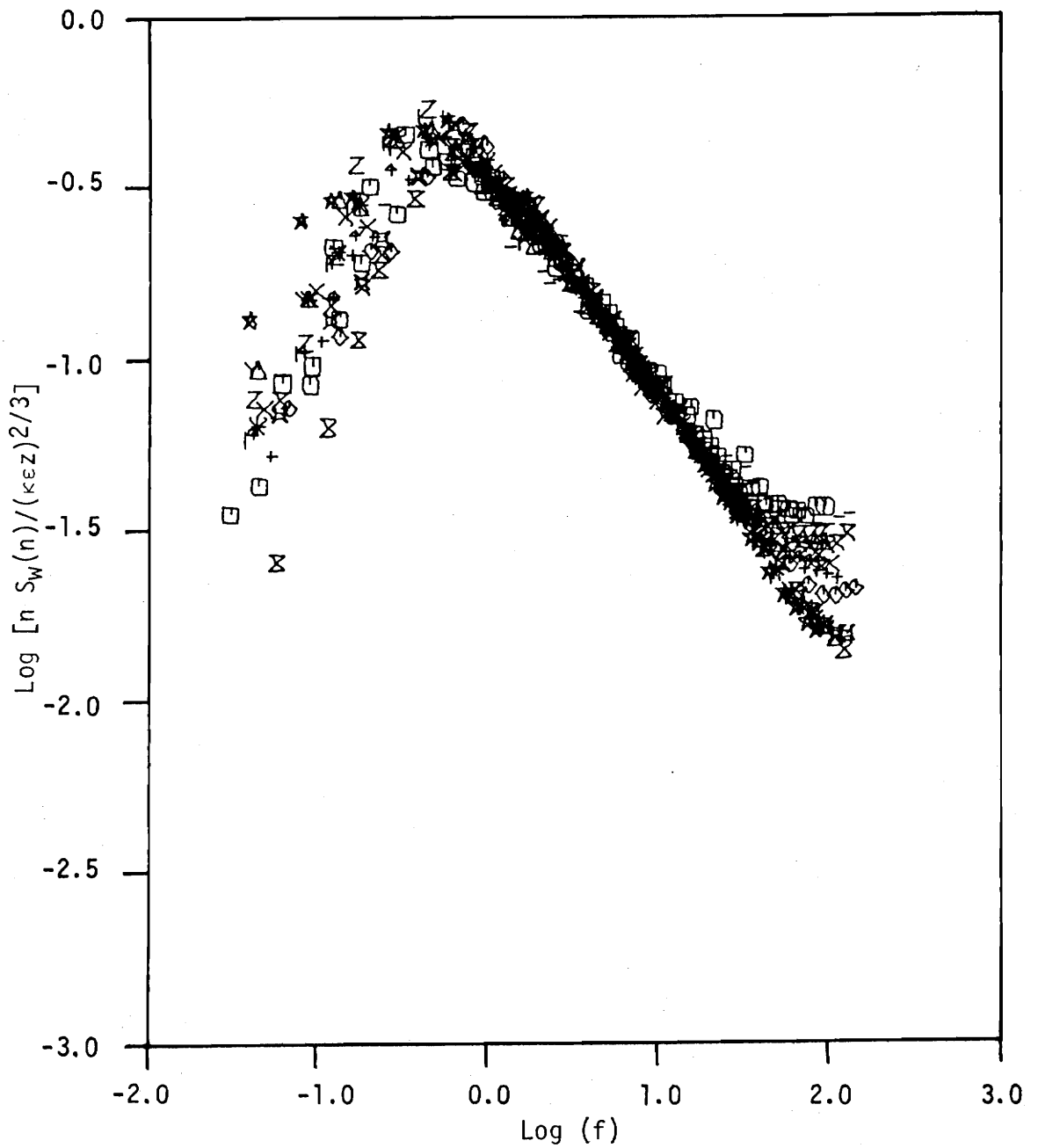


Figure 21a. Logarithmic spectra of the vertical velocity normalized with  $(\kappa \epsilon z)^{2/3}$  versus the reduced frequency, moderately unstable,  $-1.0 < z/L < 0$ .

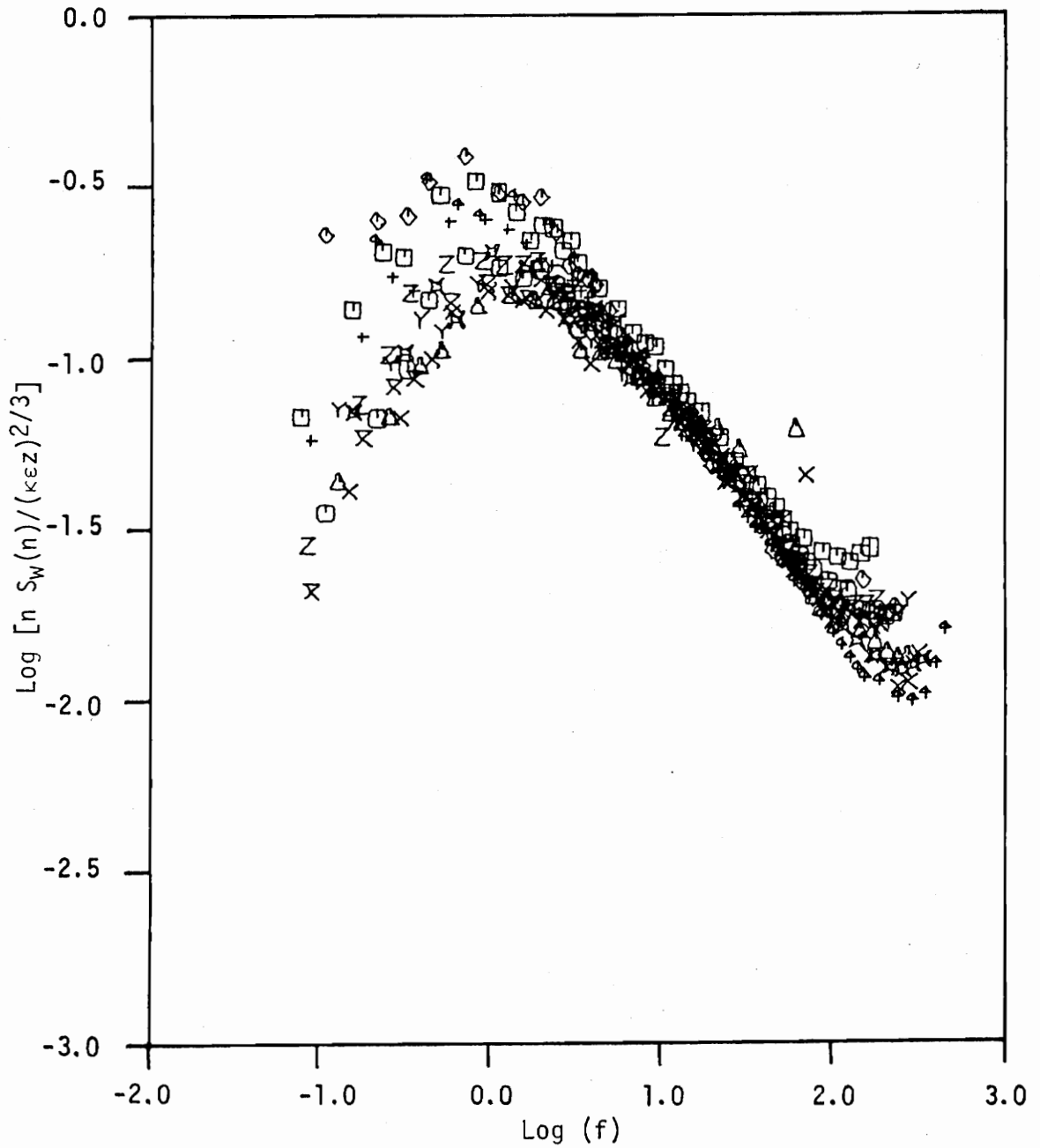


Figure 21b. Logarithmic spectra of the vertical velocity normalized with  $(\kappa \epsilon z)^{2/3}$  versus the reduced frequency, moderately stable,  $0 < z/L < +1.0$ .

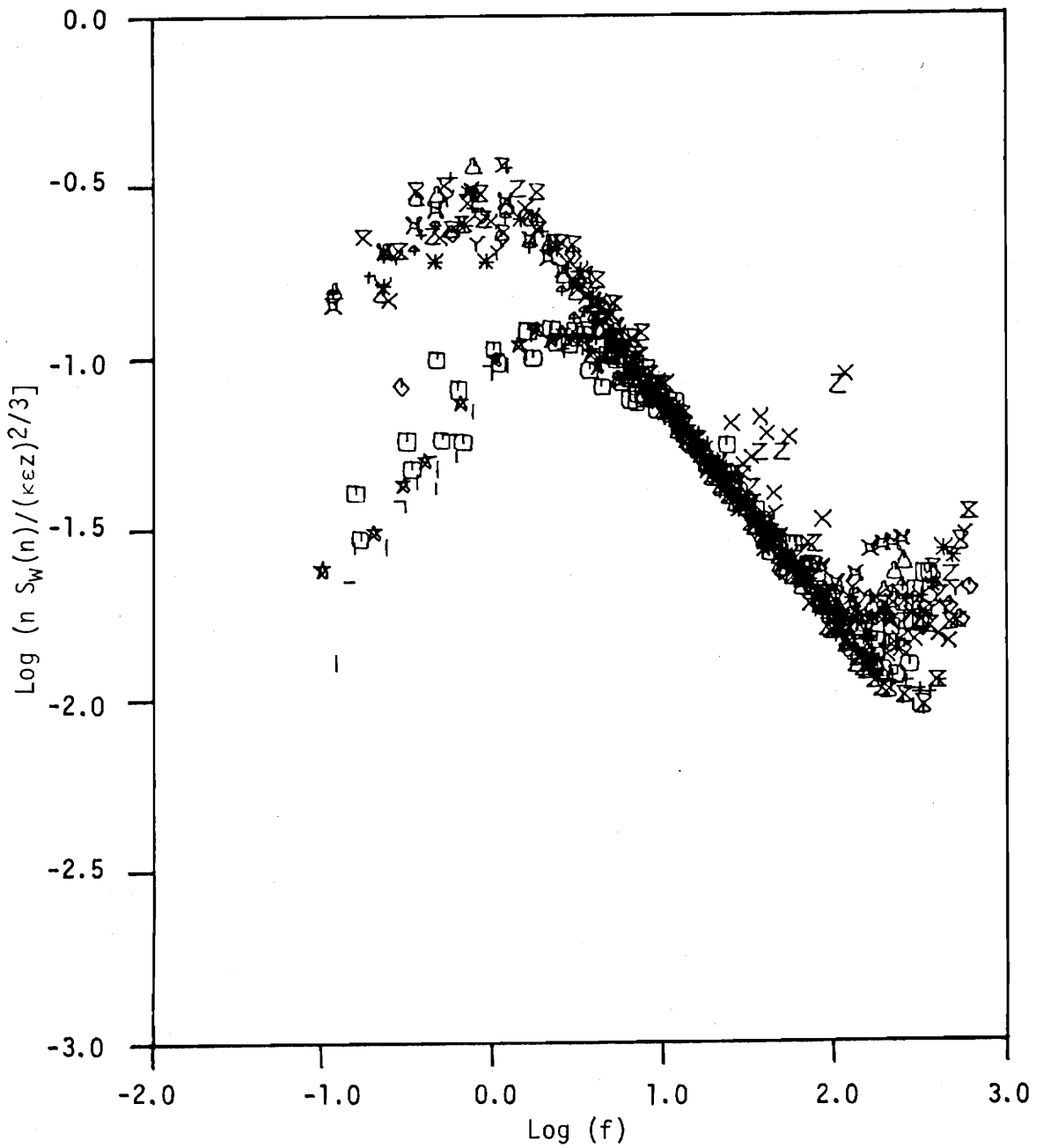


Figure 21c. Logarithmic spectra of the vertical velocity normalized with  $(k\epsilon z)^{2/3}$  versus the reduced frequency, very stable,  $z/L > +1.0$ .

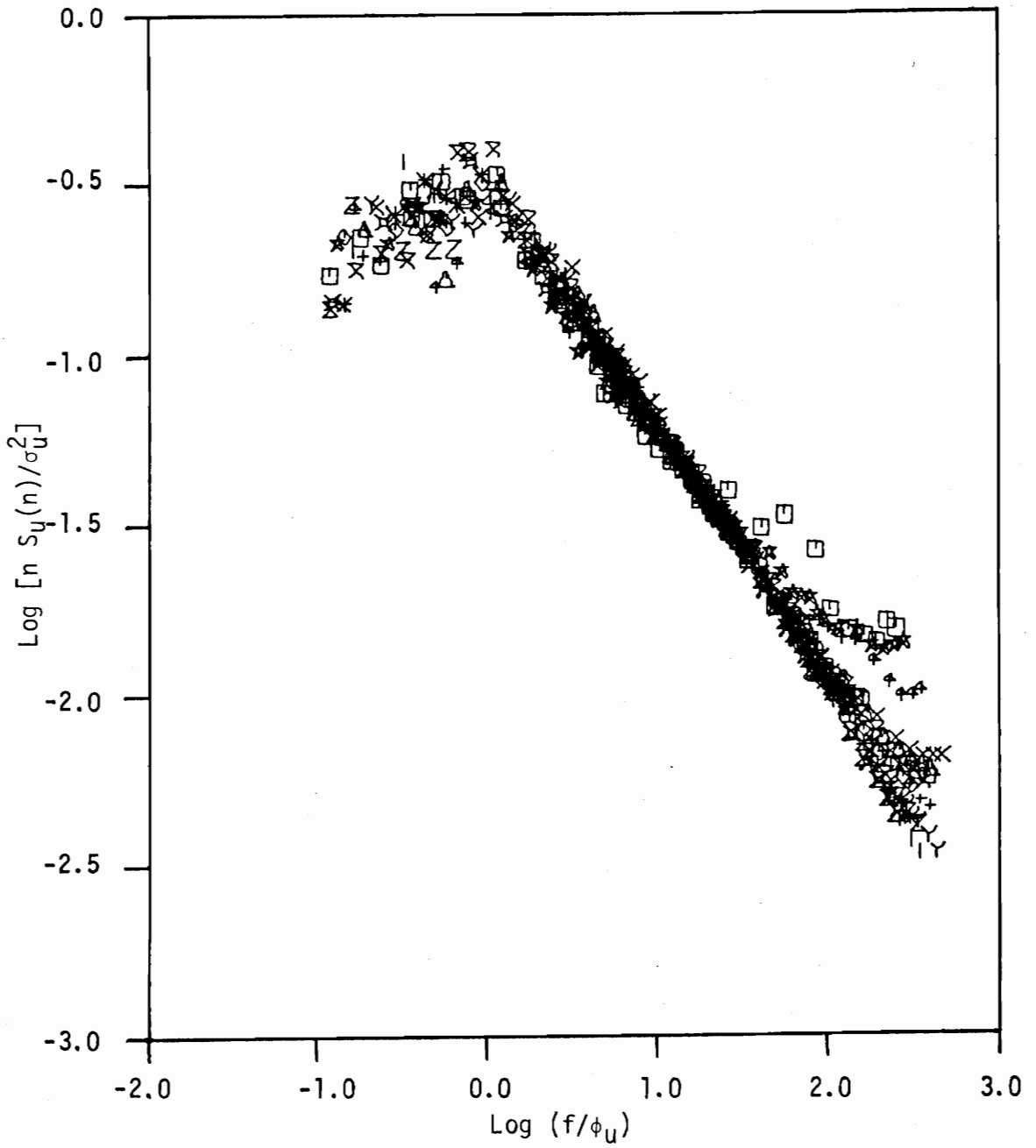


Figure 22a. Logarithmic spectra of the longitudinal velocity normalized by the variance versus  $f/\phi_u$ , moderately unstable,  $-1.0 < z/L < 0$ .

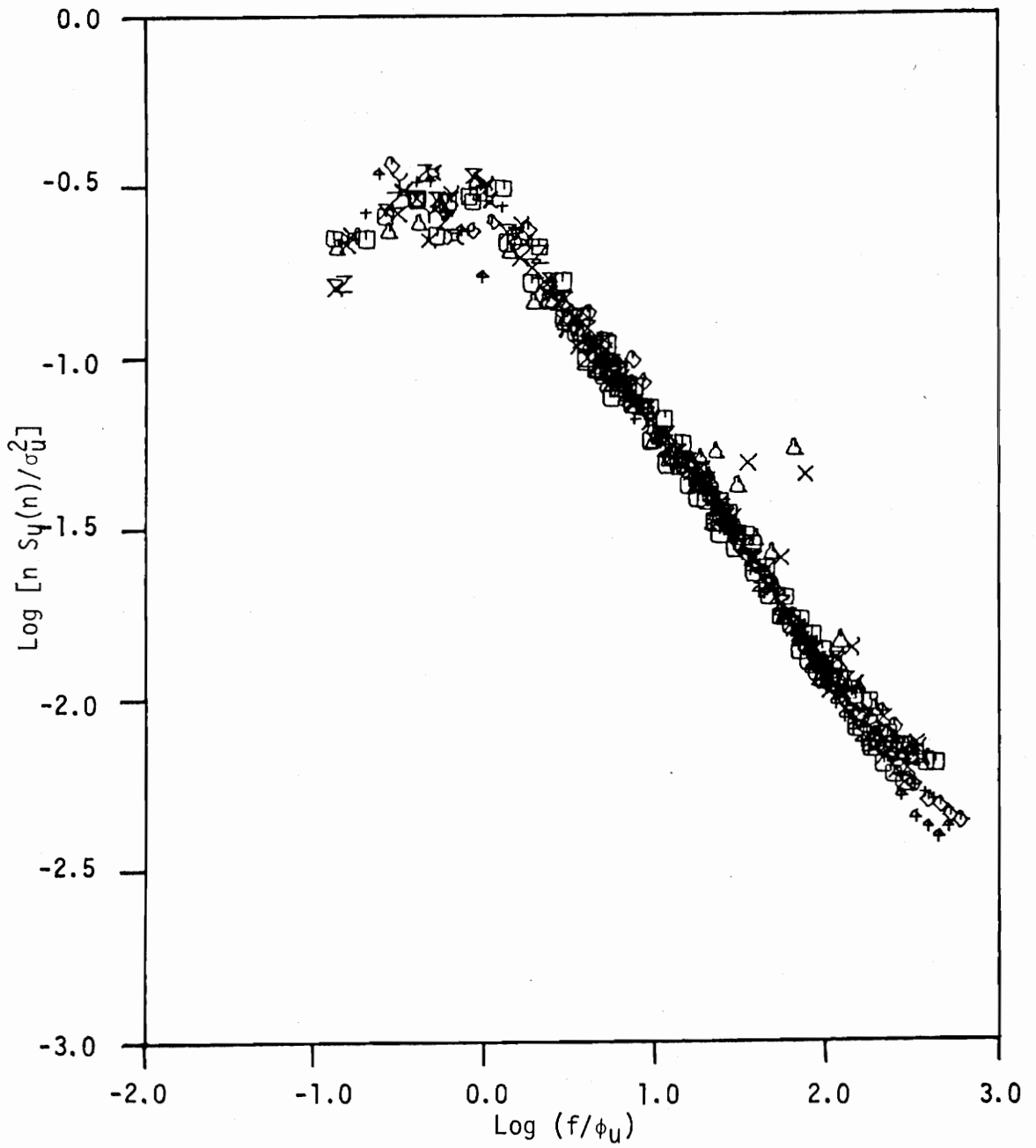


Figure 22b. Logarithmic spectra of the longitudinal velocity normalized by the variance versus  $f/\phi_u$ , moderately stable,  $0 < z/L < +1.0$ .

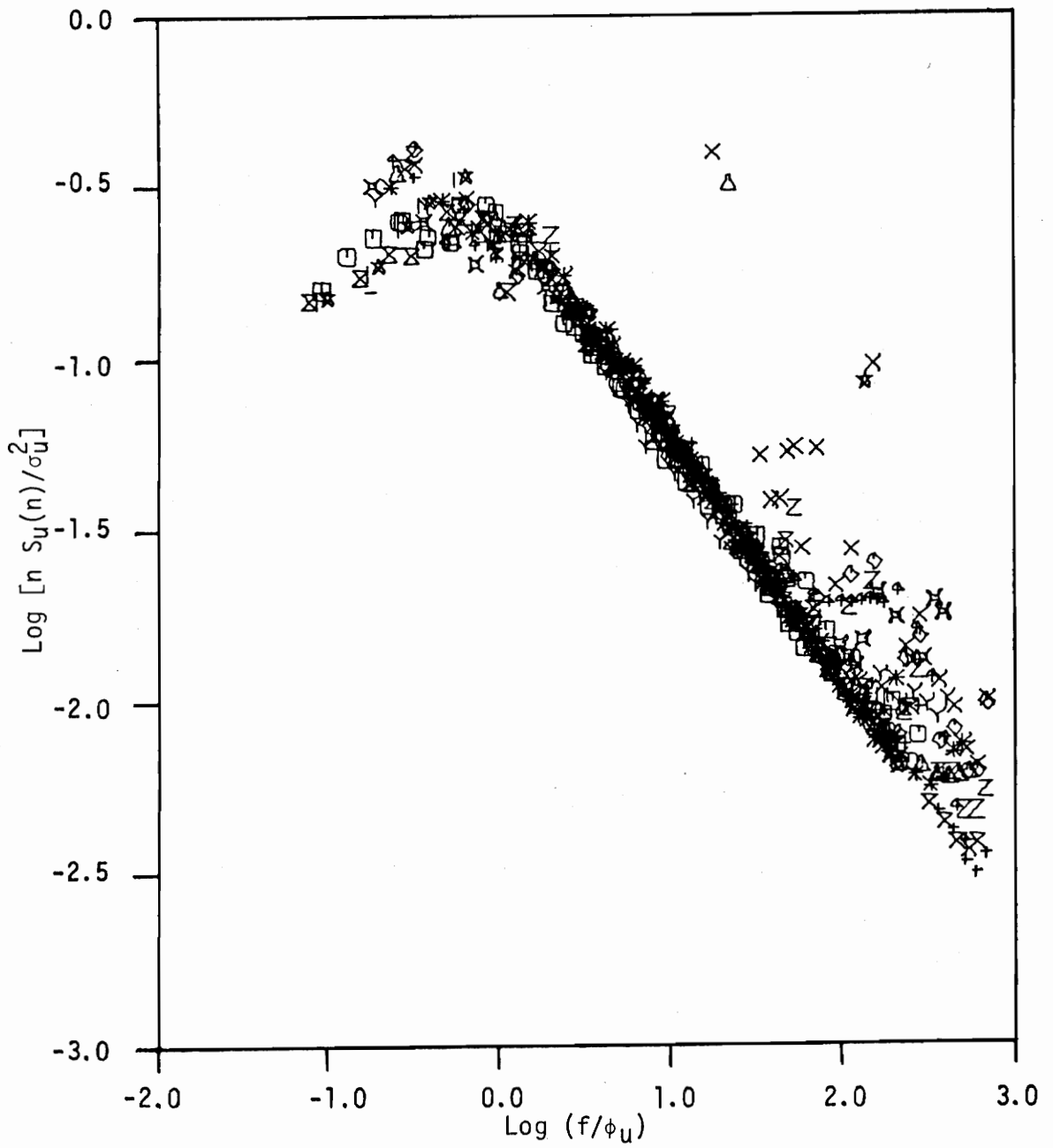


Figure 22c. Logarithmic spectra of the longitudinal velocity normalized by the variance versus  $f/\phi_U$ , very stable,  $z/L > +1.0$ .

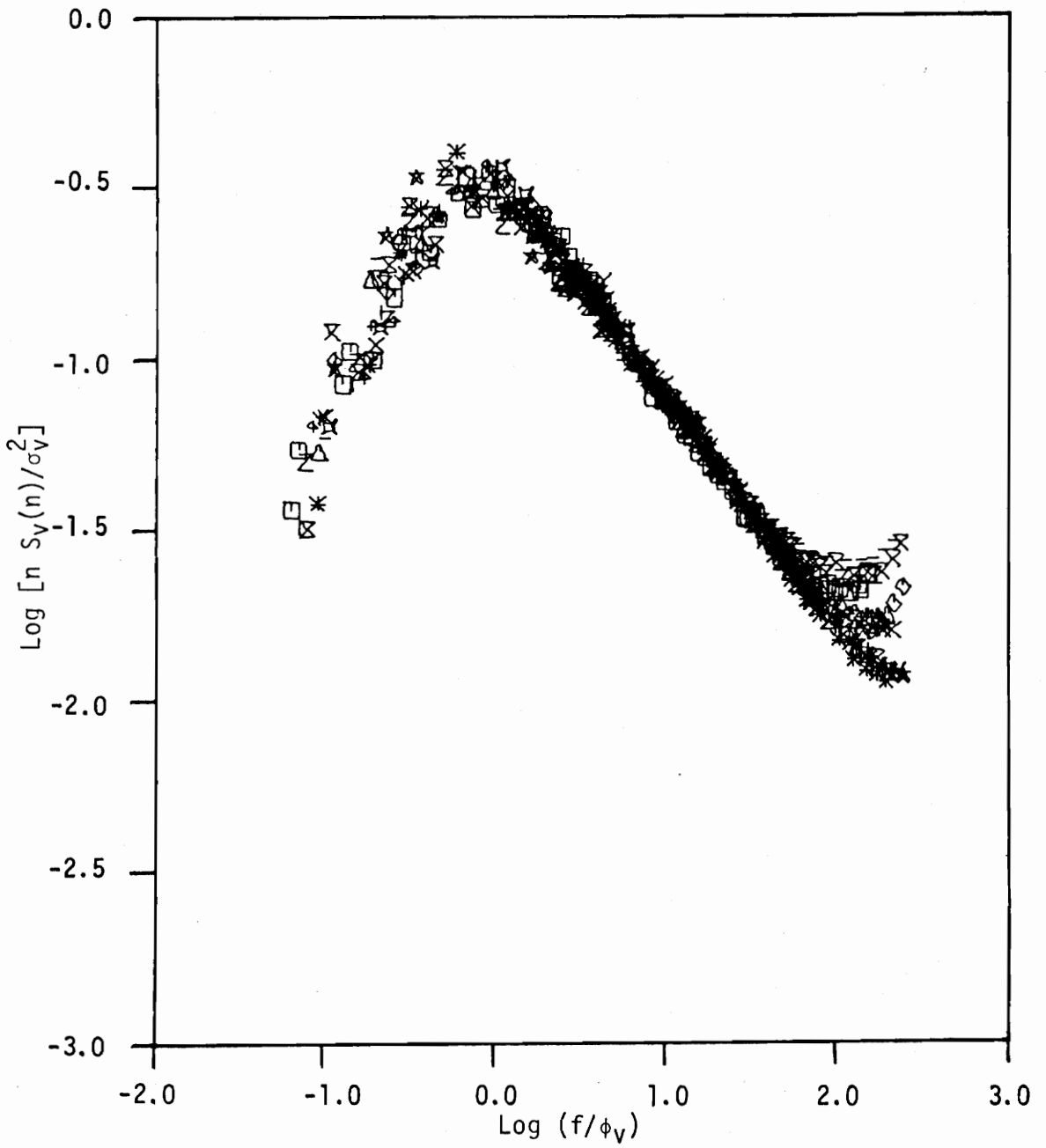


Figure 23a. Logarithmic spectra of the lateral velocity normalized by the variance versus  $f/\phi_V$ , moderately unstable,  $-1.0 < z/L < 0$ .

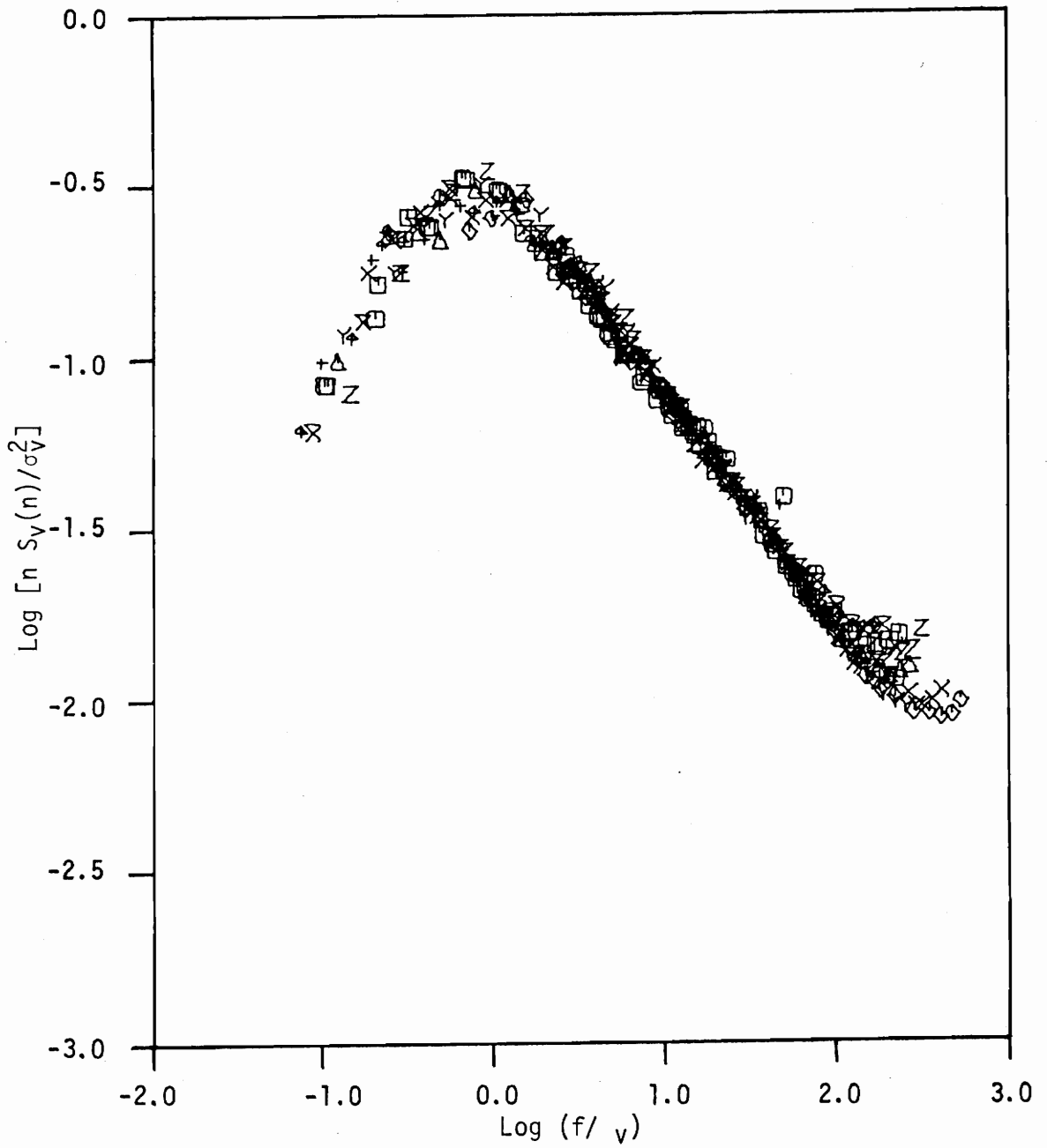


Figure 23b. Logarithmic spectra of the lateral velocity normalized by the variance versus  $f/\phi_v$ , moderately stable,  $0 < z/L < +1.0$ .



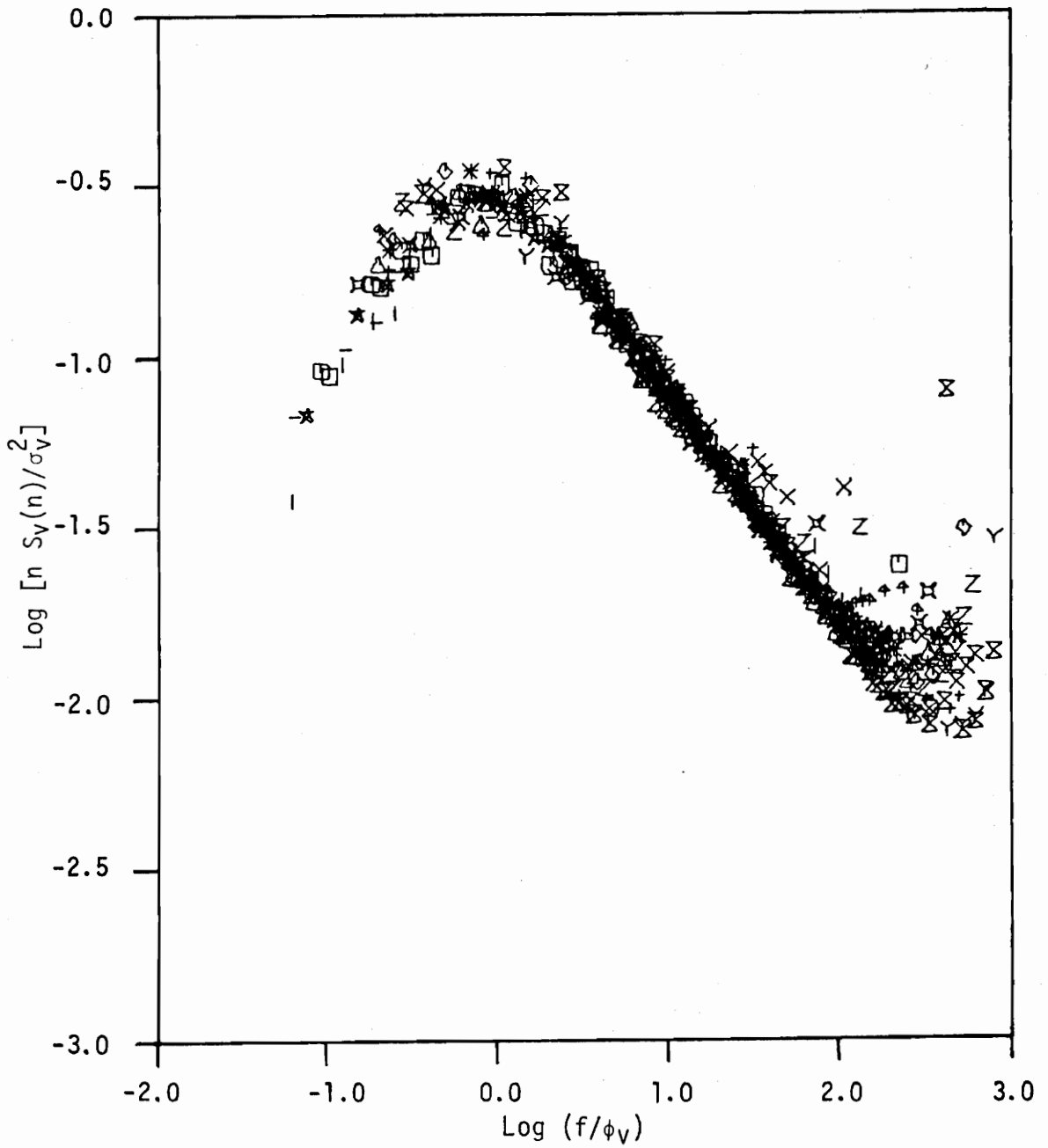


Figure 23c. Logarithmic spectra of the lateral velocity normalized by the variance versus  $f/\phi_V$ , very stable,  $z/L > +1.0$ .

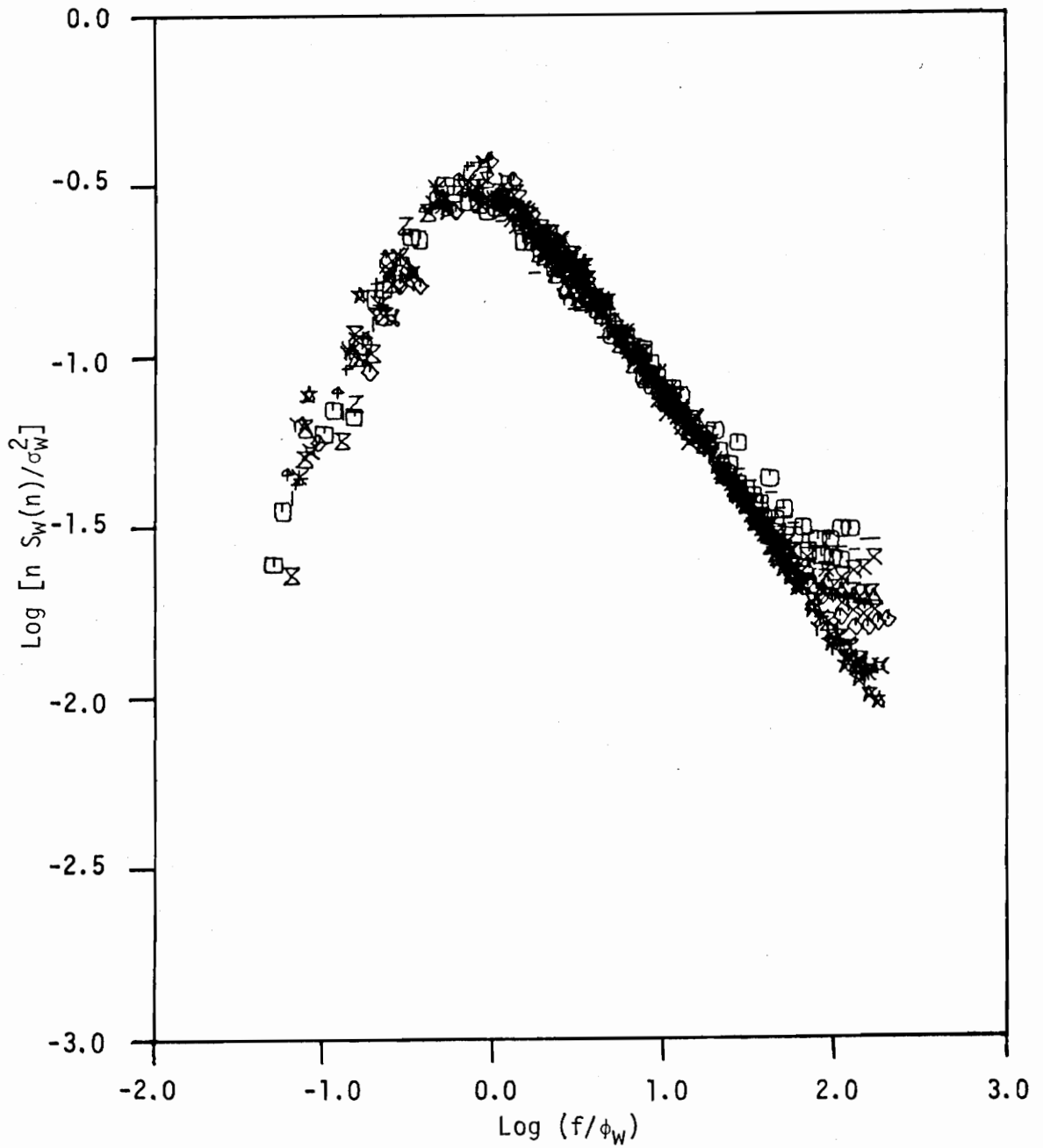


Figure 24a. Logarithmic spectra of the vertical velocity normalized by the variance versus  $f/\phi_w$ , moderately unstable,  $-1.0 < z/L < 0$ .

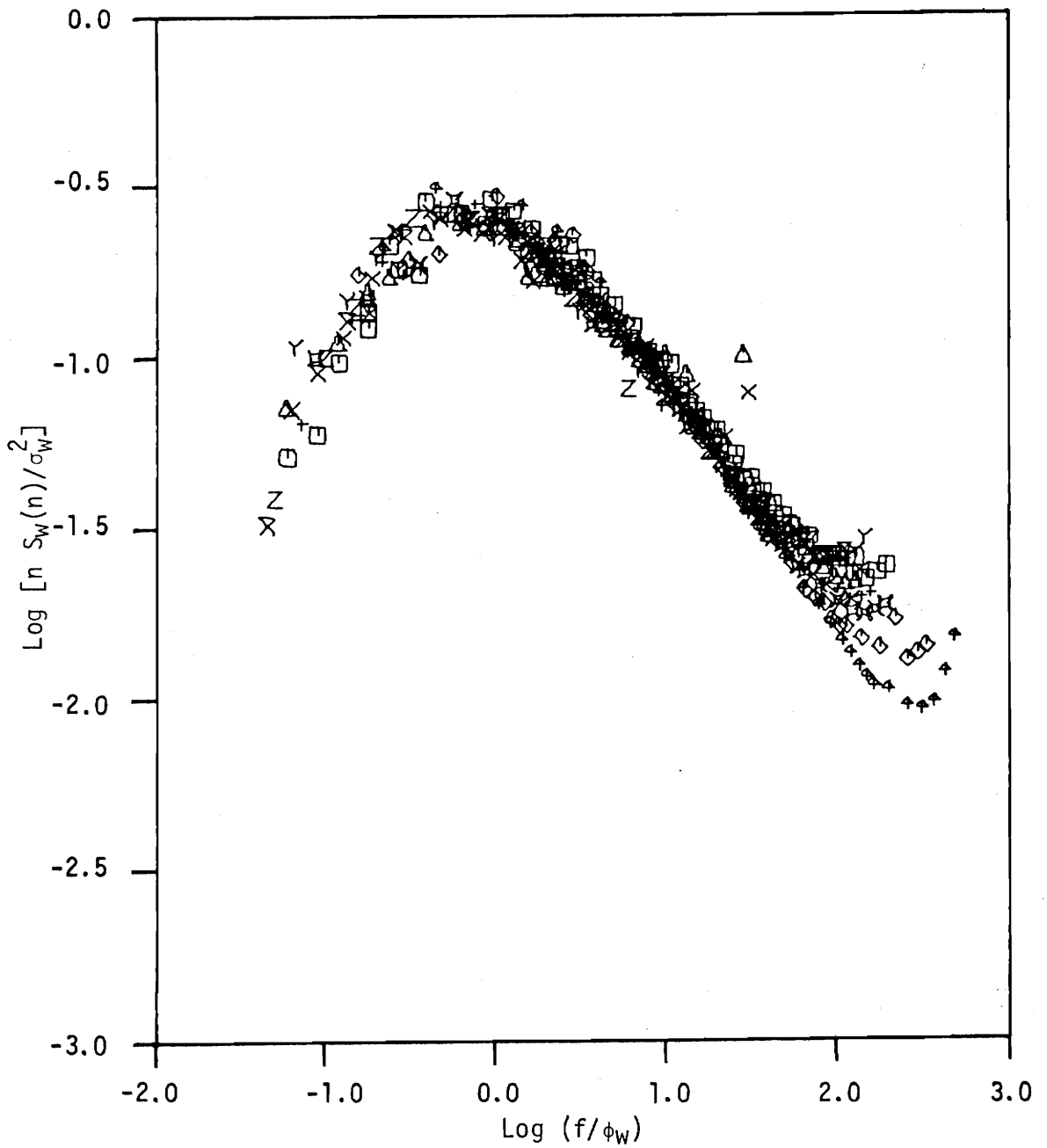


Figure 24b. Logarithmic spectra of the vertical velocity normalized by the variance versus  $f/\phi_W$ , moderately stable,  $0 < z/L < +1.0$ .

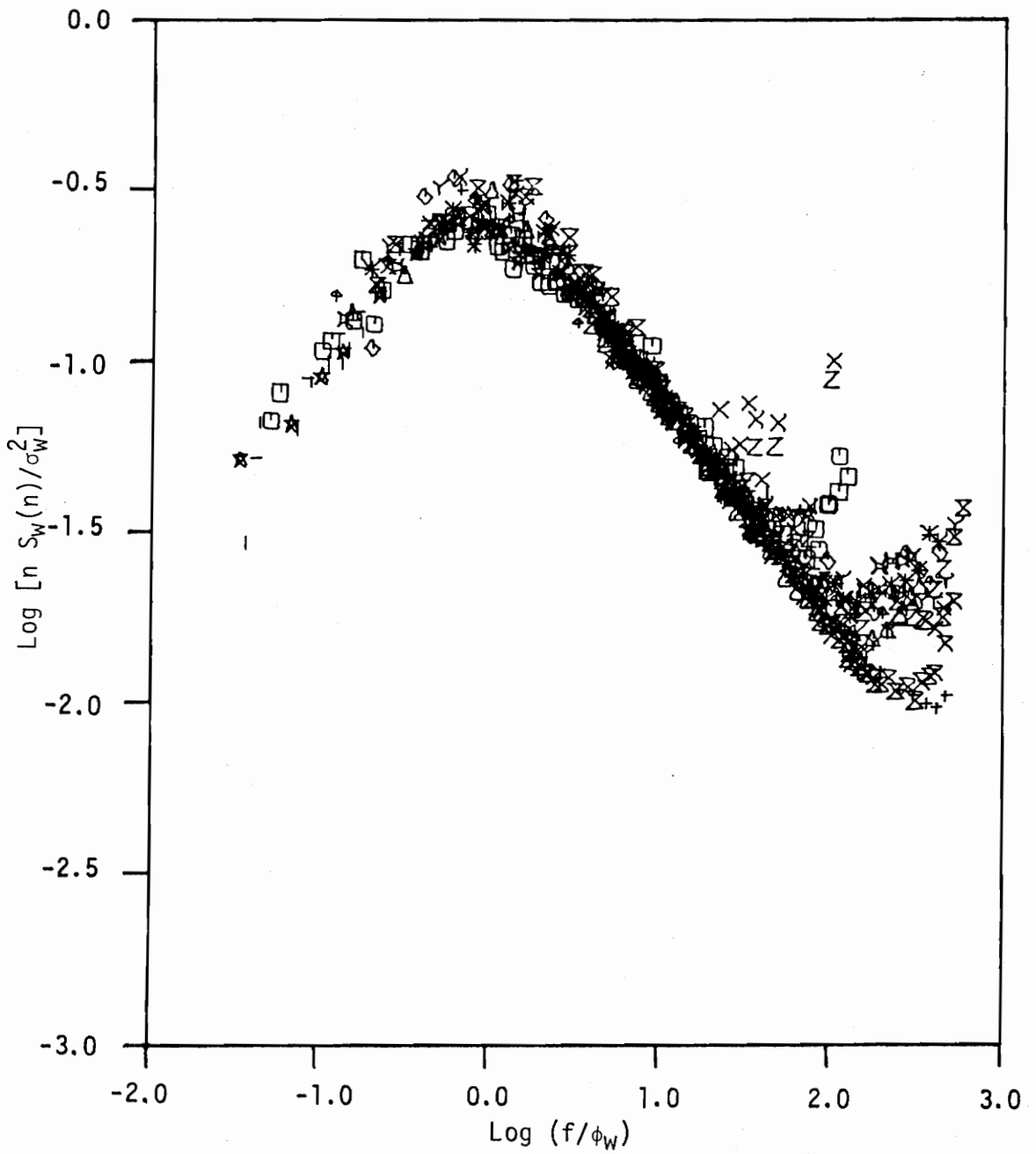


Figure 24c. Logarithmic spectra of the vertical velocity normalized by the variance versus  $f/\phi_w$ , very stable,  $z/L > +1.0$ .

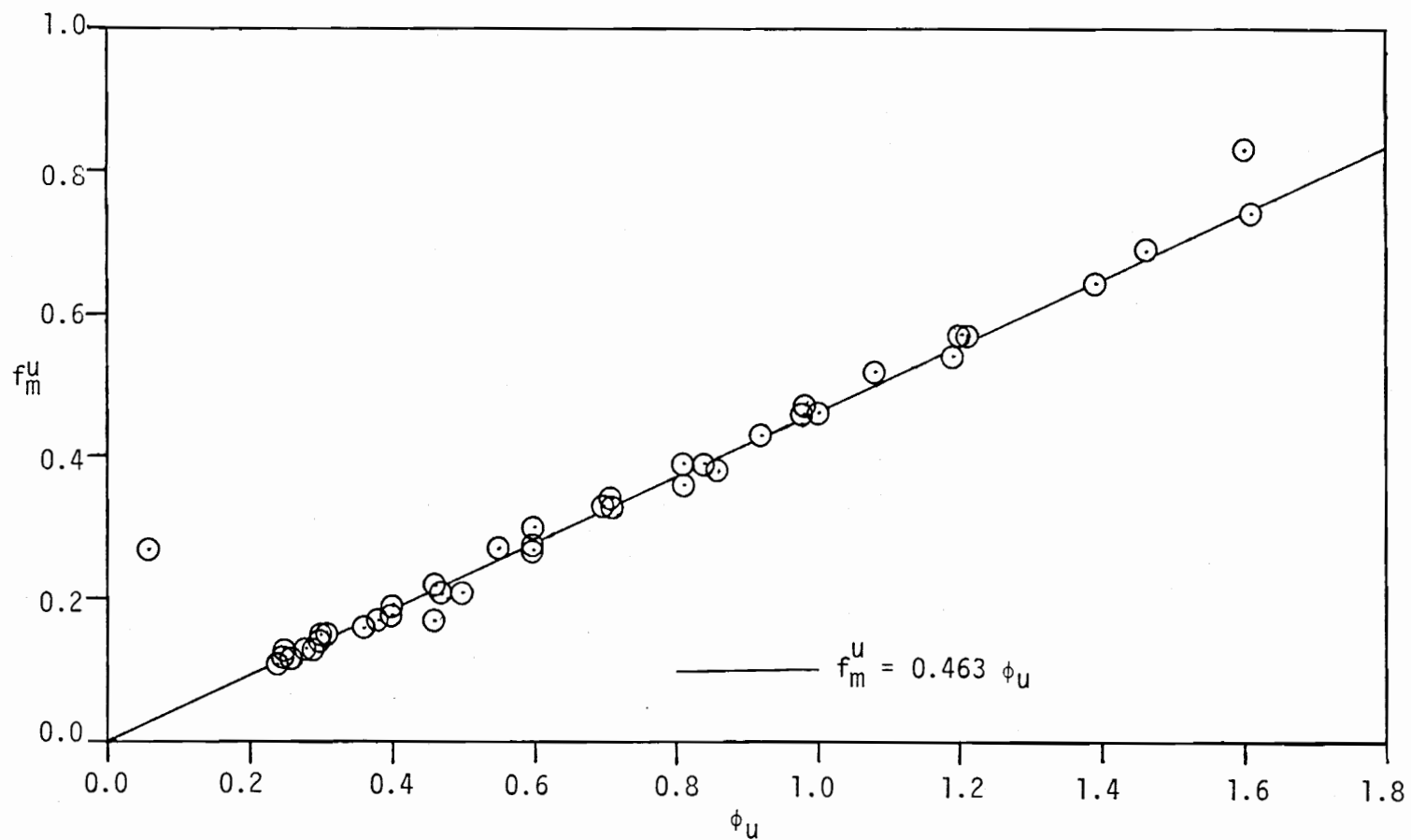


Figure 25. Variation of the reduced peak-frequencies of the longitudinal spectra with the dissipation parameter  $\phi_u$ .

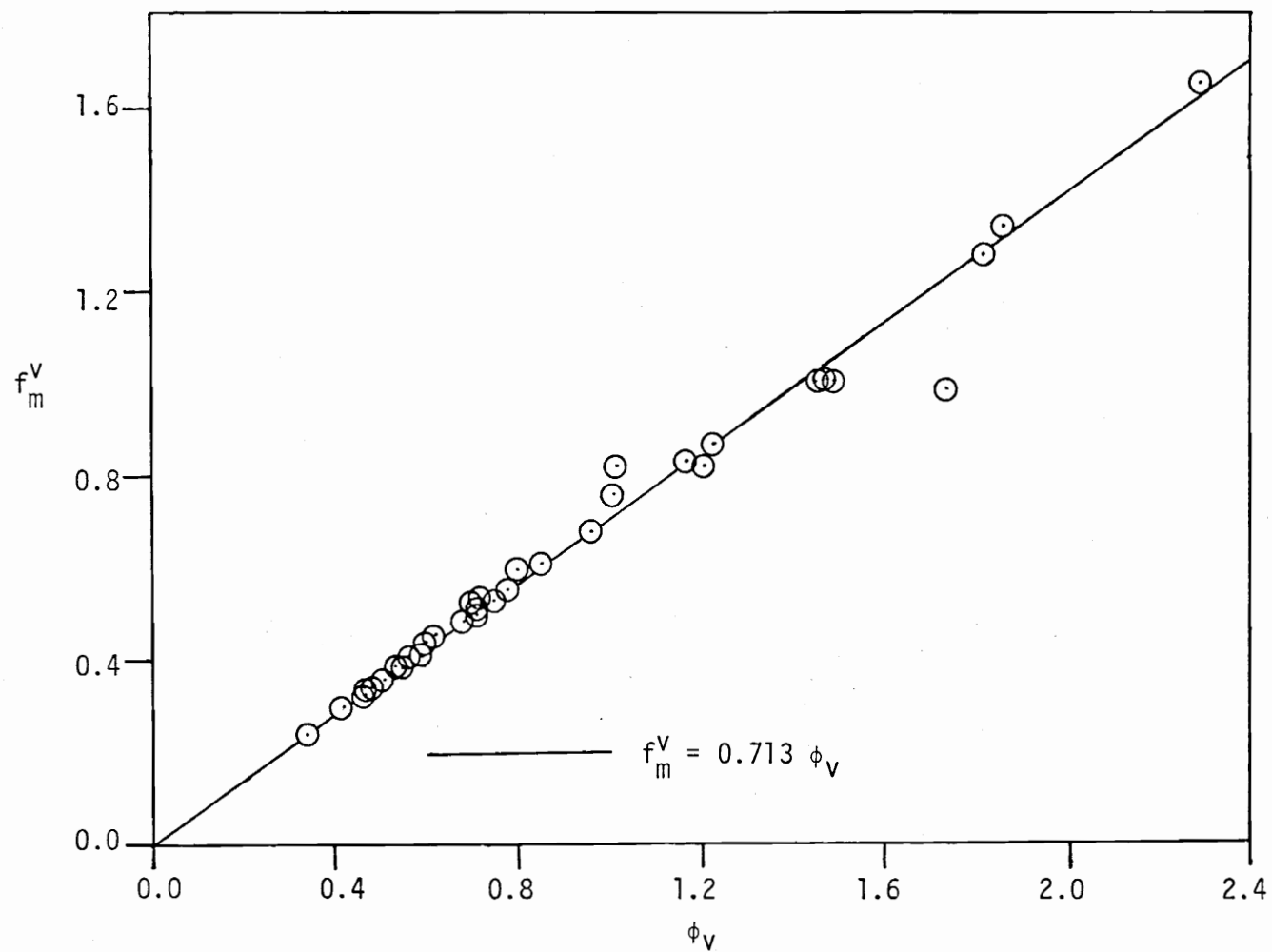


Figure 26. Variation of the reduced peak-frequencies of the lateral spectra with the dissipation parameter  $\phi_V$ .

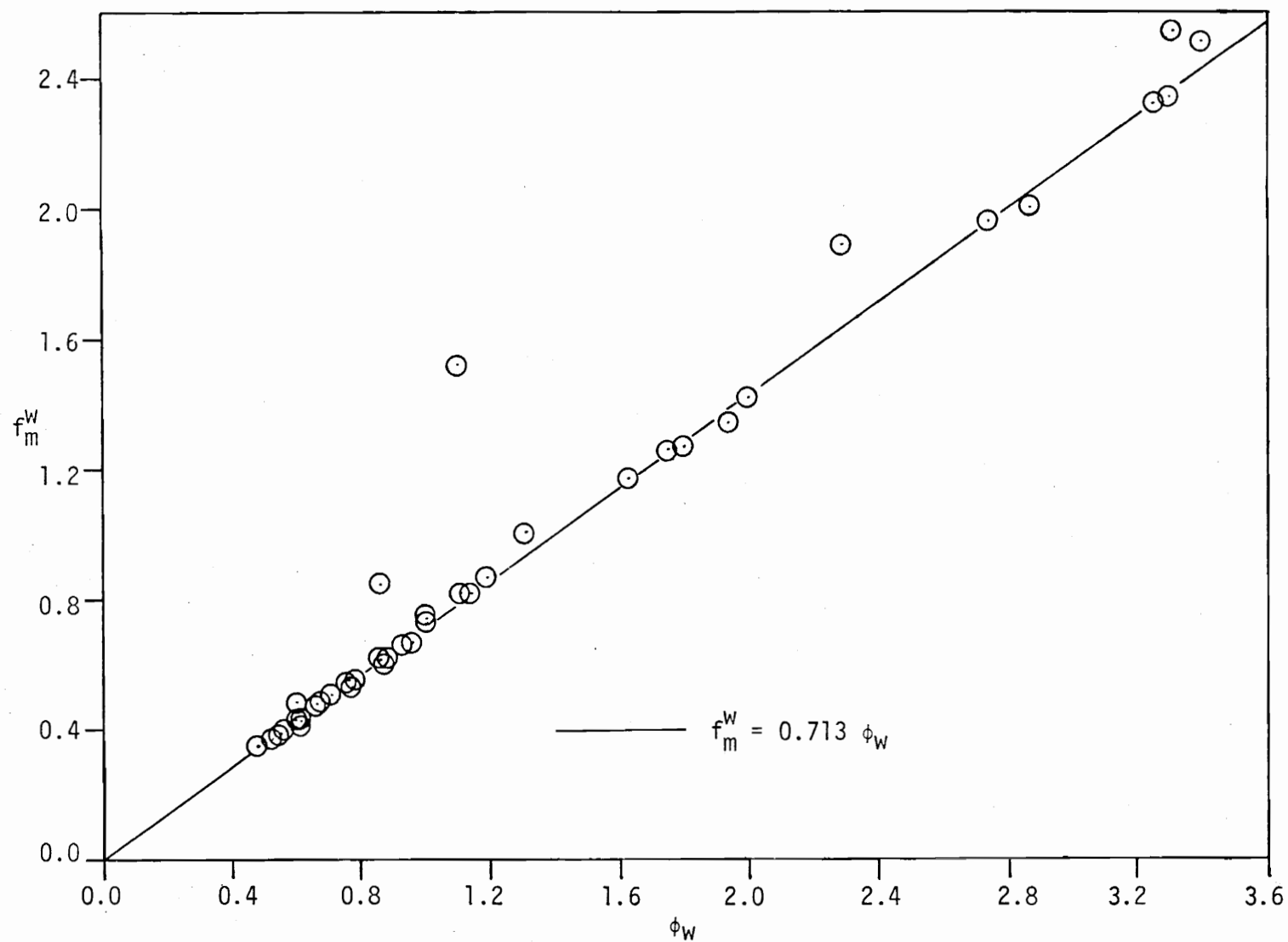


Figure 27. Variation of the reduced peak-frequencies of the vertical spectra with the dissipation parameter  $\phi_W$ .

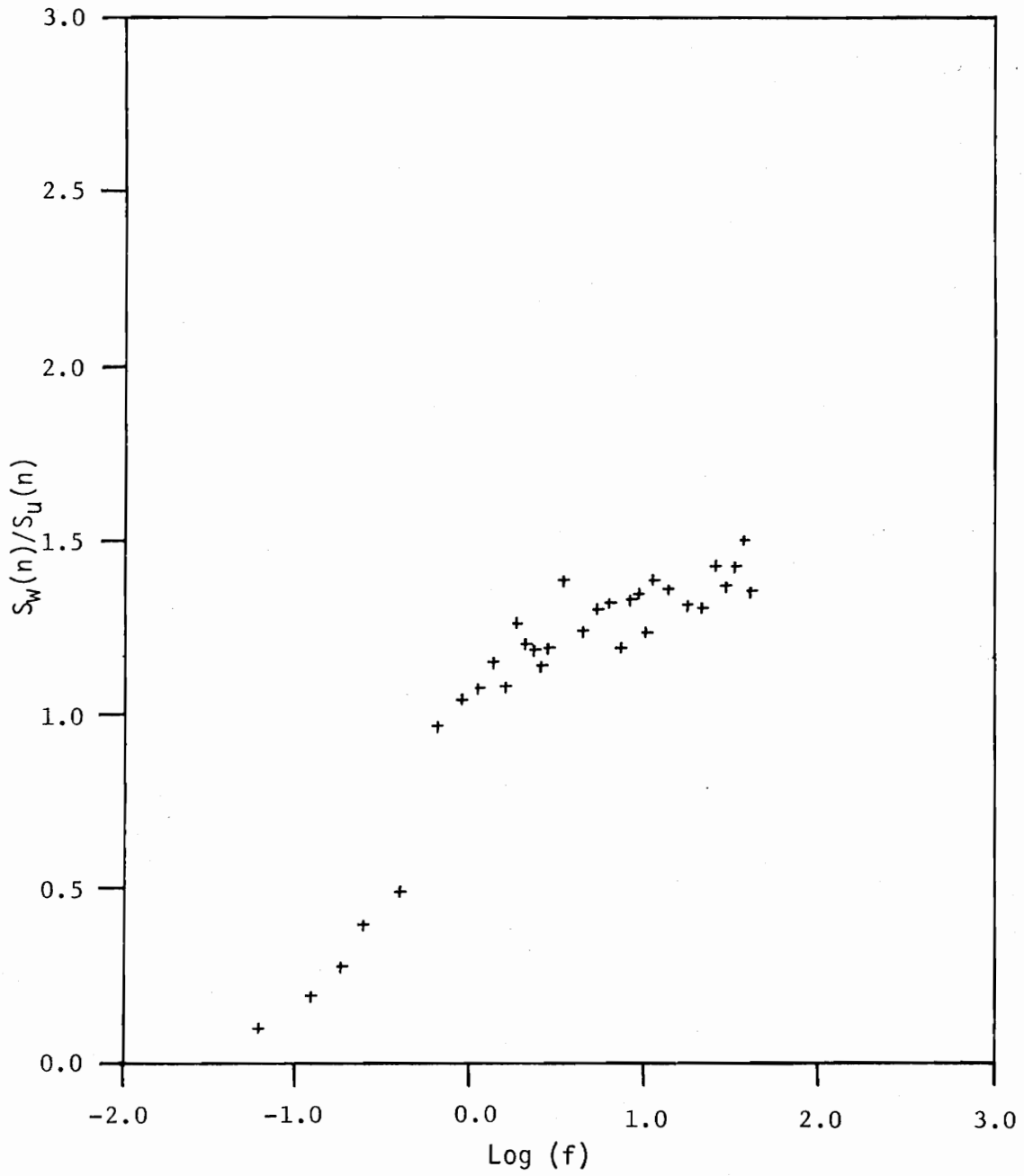


Figure 28. Ratio of vertical and longitudinal velocity spectra versus reduced frequency, Run 6, 50-foot level.



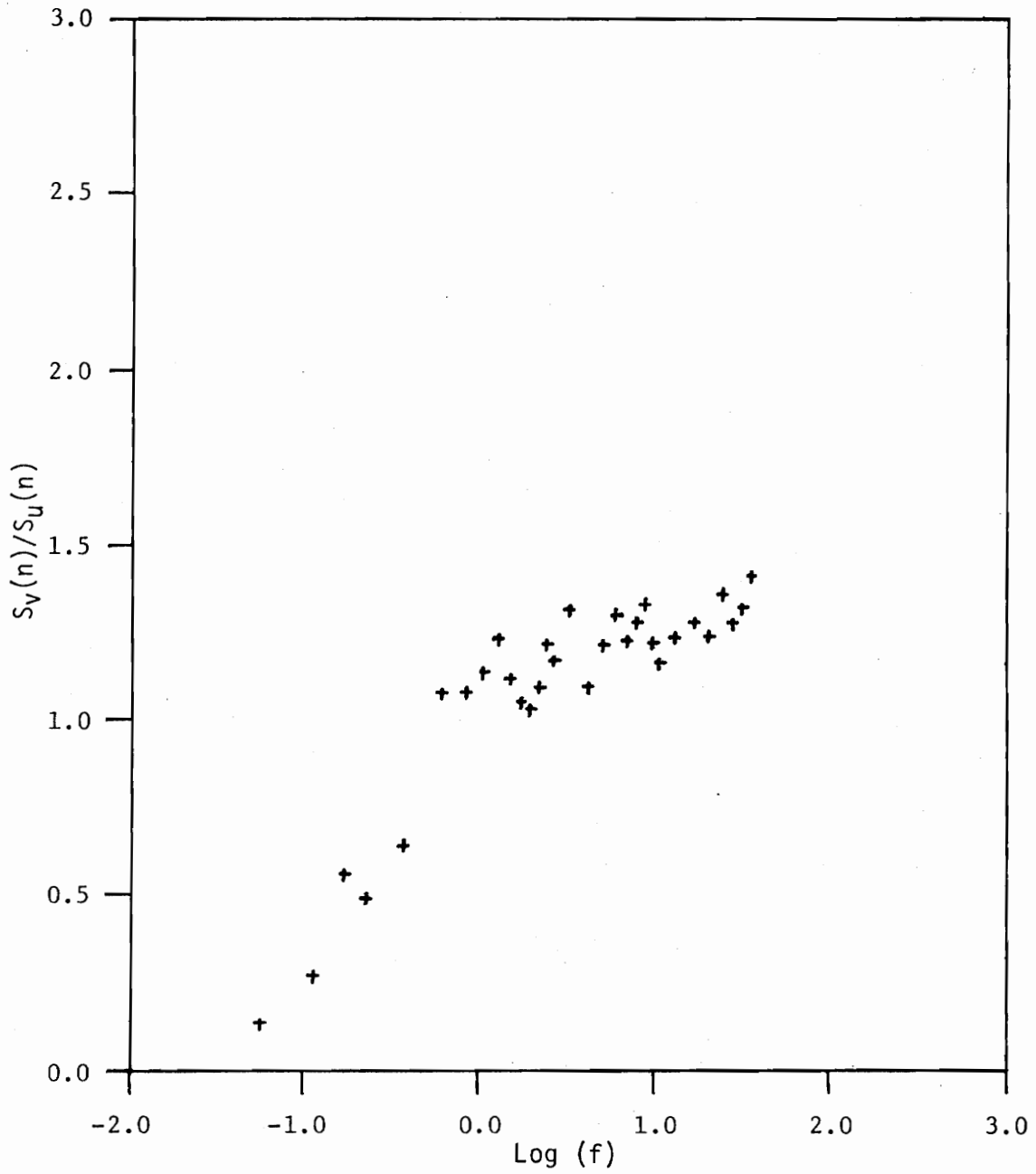


Figure 29. Ratio of lateral and longitudinal velocity spectra versus reduced frequency, Run 6, 50-foot level.

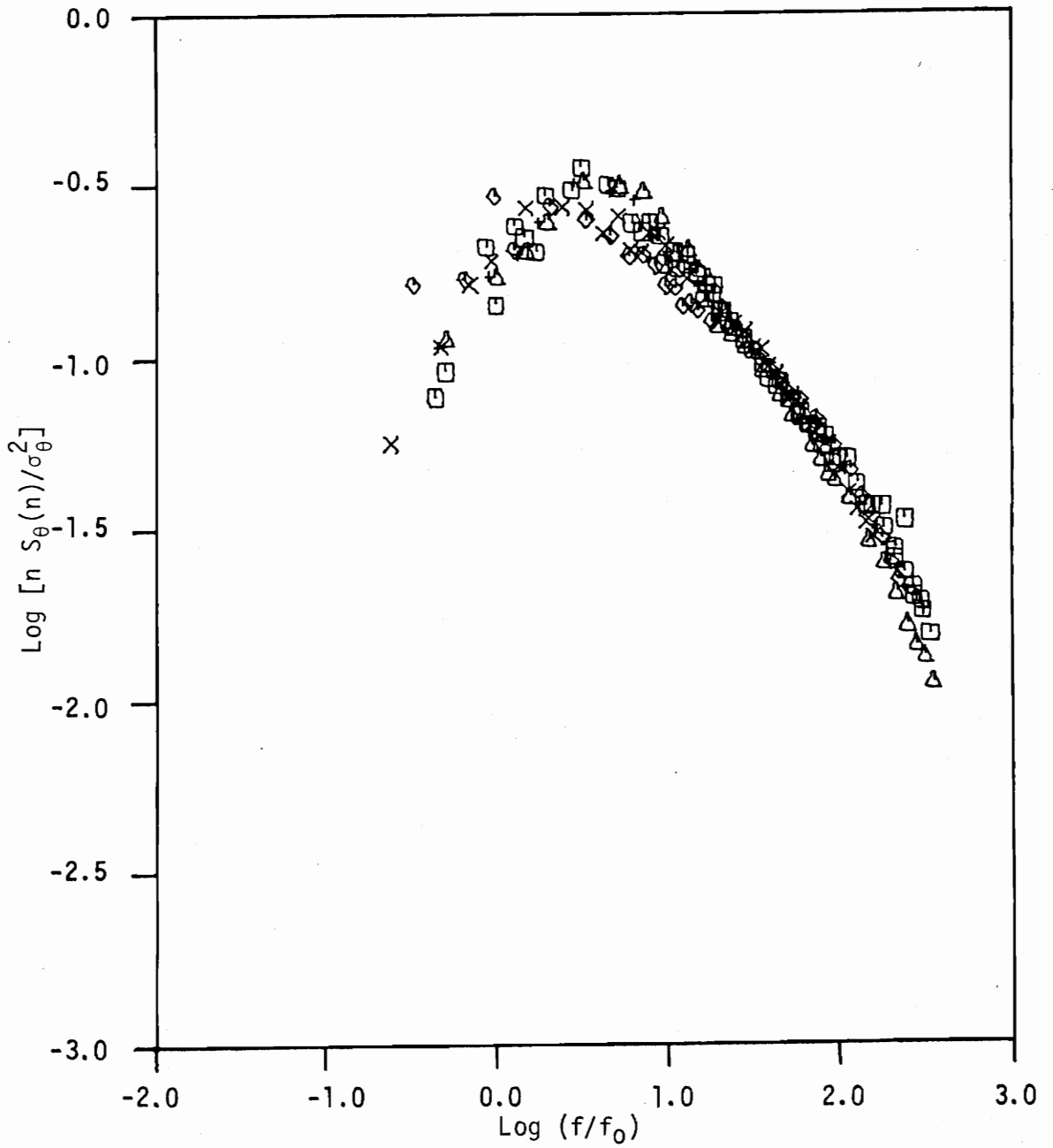


Figure 30a. Logarithmic spectra of the temperature fluctuations normalized by the variance versus  $f/f_0$ , moderately unstable,  $-1.0 < z/L < 0$ .

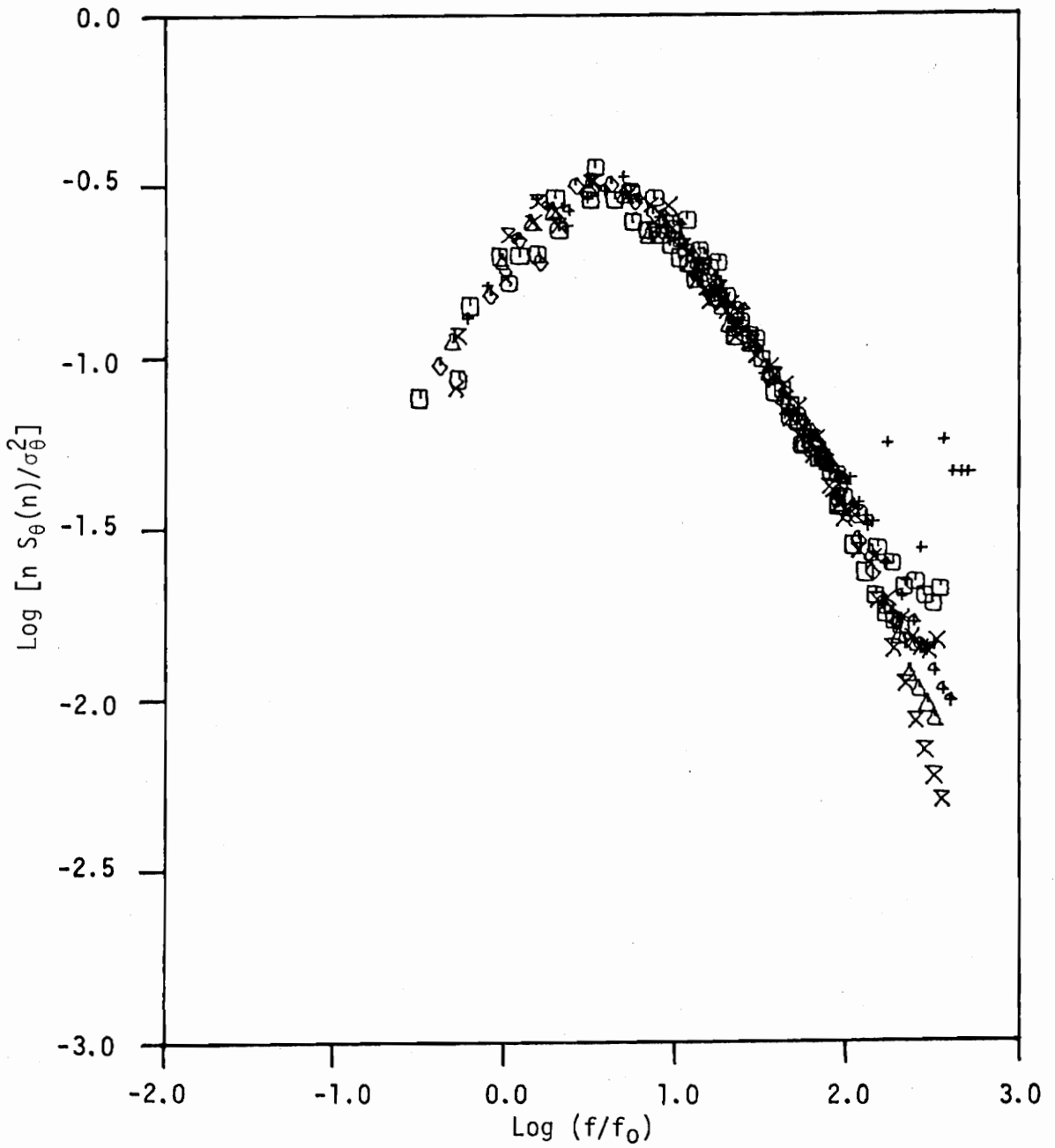


Figure 30b. Logarithmic spectra of the temperature fluctuations normalized by the variance versus  $f/f_0$ , moderately stable,  $0 < z/L < +1.0$ .

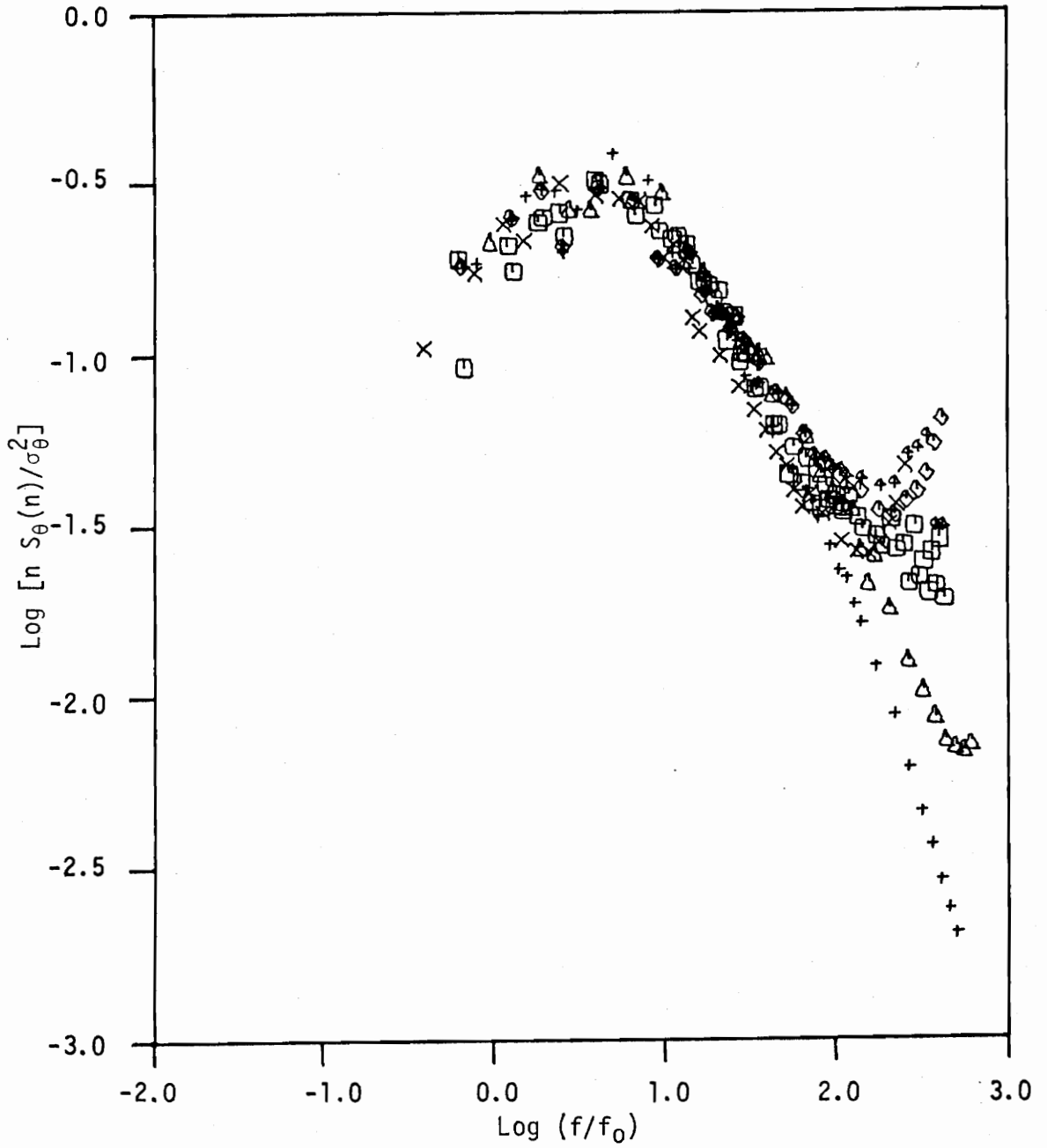


Figure 30c. Logarithmic spectra of the temperature fluctuations normalized by the variance versus  $f/f_0$ , very stable,  $z/L > +1.0$ .

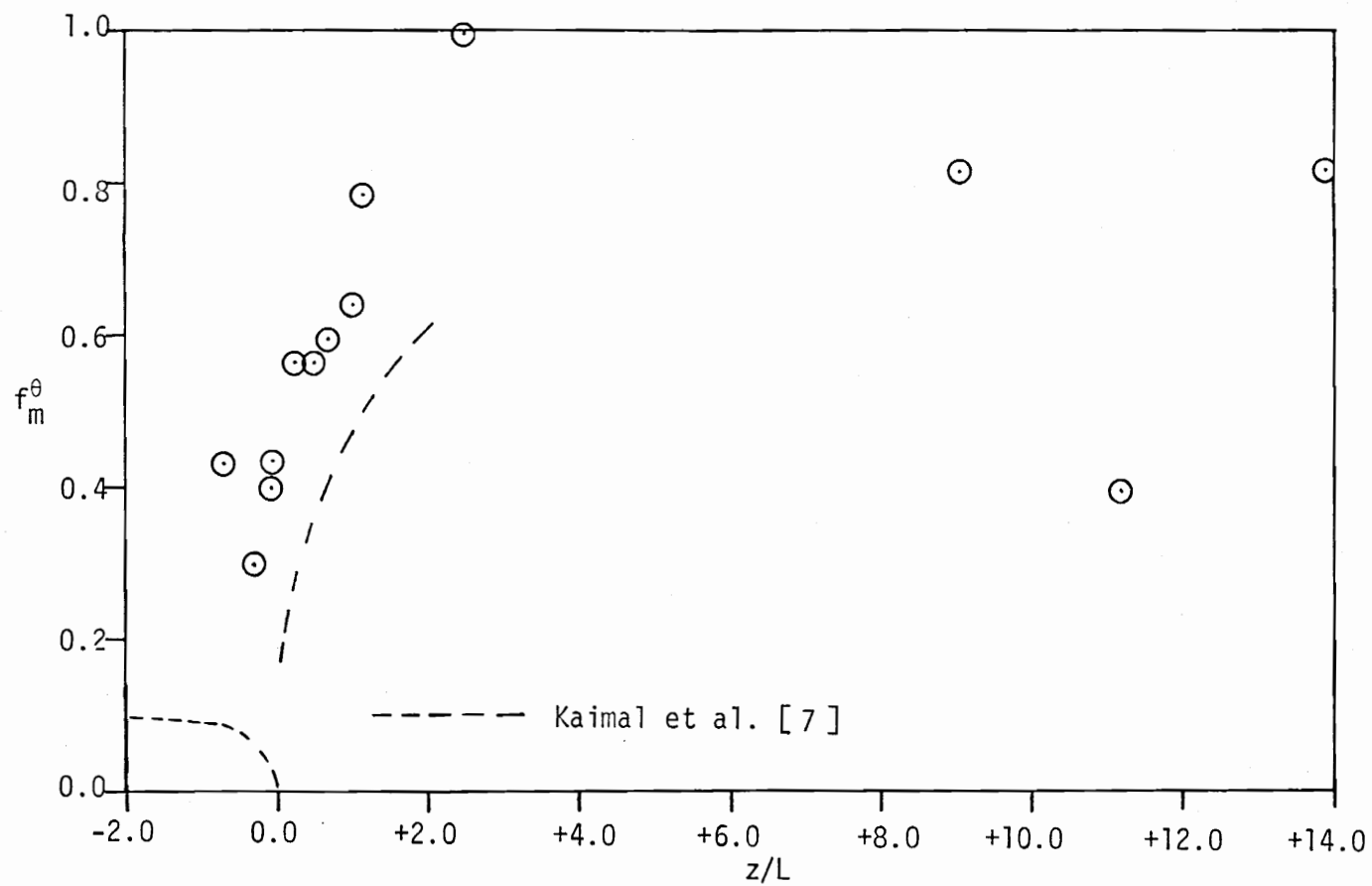


Figure 31. Variation of reduced peak-frequencies  $f_m^\theta$  for temperature spectra with  $z/L$ .

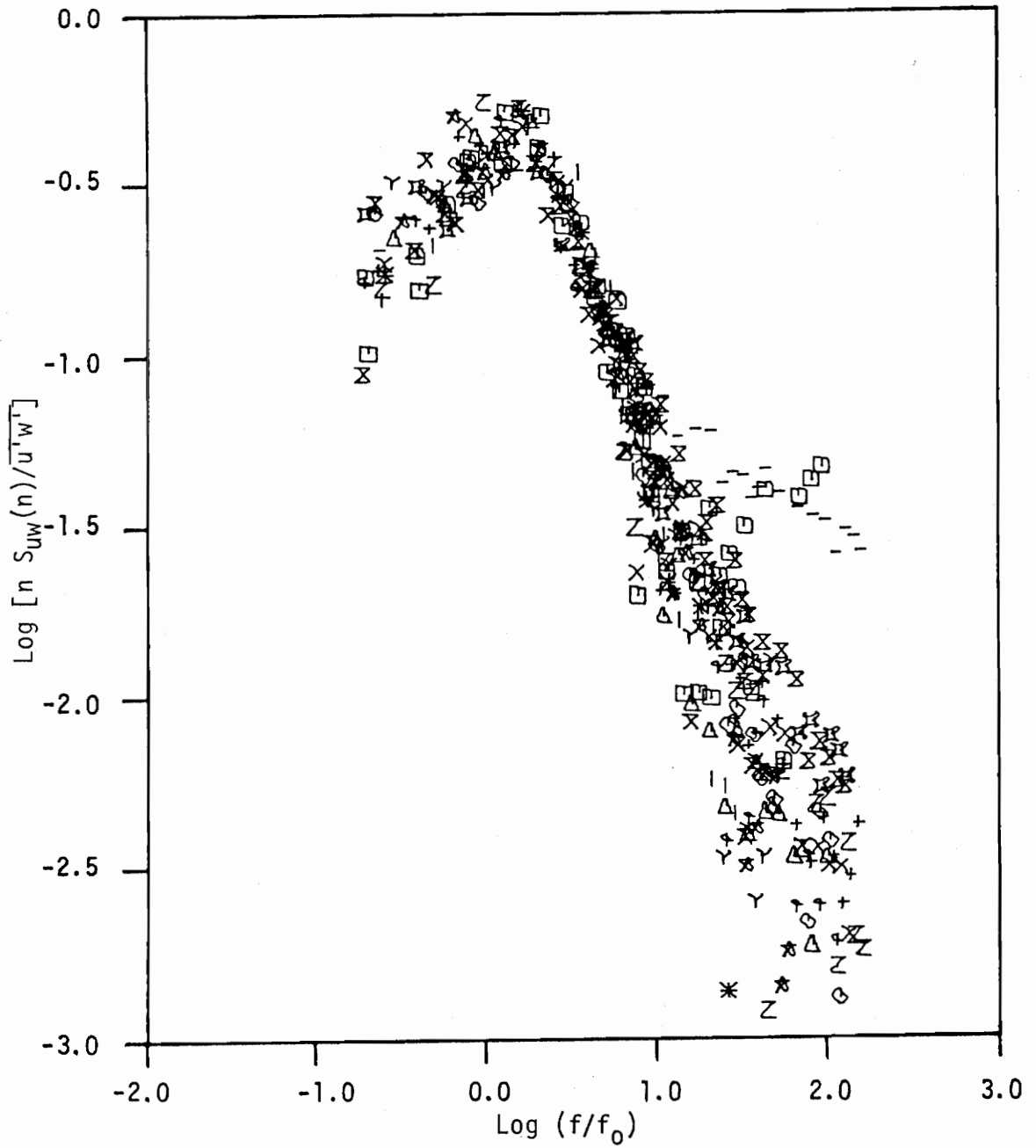


Figure 32a. Logarithmic uw cospectra normalized by the covariance  $f/f_0$ , moderately unstable,  $-1.0 < z/L < 0$ .

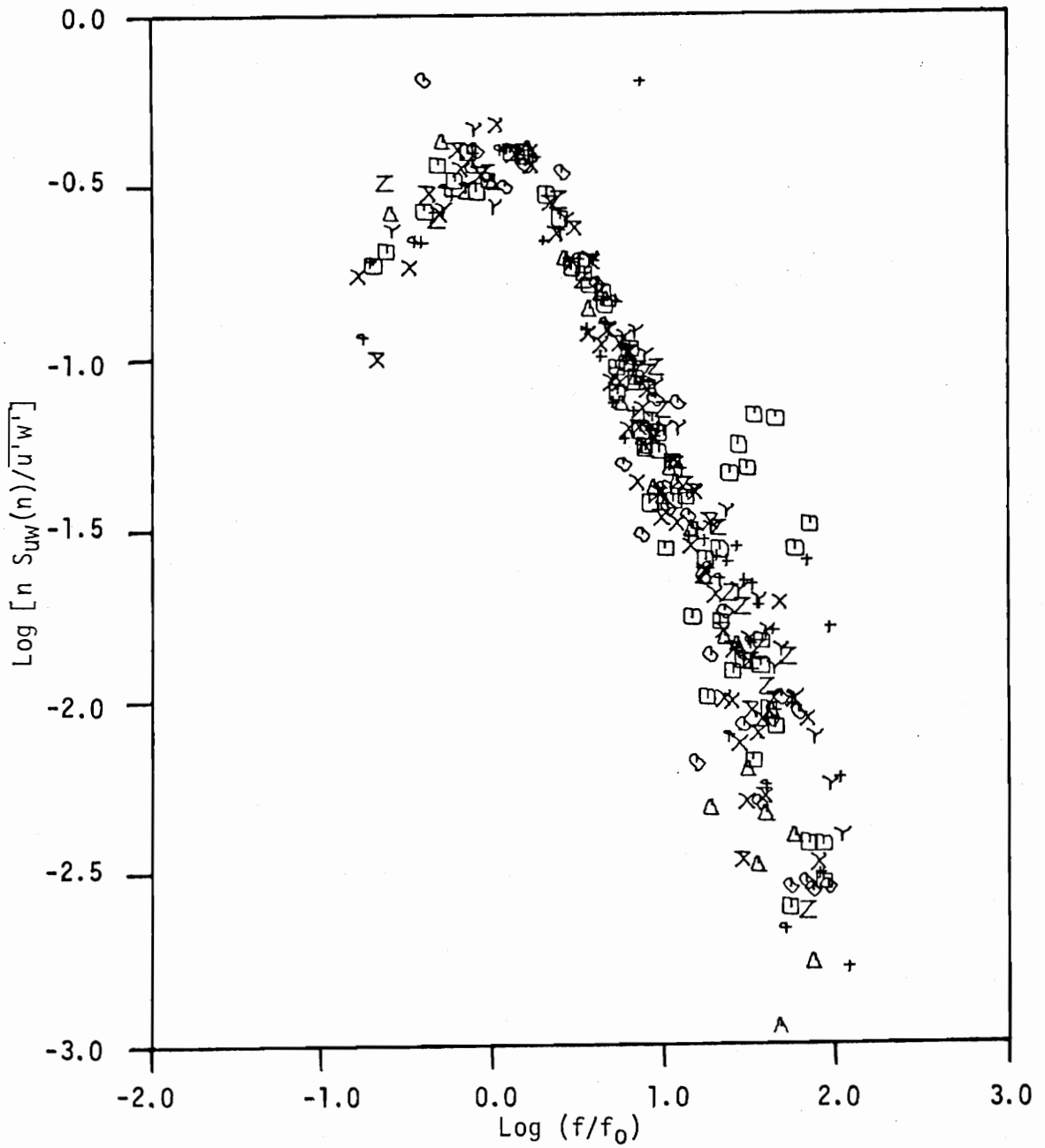


Figure 32b. Logarithmic  $uw$  cospectra normalized by the covariance  $f/f_0$ , moderately stable,  $0 < z/L < +1.0$ .

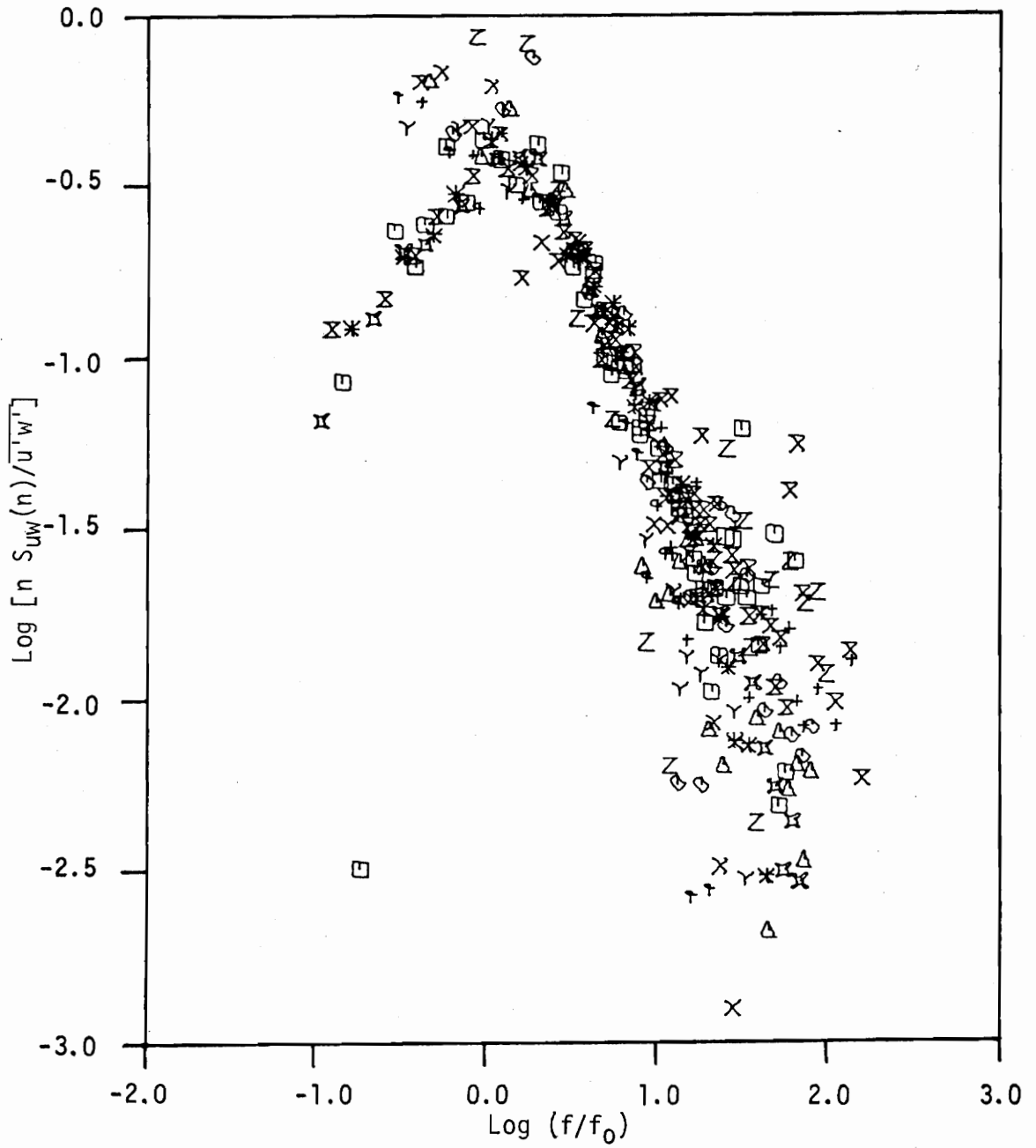


Figure 32c. Logarithmic uw cospectra normalized by the covariance  $f/f_0$ , very stable,  $z/L > +1.0$ .



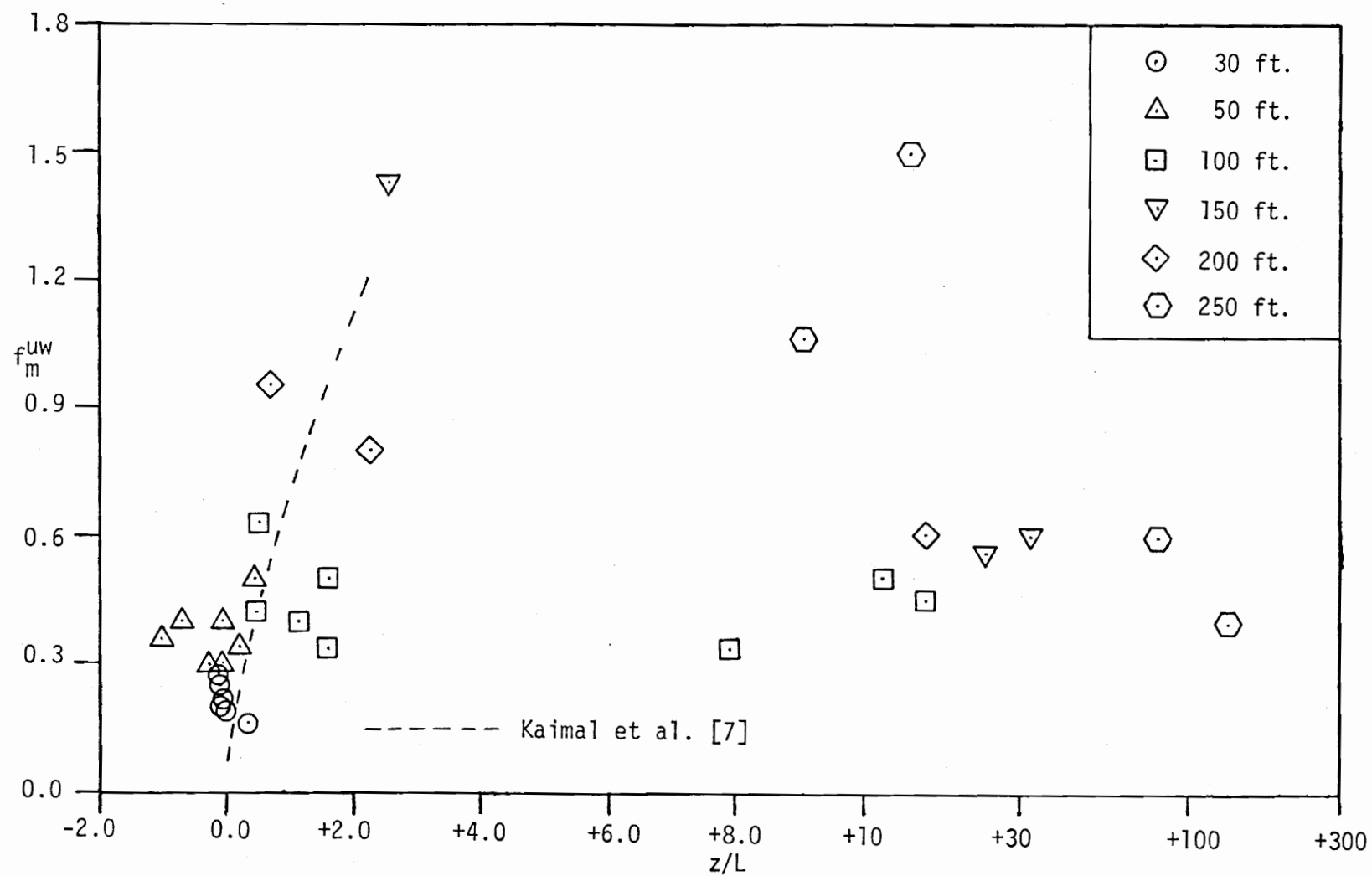


Figure 33. Variation of reduced peak-frequencies  $f_m^{uw}$  for the uw cospectra with  $z/L$ .

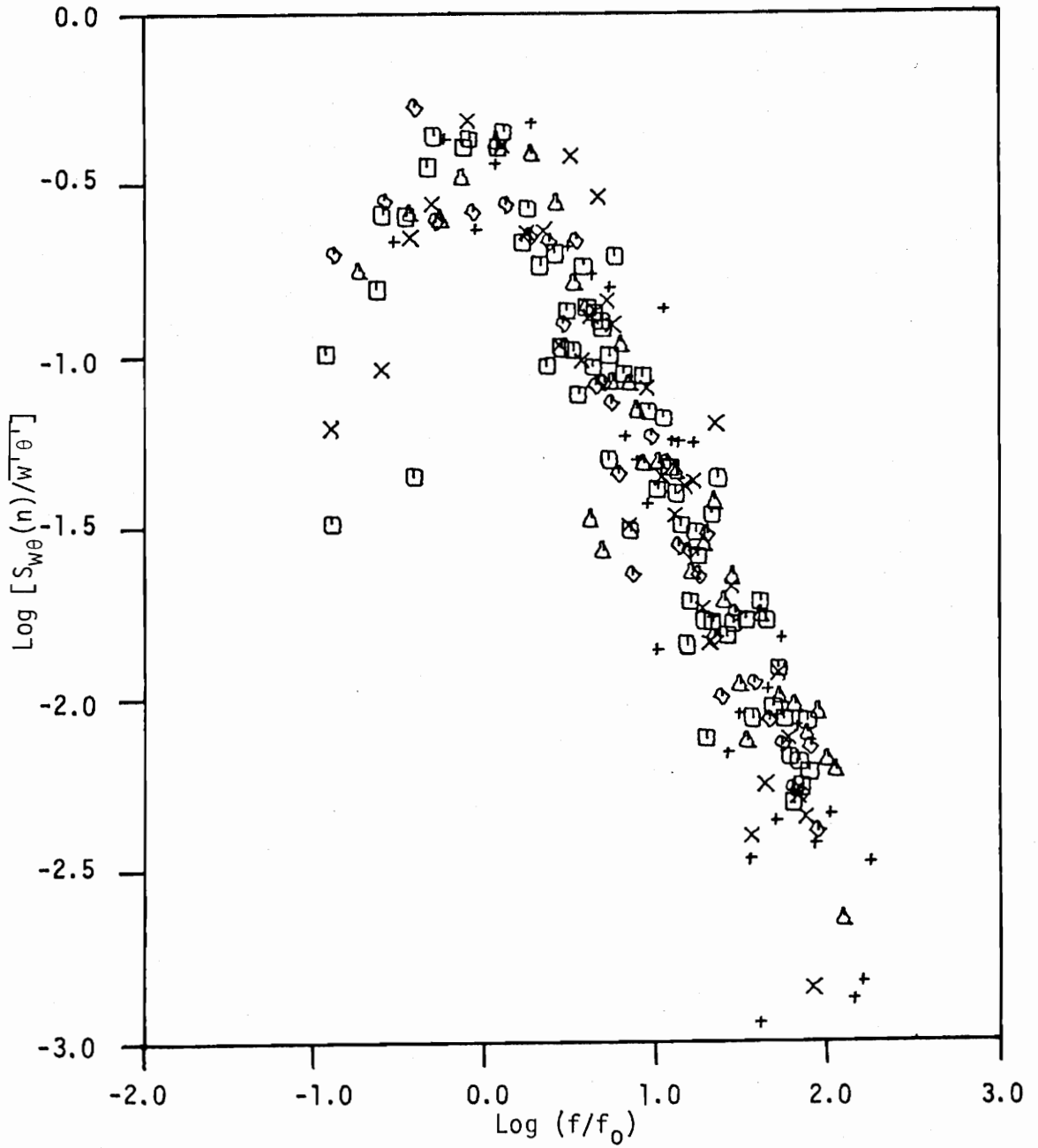


Figure 34a. Logarithmic  $w\theta$  cospectra normalized by the covariance versus  $f/f_0$ , moderately unstable,  $-1.0 < z/L < 0$ .

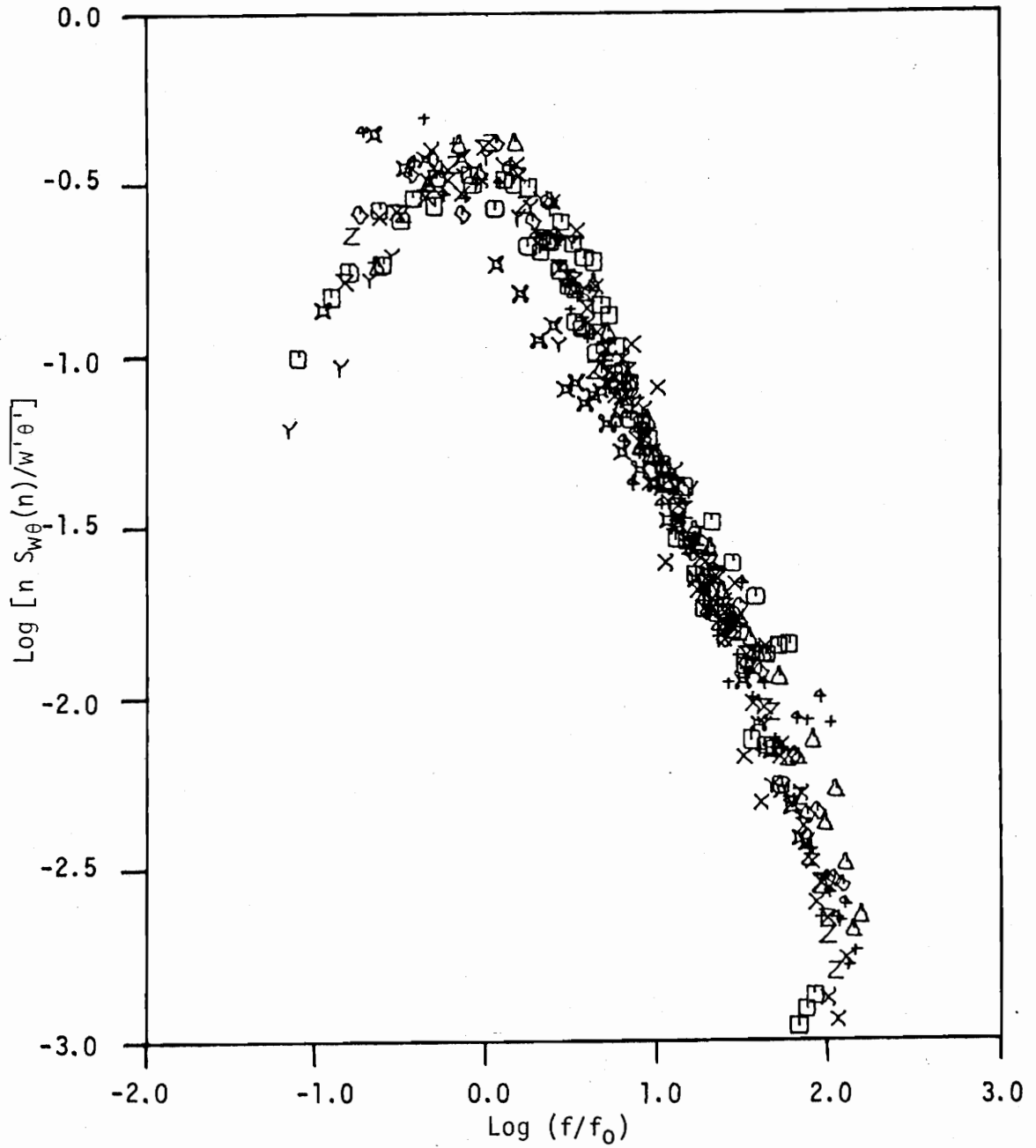


Figure 34b. Logarithmic  $w\theta$  cospectra normalized by the covariance versus  $f/f_0$ , moderately stable,  $0 < z/L < +1.0$ .

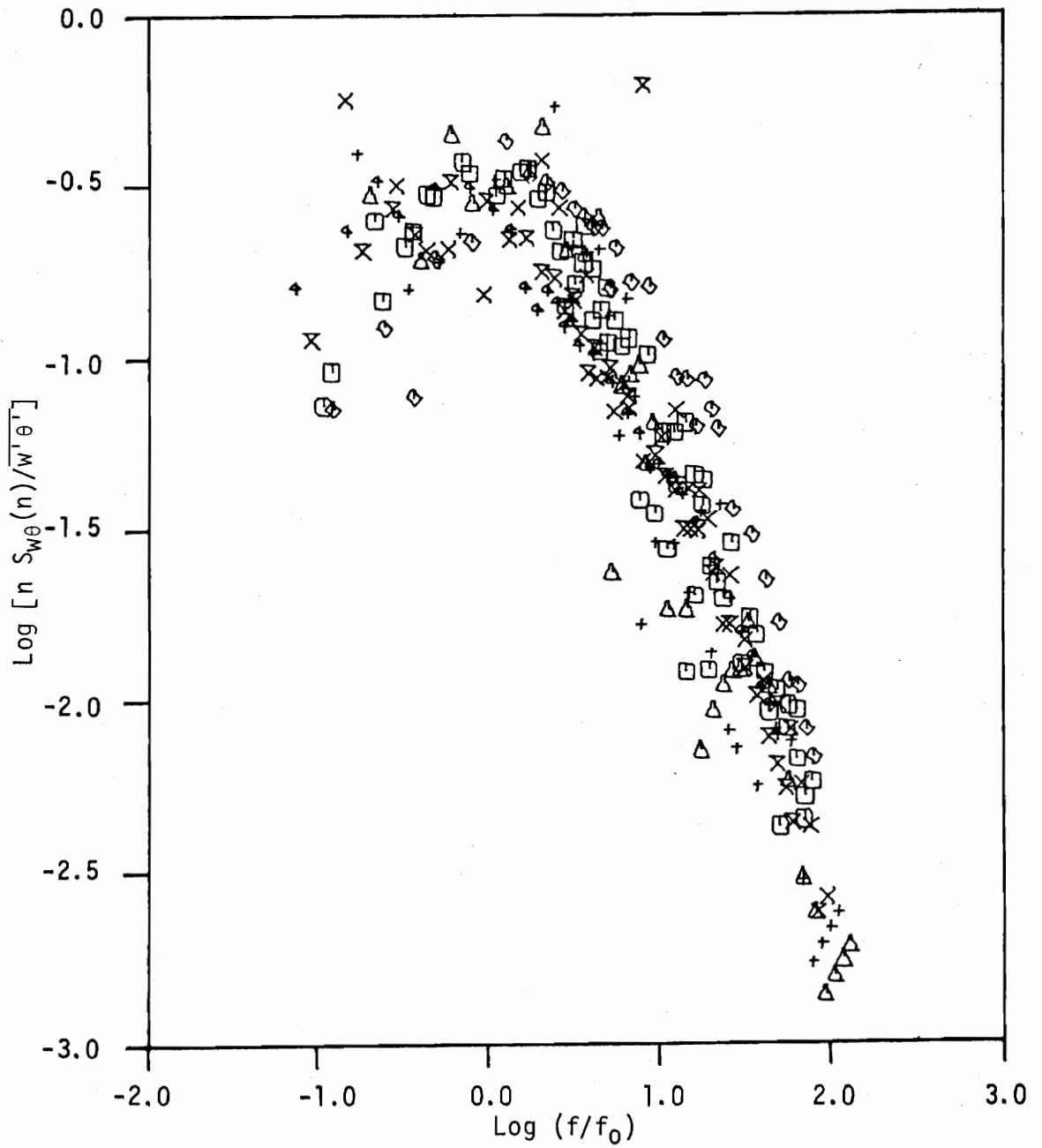


Figure 34c. Logarithmic  $w\theta$  cospectra normalized by the covariance versus  $f/f_0$ , very stable,  $z/L > +1.0$ .

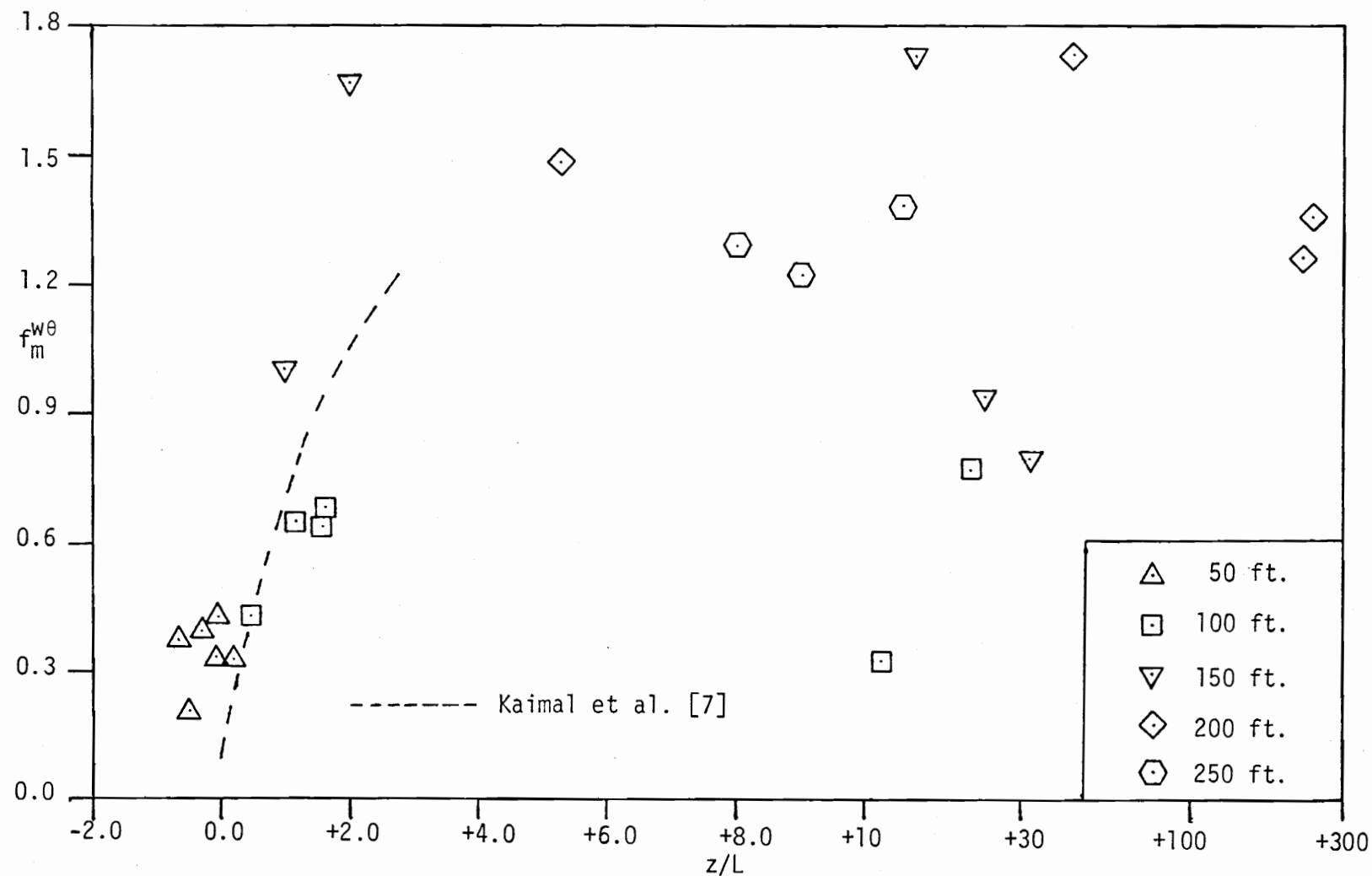


Figure 35. Variation of reduced peak-frequencies,  $f_m^{w\theta}$  for the  $w\theta$  cospectra with  $z/L$ .

## TABLES

TABLE 1. Summary of Mean Data and Integral Statistics for All Runs

Run	Date and Starting Time	z (ft)	U (fps)	z/L	R <sub>f</sub>	U <sub>o</sub> (fps)	T <sub>o</sub> (°F)	σ <sub>u</sub> (fps)	σ <sub>v</sub> (fps)	σ <sub>w</sub> (fps)	σ <sub>θ</sub> (°F)	-u'w' (fps) <sup>2</sup>	w'θ' (fps°F)	θ̄ (°R)	θ̄ (degrees)	L <sub>x</sub> (ft)	L <sub>y</sub> (ft)
I	7/27/76 12:52:00	1.5	-	-	-	-	-	-	-	-	-	-	-	533.74	-	-	-
		30.0	24.61	- 0.09	-	1.65	-	3.66	3.12	2.75	-	2.73	-	531.7	-	-	231
		50.0	28.2	- 0.281	- 0.146	1.34	-1.04	2.74	2.10	1.88	1.26	1.714	0.557	531.35	8.3	166	294
		100.0	32.85	+ 1.14	+ 0.481	0.86	+0.87	1.66	1.37	1.02	1.11	0.559	-0.299	531.35	9.7	542	556
		150.0	35.39	+ 1.0	+ 0.491	0.75	+0.39	1.65	1.61	1.1	0.63	0.23	-0.116	531.35	10.6	605	395
		200.0	39.25	+ 2.27	+ 0.291	0.60	+0.42	1.37	1.12	0.8	0.55	0.353	-0.101	531.0	13.1	652	435
		250.0	40.84	+ 9.06	+ 1.108	0.44	+0.72	0.98	0.88	0.65	0.45	0.146	-0.127	530.75	14.2	580	338
II	7/27/76 15:30:00	1.5	-	-	-	-	-	-	-	-	-	-	-	533.94	-	-	-
		30.0	16.99	- 0.033	-	1.99	-	3.62	3.11	2.91	-	3.798	-	532.8	-	-	250
		50.0	24.05	- 0.066	- 0.029	1.87	-0.48	3.47	2.76	2.27	1.54	3.350	0.357	532.55	16.0	-	385
		100.0	28.92	+ 0.49	+ 0.112	0.76	+0.29	1.73	1.44	1.09	0.78	0.579	-0.089	532.35	14.8	-	476
		150.0	32.93	-	-	-	-	-	-	-	-	-	-	532.2	14.4	-	-
		200.0	34.48	+ 0.68	+ 0.141	0.63	+0.14	1.26	1.0	0.76	0.81	0.361	-0.035	531.75	15.5	-	435
		250.0	38.2	+ 13.9	+ 1.68	0.41	+0.94	1.07	0.87	0.66	0.58	0.167	-0.154	531.43	15.3	-	439
III	8/5/76 13:49:00	1.5	-	-	-	-	-	-	-	-	-	-	-	539.7	-	-	-
		30.0	15.8	- 0.091	-	1.43	-	2.46	2.10	2.16	-	2.001	-	538.66	-	-	250
		50.0	18.74	- 0.69	- 0.484	0.86	-1.08	1.75	1.28	1.39	1.31	0.741	+0.37	537.89	- 1.0	278	357
		100.0	21.17	+ 7.9	+ 3.95	0.34	+0.96	0.89	0.84	0.66	1.06	0.11	-0.13	535.68	0.4	317	476
		150.0	20.17	+ 32.6	+16.05	0.32	+2.3	0.69	0.80	0.48	1.43	0.092	-0.295	535.98	0.4	461	556
		200.0	20.98	+ 15.4	+ 7.11	0.32	+0.82	0.69	0.60	0.50	1.08	0.067	-0.105	535.53	0.8	507	606
		250.0	22.1	80.6	+15.58	0.24	+1.96	0.57	0.50	0.50	0.90	0.052	-0.188	535.18	0.2	509	641
IV	8/5/76 15:37:30	1.5	-	-	-	-	-	-	-	-	-	-	-	534.77	-	-	-
		30.0	18.37	- 0.11	-	1.34	-	2.42	2.04	2.08	-	1.701	-0.537	533.98	-	-	231
		50.0	21.26	- 1.01	- 0.529	0.76	-1.21	1.63	1.34	1.22	1.61	0.56	+0.149	533.78	0.3	603	313
		100.0	22.03	+ 11.2	+ 7.95	0.41	+1.96	0.95	0.90	0.69	1.54	0.143	+0.089	531.69	1.4	1069	476
		150.0	21.8	+ 23.48	+26.12	0.4	+2.64	0.72	0.96	0.51	1.62	0.086	-0.423	531.99	1.3	1158	550
		200.0	23.03	+ 14.5	+12.38	0.37	+1.03	0.71	0.72	0.57	1.51	0.087	-0.152	531.39	1.7	1130	588
		250.0	23.74	+131.6	+43.49	0.21	+2.45	0.65	0.65	0.57	0.91	0.042	-0.206	530.89	1.2	1143	694
V	8/12/76 14:01:00	1.5	-	-	-	-	-	-	-	-	-	-	-	535.24	-	-	-
		30.0	17.94	- 0.066	-	1.79	-	2.89	2.76	2.41	-	3.11	-	533.75	-	-	250
		50.0	19.44	+ 0.459	+ 0.541	1.11	1.17	1.83	1.37	1.39	1.48	0.95	-0.519	532.75	- 5.9	376	-
		100.0	21.96	+ 21.64	+16.26	0.44	4.32	1.95	0.82	0.68	2.16	0.13	-0.76	530.96	- 5.1	530	370
		150.0	-	-	-	-	-	-	-	-	-	-	-	531.16	- 5.4	576	-
		200.0	22.25	+246	+11.82	0.22	6.14	0.70	0.79	0.57	2.03	0.042	-0.54	530.47	- 4.2	651	351
		250.0	22.36	-	-	0.52	-	0.64	0.84	0.57	-	0.052	-	529.97	- 4.0	691	463

TABLE 1 (continued).

Run	Date and Starting Time	z (ft)	U (fps)	z/L	R <sub>F</sub>	U <sub>s</sub> (fps)	T <sub>s</sub> (°F)	σ <sub>u</sub> (fps)	σ <sub>v</sub> (fps)	σ <sub>w</sub> (fps)	σ <sub>θ</sub> (°F)	$\overline{u'w'}$ (fps) <sup>2</sup>	$\overline{w'\theta'}$ (fps°F)	$\overline{\theta'^2}$ (°R)	φ (degrees)	L <sub>z</sub> (ft)	u <sub>m</sub> (ft)
VI	8/12/76 15:42:46	1.5	-	-	-	-	-	-	-	-	-	-	-	534.12	-	-	-
		30.0	18.75	- 0.017	-	1.58	-	2.90	2.77	2.29	-	2.152	-	533.37	-	-	200
		50.0	21.19	- 0.052	- 0.057	1.30	-0.18	2.27	1.75	1.64	1.13	1.292	0.0943	532.83	1.4	384	385
		100.0	23.41	+ 1.57	+ 0.682	0.48	+0.37	1.11	0.98	0.81	0.81	0.213	-0.02	530.74	2.3	692	556
		150.0	-	-	-	-	-	-	-	-	-	-	-	530.94	1.9	696	-
		200.0	23.98	+ 5.3	+ 3.244	0.39	+0.42	0.85	0.83	0.67	0.99	0.117	+0.002	530.24	2.5	859	465
		250.0	-	-	-	-	-	-	-	-	-	-	-	529.75	2.2	827	-
VII	8/13/76 14:12:00	1.5	-	-	-	-	-	-	-	-	-	-	-	538.52	-	-	-
		30.0	17.32	- 0.02	-	1.94	-	3.27	3.34	2.79	-	3.554	-	536.33	-	-	176
		50.0	22.07	- 0.08	- 0.04	1.55	-0.38	2.66	2.13	1.99	0.89	1.895	0.238	534.74	12.7	54	263
		100.0	28.48	+ 0.25	+ 0.0433	0.56	+0.08	1.17	0.95	0.71	0.54	0.265	-0.018	533.34	13.5	257	303
		150.0	32.12	+ 2.52	+ 0.523	0.51	+0.45	0.92	0.89	0.57	0.57	0.17	-0.092	533.94	14.9	491	217
		200.0	35.19	+224	+25.53	0.19	+4.21	0.40	0.41	0.28	1.51	0.016	-0.320	535.53	20.2	562	230
		250.0	35.79	-	-	0.11	-	0.34	0.26	0.18	-	0.013	-	536.83	22.4	1331	-
VIII	8/13/76 15:37:00	1.5	-	-	-	-	-	-	-	-	-	-	-	537.33	-	-	-
		30.0	20.46	- 0.033	-	1.9	-	3.57	3.43	2.89	-	3.614	-	535.73	-	-	203
		50.0	24.1	- 0.016	- 0.013	2.87	-0.27	3.61	2.14	3.76	0.76	8.246	+0.315	534.54	10.9	61	168
		100.0	30.24	+ 1.61	+ 0.074	0.61	+0.62	1.35	1.13	0.84	1.0	0.373	-0.152	533.14	11.6	140	360
		150.0	38.75	-	-	-	-	1.09	1.25	0.69	0.45	-0.121	-0.041	533.34	11.9	172	290
		200.0	36.01	-	-	-	-	1.04	0.87	0.61	0.57	0.209	+0.0025	533.44	13.9	155	311
		250.0	41.65	-	-	-	-	1.0	0.98	0.63	-	0.262	-	533.54	15.0	530	302
IX	8/13/76 17:04:50	1.5	-	-	-	-	-	-	-	-	-	-	-	534.42	-	-	-
		30.0	19.16	+ 0.34	-	1.44	-	2.90	2.51	2.35	-	2.071	-	534.47	-	-	-
		50.0	20.82	+ 0.20	+ 0.135	2.04	+1.72	3.0	3.06	3.10	1.78	4.188	-1.403	534.52	25.2	94	232
		100.0	25.33	+ 0.83	+ 0.24	0.87	+0.65	2.34	2.28	1.57	2.45	0.758	-0.227	533.12	25.2	85	-
		150.0	29.82	+ 14.6	+ 3.434	0.71	+5.0	1.64	1.81	0.97	2.52	0.499	-1.419	533.22	23.8	135	389
		200.0	32.26	+ 44.0	+ 9.076	0.62	+8.7	1.20	1.10	0.82	3.23	0.383	-2.158	533.07	23.7	167	424
		250.0	36.76	-	-	-	-	-	-	-	-	-	-	532.92	22.6	183	-



TABLE 2. Summary of the spectral characteristics for the variance normalized logarithmic spectra versus the modified frequency  $f/f_m$ .

	Category I Moderately Unstable	Category II Moderately Stable	Category III Very Stable
$[n S_W(n)/\sigma_W^2]_{f=f_m}$	0.32	0.27	0.27
$f_m$ (average)	0.52	0.92	1.15
Intercept of high frequency range $(f/f_m)^{2/3}$ with $n S_W(n)/\sigma_W^2 = 1$	0.29	0.35	0.34
Intercept of low frequency range $(f/f_m)^{+1}$ with $n S_W(n)/\sigma_W^2 = 1$	2.19	1.58	1.58

TABLE 3. Summary of the spectral characteristics for the variance normalized logarithmic spectra versus the modified frequency  $f/f_0$ .

		Category I Moderately Unstable	Category II Moderately Stable	Category III Very Stable
$[n S_\alpha(n)/\sigma_\alpha^2]_{f=f_m}$	u	-	-	-
	v	0.32	0.29	0.28
	w	0.30	0.27	0.27
$f_m/f_0$	u	-	-	-
	v	3.39	3.09	3.50
	w	3.36	3.02	3.35
Intercept of low frequency range $(f/f_0)^{+1}$ with $n S_\alpha(n)/\sigma_\alpha^2 = 1$	u	-	-	-
	v	6.84	5.37	5.31
	w	6.17	4.90	4.95

## VITA

Darrell B. Derrington, Jr., was born on the 29th of August in the year of our Lord nineteen hundred and fifty-three in Dayton, Texas. He attended pre-college school in various states including Texas, Mississippi, Louisiana, New Mexico and Washington state. After moving to Virginia he pursued and acquired an Associate degree in Pre-Engineering at Lord Fairfax Community College in 1973. His education continued at Virginia Polytechnic Institute and State University where he acquired a Bachelor of Science degree in Engineering Science and Mechanics in 1976. He is currently pursuing a Master of Science degree in Engineering Science and Mechanics at Virginia Polytechnic Institute and State University and hopes to find employment immediately thereafter.

A handwritten signature in black ink that reads "Darrell B. Derrington Jr." The signature is written in a cursive style with a large, stylized 'D' at the beginning and a long, sweeping flourish at the end.

AN EXPERIMENTAL STUDY OF THE ATMOSPHERIC BOUNDARY LAYER  
MODIFIED BY A CHANGE IN SURFACE ROUGHNESS  
AND SURFACE TEMPERATURE

by

Darrell B. Derrington, Jr.

(ABSTRACT)

Three-dimensional wind measurements and temperature measurements were obtained on a 250-foot meteorological tower located near the Atlantic Ocean at Wallops Island, Virginia. The type of flow measured approached the tower from the ocean resulting in a complex three-dimensional type of flow as it sees a change in roughness and a possible change in surface temperature when passing the shore line. During warm summer afternoons the stable air is heated from below, and an internal boundary layer (IBL) with an unstable stratification develops within the stable layer which originated over the ocean. As this flow moves inland the IBL grows vertically depending on changes in surface roughness and surface temperature. Eventually, far enough inland, the IBL replaces the original stable layer. The vertical heat flux is positive in the IBL and negative in the overlying inversion. The point where the heat flux changes sign corresponds to the height of the IBL.

Measurements of the mean and turbulent flow quantities were made with a special computer-controlled data-acquisition system for

the aforementioned type of flow. Data analysis includes the following statistical parameters: mean values, variances, covariances (heat flux and Reynold's stresses), spectra and cospectra. Nine, one-hour runs were analyzed and the results agreed closely with the suggested model.

In addition, the spectra and cospectra measured in the IBL as well as those from the overlying inversion layer reduce to a family of curves when expressed in appropriate similarity coordinates. These results for moderately, thermally stratified flows compare quite well with the Kansas data which were obtained in the surface layer. The results for very stable flow ( $z/L > 2.0$ ) do not follow the same trend as was established in the moderately stable range.